

---

# Investigation and Electrical Manipulation of Adsorbed Polymers measured by Atomic Force Microscopy

Matthias Erdmann

---



München 2009

---

# **Investigation and Electrical Manipulation of Adsorbed Polymers measured by Atomic Force Microscopy**

**Matthias Erdmann**

---

Dissertation  
an der Fakultät für Physik  
der Ludwig-Maximilians-Universität  
München

vorgelegt von  
Matthias Erdmann  
aus Coburg

München, den 15.09.2009

Erstgutachter: Prof. Dr. Hermann E. Gaub

Zweitgutachter: Prof. Dr. Erwin Frey

Tag der mündlichen Prüfung: 20.10.2009

# Abstract

Polymers, which are adsorbed on surfaces, offer a broad range of technological applications such as adhesives, lubricants and composite materials or nanodevices and sensors. Thereby, their functionality is mainly governed by their static and dynamic properties and in particular, by their adhesion strength or bonding mechanisms to the substrate. These characteristics are determined by local interactions between the polymer and the surface on the molecular scale. Therefore, AFM based single molecule force spectroscopy was used to determine the conformation and the friction of single adsorbed polymers. Moreover, the adhesion strength and alternatively the bonding of single polymers to surfaces were externally controlled and manipulated by electrochemical techniques and measured by AFM.

- The end-to-end distance of a polymer characterizes its spatial structure and depends on the Kuhn length, the contour length and an exponential scaling factor. With a new mechanical approach, the end-to-end distance of carboxymethylamylose (CMA) being adsorbed on an amino surface was determined. CMA exhibits a high in-plane mobility on this surface and eludes conventional imaging techniques. Thus, single CMA polymer chains were covalently pinned with one segment to the amino surface and then picked up randomly with the AFM tip. Upon retracting the AFM tip, the polymer section between pinpoint and pickup point was stretched. The distance between these two points was derived by laterally scanning the area above the surface at a constant height and measuring the normal force. This distance corresponds to the end-to-end distance of this polymer section. Due to its self-similarity, the entire polymer and the polymer section are characterized by the same scaling factor. Then, the contour length of the CMA-section was measured by vertical force extension curves. A Kuhn-length of 0.44 nm and a scaling exponent of 0.74 were found indicating an almost plain adsorption with conformational rearrangement on the surface. Moreover, the contributions of tangential force components to the normal force in AFM experiments were determined.
- Despite their quasi-irreversible adsorption to a substrate, polymers may exhibit a high in-plane mobility and rearrange their conformation as seen above. To study the mobility of adsorbed polymers, ssDNA or polyallylamine were covalently bound to the AFM tip and were allowed to adsorb on different substrates. The AFM tip was then retracted not only vertically, but also horizontally to the surface, which resulted in a tangential force component acting on the adsorbed polymer. Depending on the friction coefficient between polymer and surface, this new measurement protocol caused either a desorption of the polymer, a sliding

---

across the surface or a combination of both cases. It could be shown that ssDNA is highly mobile on a mica substrate, but is immobile on a gold surface due to high friction forces. For polyallylamine, a friction coefficient of  $1.4 \times 10^{-5}$  Ns/m was determined on a mica surface. This value shows that the AFM allows to measure friction coefficients of single adsorbed polymers, which cannot be resolved in conventional experiments driven by thermal diffusion.

- Coulombic interactions may contribute to the adhesion strength of polymers on surfaces. In order to control and to measure the electrostatic adhesion, AFM based desorption experiments with dsDNA were conducted on gold electrodes covered by a self-assembled monolayer (SAM). Therefore, dsDNA was covalently attached to the AFM tip. The coulomb interaction was biased with the composition of the monolayer and the desorption force was then adjusted externally by the applied potential. Positive electrode potentials induced the adsorption of the negatively charged dsDNA onto an OH-terminated SAM electrode resulting in adhesion forces for an individual dsDNA molecule of up to 25 pN (at +0.5 V vs. Ag/AgCl). Applying negative potentials completely suppressed dsDNA adsorption onto the OH-SAM. Furthermore, the coulombic contributions of the backbone phosphate charges and the double charged terminal phosphate group were measured and confirmed by a model based on Gouy-Chapman-Theory. The desorption force for dsDNA on an NH<sub>2</sub>-SAM electrode could also be modulated in the range of 20 pN by the applied potential.
- Not only the coulombic adhesion control of charged polymers is of great interest in numerous technological devices, also an electrically controlled chemisorption would provide a richness of novel applications. Thus, the interaction of dsDNA with a gold electrode was characterized for different applied potentials, whereby the dsDNA was again functionalized to the AFM tip. Thereby, dsDNA chemisorbed exclusively at the ends via coordinate nitrogen-gold bonds to the electrode. Moreover, the complex electrochemical conditions were identified, which are required for this controlled "electrosorption" of dsDNA to gold. The formation of N-Au bonds between primary amines of the bases and the gold electrode was proven by systematically varying the sequence of the nucleotides at the free end of the dsDNA. Force spectroscopy experiments with a single adenosine nucleotide on a PEG spacer revealed an N-Au binding force of 170 pN, which is in perfect agreement with model calculations. For the latter two studies, AFM based single molecule force spectroscopy was combined with electrochemical techniques for the first time.

The new three dimensional measurement protocols to determine the conformation and friction of adsorbed polymers and the combination of AFM and electrochemistry to control the adhesion or bonding of polymers promise to be the basis for further experimental or theoretical studies and technological applications.

# Zusammenfassung

Auf Oberflächen adsorbierte Polymere bieten eine Vielzahl von technologischen Anwendungsmöglichkeiten, wie zum Beispiel Kleber, Schmiermittel und Verbundmaterialien. Aber auch im Bereich der Nanotechnologie kommen sie als funktionelle Bauteile oder Sensoren zum Einsatz. Ihre Funktionalität wird dabei hauptsächlich durch ihre statischen und dynamischen Eigenschaften und besonders durch ihre Adhäsionsstärke oder Bindungsmechanismen an Substrate bestimmt. Diese Eigenschaften werden durch lokale Wechselwirkungen zwischen Polymer und Oberfläche auf der molekularen Ebene festgelegt. Deshalb wurde die AFM-basierte Kraftspektroskopie angewandt, um die Konformation und die Reibung von einzelnen, adsorbierten Polymeren zu bestimmen. Darüber hinaus wurden die Adhäsionsstärke und alternativ dazu die Bindung von einzelnen Polymeren auf Oberflächen extern durch elektrochemische Techniken kontrolliert und manipuliert und mit dem AFM gemessen.

- Der End-zu-End-Abstand eines Polymers kennzeichnet seine räumliche Struktur und hängt von der Kuhnlänge, der Konturlänge und einem exponentiellen Skalierungsfaktor ab. Mit einem neuen mechanischen Ansatz wurde der End-zu-End-Abstand von Carboxymethylamylose (CMA) bestimmt, die auf einer Aminooberfläche adsorbiert wurde. CMA weist eine hohe Mobilität auf dieser Oberfläche auf und entzieht sich konventionellen Abbildungstechniken. Deshalb wurden einzelne CMA-Polymerketten mit einem ihrer Segmente auf die Aminooberfläche kovalent verankert und dann mit der AFM-Spitze an einer beliebigen Stelle aufgegriffen. Der Polymerabschnitt zwischen Ankerpunkt und Aufnahmepunkt wurde durch das Zurückziehen der AFM-Spitze gedehnt. Die Distanz zwischen diesen beiden Punkten wurde dadurch bestimmt, indem die AFM-Spitze lateral über der Oberfläche bewegt wurde und die Normalkraft detektiert wurde. Diese Distanz entspricht dem End-zu-Endabstand des Polymerabschnitts. Aufgrund seiner Selbstähnlichkeit werden das gesamte Polymer und dieser Abschnitt durch den selben Skalierungsfaktor beschrieben. Als nächstes wurde die Konturlänge des CMA-Abschnitts durch vertikale Kraft-Abstands-Kurven gemessen. Diese zwei Messungen ergaben eine Kuhnlänge von 0.44 nm und einen Skalierungsexponenten von 0.74, der auf eine nahezu vollständige Adsorption mit einer Konformationsänderung auf der Oberfläche schließen läßt. Darüber hinaus wurde der Beitrag von tangentialen Kraftkomponenten zu der Normalkraft in AFM-Experimenten bestimmt.
- Trotz ihrer quasi irreversiblen Adsorption auf ein Substrat können Polymere wie oben beschrieben eine hohe Oberflächenmobilität aufweisen und ihre Konformation ändern. Um die Mobilität von adsorbierten Polymeren zu untersuchen, wurde

---

ssDNA und Polyallylamin kovalent an die AFM-Spitze gebunden und konnten dann auf verschiedene Substrate adsorbieren. Die AFM-Spitze wurde dann nicht nur vertikal, sondern auch horizontal zur Oberfläche von dieser zurückgezogen, was eine auf das adsorbierte Polymer wirkende tangentielle Kraftkomponente verursachte. Abhängig vom Reibungskoeffizienten zwischen Polymer und Oberfläche kam es entweder zu einer Desorption des Polymers, einem Gleiten über die Oberfläche oder einer Kombination von beiden Fällen. Bei ssDNA konnte gezeigt werden, dass sie auf Glimmer hochmobil ist, auf Gold aber sehr hohe Reibungskräfte auftreten. Für Polyallylamin wurde ein Reibungskoeffizient von  $1.4 \times 10^{-5}$  Ns/m auf einer Glimmeroberfläche ermittelt. Dieser Wert zeigt, dass man mit dem AFM Reibungskoeffizienten von einzelnen, adsorbierten Polymeren messen kann, die messtechnisch durch Experimente basierend auf thermischer Diffusion nicht bestimmt werden können.

- Coulombwechselwirkungen können zu der Adhäsionsstärke von Polymeren auf Oberflächen mit beitragen. Um die elektrostatische Adhäsion zu kontrollieren und zu messen, wurden AFM-basierte Desorptionsexperimente mit dsDNA auf Goldelektroden durchgeführt, welche mit einer Monoschicht von selbstanordnenden Molekülen bedeckt war (SAM). Zuvor wurde dsDNA kovalent an die AFM-Spitze angebunden. Ein Desorptionskraft-Offset wurde durch die Zusammensetzung des SAMs festgelegt und der Coulombanteil der Desorptionskraft wurde dann extern durch das angelegte Potential eingestellt. Positive Elektrodenpotentiale führten zur Adsorption der negativ geladenen dsDNA auf eine OH-terminierte SAM-Elektrode, wobei Desorptionskräfte für ein einzelnes dsDNA-Molekül von bis zu 25 pN erreicht wurden (bei +0.5 V vs. Ag/AgCl). Durch das Anlegen von negativen Spannungen wurde die Adsorption von dsDNA vollständig verhindert. Darüber hinaus wurden die unterschiedlichen Coulombwechselwirkungen der Phosphatgruppen des Rückgrats und der doppelt geladenen terminalen Phosphatgruppe der dsDNA gemessen und durch ein auf der Gouy-Chapman-Theorie bestehendes Modell bestätigt. Die Desorptionskraft für dsDNA von einer NH<sub>2</sub>-SAM-Elektrode konnte ebenso im Bereich von 20 pN durch das angelegte Potential moduliert werden.
- In zahlreichen technologischen Anwendungen ist nicht nur die Kontrolle der elektrostatischen Adhäsion von geladenen Polymeren von großem Interesse, auch eine elektrisch gesteuerte Chemisorption würde eine Vielfalt von neuen Anwendungsmöglichkeiten bieten. Deshalb wurde die Wechselwirkung von dsDNA mit einer Goldelektrode für verschiedene angelegte Spannungen gemessen, wobei die dsDNA wieder an die AFM-Spitze angebunden war. Dabei stellte sich heraus, dass dsDNA ausschließlich mit ihren Enden über koordinative Stickstoff-Gold-Bindungen auf die Elektrode chemisorbiert. Weiterhin wurden die komplexen elektrochemischen Bedingungen bestimmt, unter denen diese kontrollierte "Elektrosorption" von dsDNA an Gold möglich ist. Die Bildung von N-Au-Bindungen zwischen primären Aminen der Basen und der Goldelektrode wurde nachgewiesen, indem systematisch die Endsequenz der Nukleotide am freien Ende der dsDNA va-

---

riert wurde. Kraftspektroskopische Experimente mit einzelnen Adenosin-Nukleotiden an einem PEG-Spacer zeigten eine N-Au Bindungskraft von 170 pN, was in sehr guter Übereinstimmung mit Modellrechnungen ist. Für die letzten zwei Studien wurde zum ersten Mal AFM basierte Kraftspektroskopie an einzelnen Molekülen mit elektrochemischen Techniken kombiniert.

Die neuen dreidimensionalen Messprotokolle zur Bestimmung der Konformation und der Reibung von adsorbierten Polymeren und die Kombination von AFM und Elektrochemie zur Kontrolle der Adhäsion oder Bindung von Polymeren auf Oberflächen lassen eine Vielzahl von weiteren experimentellen oder theoretischen Arbeiten und technologischen Anwendungen versprechen.



# Contents

<b>1</b>	<b>Introduction</b>	<b>2</b>
<b>2</b>	<b>Scaling Exponent and Kuhn Length of Pinned Polymers</b>	<b>5</b>
2.1	Conformation of polymers . . . . .	5
2.2	Conformation measured by 3D force spectroscopy . . . . .	7
	F. Kuhner, M. Erdmann and H. E. Gaub, <i>Physical Review Letters</i> <b>97</b> (2006)	12
<b>3</b>	<b>Friction of Single Polymers on Surfaces</b>	<b>18</b>
3.1	Polymer mobility . . . . .	18
3.2	Measuring the friction of single polymers by AFM . . . . .	21
	F. Kuhner, M. Erdmann, L. Sonnenberg, et al., <i>Langmuir</i> <b>22</b> , 11180 (2006)	24
<b>4</b>	<b>Electrical controlled DNA adhesion</b>	<b>32</b>
4.1	Desorption force, applied potential and surface charge . . . . .	32
4.2	Electrical manipulation of the desorption force . . . . .	34
	M. Erdmann, R. David, A. R. Fornof and H.E. Gaub, <i>Nature Nanotechnology</i> , accepted (2009) . . . . .	38
<b>5</b>	<b>Bonding DNA to gold</b>	<b>57</b>
5.1	Electrochemistry of the gold surface . . . . .	57
5.2	Electrochemical induced DNA-gold bonding . . . . .	59
	M. Erdmann, R. David, A. R. Fornof and H.E. Gaub, submitted (2009) . . .	65
<b>6</b>	<b>Outlook</b>	<b>87</b>
<b>A</b>	<b>Bibliography</b>	<b>88</b>
<b>B</b>	<b>AFM, potentiostat and polymers</b>	<b>94</b>
B.1	AFM basics . . . . .	94
B.2	Basic principles of potential control . . . . .	96
B.3	Polymers: CMA, PAAM and DNA . . . . .	98
<b>C</b>	<b>Publications in preparation</b>	<b>101</b>
	<b>Acknowledgment</b>	<b>102</b>

# 1 Introduction

*Nothing is particularly hard if you divide it into small jobs.*

- Henry Ford

Nature uses this bottom-up approach to organize life and complex biological structures or materials by starting at the very basic level of atoms and molecules. The fundamental principle of self-assembly by molecular recognition and controlled chemical reactions help to establish individual functional nanometer-sized units. The interplay between these differently assembled molecular units delivers the form and function of life in our macroscopic world.

Of course nature's molecular processes of life cannot be summarized within a single paragraph, but they can be studied in detail: the fast growing field of nano(bio)-technology aims to investigate and to manipulate structures and materials at the molecular level. Thereby, physical and chemical techniques and theories are employed to understand the principles of molecular arrangement or functionality and to create new technological applications.

From the physical point of view, an essential aspect is to understand the dynamic intra- and intermolecular forces, which are responsible to form stable molecules and define the interactions between them. In order to measure forces on the order of Piconewtons ( $10^{-12}$  N), several nanotechnological techniques have been developed such as optical tweezers, magnetic traps or the **atomic force microscopy (AFM)**. Due to its high resolution in time, location and force, the atomic force microscope [1] has proven to be an universal instrument for imaging and force spectroscopy of biological soft matter under physiological conditions (buffered salt solutions at room temperature) [2, 3]. Thereby, the origin of AFM based single molecule force spectroscopy lies in the investigation of dissociation and extension forces of single biopolymers [4, 5]. Biopolymers such as proteins, carbohydrates and DNA are prominent representatives of nature's diversity and are involved in virtually every process within cells. Typically for **polymers**, these macromolecules are composed of repeating structural units (amino acids, sugars and nucleotides), which are generally called monomers [6].

But polymers play not only a crucial role in nature, also industrial polymers like polyethylene, polyamide or polyester can be found in countless products today. Besides the common use of polymers in form of plastic, complex applications of polymers in fields like polymer electronics (OLED displays, solar cell, RFID tags etc) or functional surface coatings (paints, adhesives, composite materials) are evolving. Thereby, polymers are typically interacting with solid substrates and are called **adsorbed polymers** in case of physical attachment to the surface. The force, which is necessary to "peel off" or desorb such an adhered polymer is called the **desorption force** and can be measured by AFM. The desorption force is contributed to van-der-Waals, hydrophobic and

coulombic interactions (physisorption). In contrast, polymers can also be chemically pinned or grafted via covalent bonds at a single point to the surface (chemisorption). The **rupture force**, which is necessary to break the bonding between polymer and surface can be determined by AFM as well.

The functionality of polymers on the surface is mainly governed by their adhesion strength or bonding to the substrate and their static and dynamic characteristics. Investigating these parameters is essential to provide for instance new functional coatings or lubricants and adhesives. The static and dynamic characteristics are determined by the **conformation** - or spatial structure - and the **lateral mobility** of the polymer on the surface. The size and structure of a polymer on a surface is given by its conformation. Thus, knowing its conformation answers for example questions, if the polymer adsorbs completely to the surface or forms protruding loops and trains or how strong is the polymer folded. Information about its lateral mobility is, for example, necessary to manipulate adsorbed polymers in further nanoscale applications or to create new exchangeable, but adhesive coatings.

One aspect of this thesis is the determination of the conformation and the lateral mobility of several adsorbed polymers, which could not be measured by conventional techniques. Therefore, new AFM measurement protocols were developed, which expanded the known force measurement from one to three dimensions. Thus, the static scaling exponent of highly mobile carboxy-methyl-amylose and the friction coefficient of a single polyallylamine polymer on a mica surface could be measured. Moreover, the friction of DNA on surfaces could be qualitatively characterized. Furthermore, the influence of horizontal force components in AFM measurements was investigated.

As described above, the adhesion strength of polymers on surfaces is essential, also in view of a controlled assembly of single molecules. Recently it was shown to pick up and deliver single DNA strands to a defined position in an aqueous environment at room temperature (Single Molecule Cut&Paste, [7]). Thereby, the angstrom precision of the AFM and the selectivity of DNA hybridization was used to overcome the "sticky finger problem" in nanotechnology [8]: a controlled delivery of molecules was claimed to be not possible due to the unspecific (e.g. van-der-Waals) interactions between molecule and the manipulator. However, this problem was solved by a passive hierarchy of interaction forces between different DNA strands. Nevertheless it would be highly desirable to control by an external parameter, whether or not a molecule is delivered, e.g. electrically. Moreover, the interaction of DNA with solid substrates is of utmost interest for numerous technological and biological applications, like DNA biochips or sensors [9, 10, 11], DNA templated wire formation [12] and DNA origamis [13, 14, 15]. Thus, an external electrical control of these processes would be of great advantage to new applications.

For this reason, the investigation of the **electrical control of DNA adhesion and bonding** constitutes the second part of this thesis. On the one hand, the adhesion of DNA to a chemically modified electrode was controlled via the electrode potential. Thereby, the desorption force could be adjusted by the applied potential and then measured by AFM. Also, DNA adhesion could be suppressed at all. Thus, the control of the

coulombic interaction between DNA and electrode established a fully reversible system based on physisorption. On the other hand, single DNA molecules were directed with the AFM to a chosen position on a gold electrode. There they were bonded with one end to the gold surface under controlled electrochemical conditions. This formation of coordinate bonds between DNA and gold was sensitively dependent on the electrochemistry of the surface. In other words, an externally triggered chemisorption or "electrosorption" of single molecules could be realized. For these studies, single force spectroscopy was combined with electrochemically techniques for the first time.

As mentioned in the beginning of the introduction, splitting problems into smaller parts is often helpful. The challenge to understand and manipulate single polymers on surfaces was partly simplified by investigating their conformation, mobility and adhesion/bonding mechanisms. Merging these parts again may provide new applications or devices and building blocks on the molecular scale. Also macroscopic implementations such as an "electric glue" could be conceivable ...

### **Structure of this thesis**

These perspectives and possible applications can be found in the Outlook chapter of this cumulative thesis. Prior to this, the introduced studies will be summarized in detail in chapters 2 to 5. Each chapter will also provide a brief theoretical introduction. For further detailed information, please refer especially to the Supporting Information of the corresponding publication. In the appendix, a quick and basic presentation of AFM, used polymers and electrochemistry will be given. Finally, studies in preparation are attached, which are based on the information in chapter 5.

# 2 Scaling Exponent and Kuhn Length of Pinned Polymers

As described in the introduction, the characteristic properties of adsorbed polymers are also governed by their conformation and dynamics on the surface. This chapter addresses the determination of the conformation of polymers, which are adsorbed on a surface and exhibit a high in-plane mobility. Thereby, a new three dimensional force spectroscopy approach was developed to determine the scaling exponent and the Kuhn length of such polymers. As a side effect, the influence of tangential contributions to the normal force in single molecule force spectroscopy experiments was investigated.

## 2.1 Conformation of polymers

### Ideal chains

The conformation - or spatial structure - of polymers has been described by numerous theories and scaling laws [16, 17]. In a first approximation, the model of an ideal chain is frequently used. Here, a polymer with the total contour length  $L_C$  is divided into  $N$  parts with length  $b$ :

$$L_C = bN. \quad (2.1)$$

In the **freely jointed chain model (FJC)**, the length  $b$  is called Kuhn length and is a measure of flexibility: the more Kuhn segments or "chain links" with length  $b$  a polymer provides, the higher is its flexibility. The structure of the polymer is then described by a simple **random walk**, whereby the Kuhn segments are described by  $b = |\vec{r}_i| = \text{const}$ . Furthermore, there are no correlations between the directions of the different bond vectors. The **end-to-end distance** of  $N$  Kuhn segments is then

$$\vec{R} = \sum_{i=1}^N \vec{r}_i. \quad (2.2)$$

As the name explains, the end-to-end distance is simply the distance between the first and last segment of the polymer and is a measure for the size or "volume" of a folded polymer. The average end-to-end distance for an isotropic collection of polymer chains is zero:

$$\langle \vec{R} \rangle = 0, \quad (2.3)$$

as there are no preferred directions in an ensemble of random walk distributed polymers. However, the first non-zero average is the mean-square end-to-end distance:

$$\begin{aligned}\langle R^2 \rangle &\equiv \langle \vec{R}^2 \rangle = \langle \vec{R} \cdot \vec{R} \rangle = \left\langle \left( \sum_{i=1}^N \vec{r}_i \right) \cdot \left( \sum_{j=1}^N \vec{r}_j \right) \right\rangle \\ &= \sum_{i=1}^N \sum_{j=1}^N \langle \vec{r}_i \cdot \vec{r}_j \rangle.\end{aligned}\quad (2.4)$$

Furthermore, the inner product of two Kuhn segments  $\vec{r}_i$  and  $\vec{r}_j$  with angle  $\theta_{ij}$  is:

$$\vec{r}_i \cdot \vec{r}_j = b^2 \cos \theta_{ij}.\quad (2.5)$$

Thus, the mean-square end-to-end distance can be directly calculated:

$$\begin{aligned}\langle R^2 \rangle &= \sum_{i=1}^N \sum_{j=1}^N \langle \vec{r}_i \cdot \vec{r}_j \rangle = b^2 \sum_{i=1}^N \sum_{j=1}^N \langle \cos \theta_{ij} \rangle \\ &= Nb^2,\end{aligned}\quad (2.6)$$

as  $\langle \cos \theta_{ij} \rangle = 0$  for  $i \neq j$  and  $\langle \cos \theta_{ij} \rangle = 1$  for  $i = j$  due to the missing preferred directions in a random walk. The root-mean-square end-to-end distance is then

$$R_0 = \sqrt{\langle R^2 \rangle} = bN^{1/2}.\quad (2.7)$$

In other words, the size of a folded polymer with the contour length  $L_C = bN$  grows proportional with the square root of the number of Kuhn segments  $N$ .

### Flory theory

However, the random walk model of an ideal chain describes the structure of polymers only in a first approximation. In nature, bond angles may be fixed and limited as in case of double stranded DNA. Here, only torsional movements along a bond angle are allowed. For example, the worm-like-chain model (WLC), which is a special case of the freely rotating chain model, is frequently used to describe these stiff polymers.

Unfortunately, these approaches do not consider interactions between the segments of a polymer. Depending on the solvent, these interactions can be either attractive or repulsive. This leads to the concepts of an **excluded volume** and **self-avoiding random walks**. The **Flory theory**, which estimates roughly the energetic and entropic contributions to the free energy of polymer, leads to an end-to-end distance for a three dimensional polymer

$$\langle |R_F| \rangle \approx v^{1/5} b^{2/5} N^{3/5}.\quad (2.8)$$

$v \approx b^3$  is the excluded volume and yields then

$$\langle |R_F| \rangle \approx bN^{3/5}.\quad (2.9)$$

In general, the Flory theory delivers a universal power law, which describes the dependence of the end-to-end distance  $R$  on the number of segments  $N$  of a polymer:

$$\langle |R| \rangle \approx bN^\nu. \quad (2.10)$$

More realistic theories yields for the scaling exponent  $\nu = 1, 0.75, 0.588$  and  $0.5$  for dimensions  $d = 1, 2, 3$  und  $d \geq 4$ .

Thus, the size or "swelling" of polymer with  $N$  segments is mainly governed by the scaling exponent  $\nu$ , which is independent of the excluded volume  $v$ . Furthermore, the scaling law leads to the concept of **self-similarity**: the end-to-end distance of an arbitrary section within a polymer obeys the same scaling law as the end-to-end distance and contour length of the whole polymer. In particular, the scaling exponent  $\nu$  will be the same in both cases; this feature is illustrated in Figure 2.1. In the subsequent paragraphs, this self-similarity will be employed in order determine the Kuhn length  $b$  and the scaling exponent  $\nu$  of adsorbed, but highly mobile polymers.

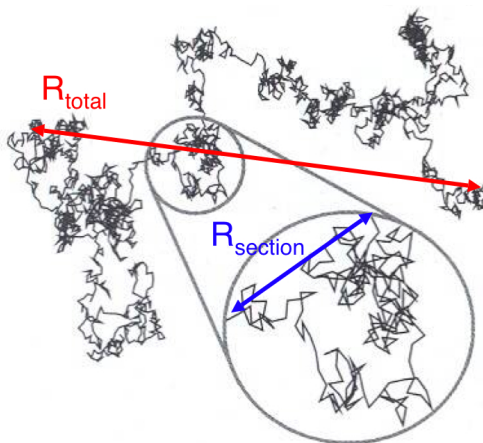


**Figure 2.1** Polymers are fractals: according to Equation 2.10, the same scaling exponent  $\nu$  describes the end-to-end distance  $R_{\text{section}}$  of an arbitrary section and the end-to-end distance  $R_{\text{total}}$  of the whole polymer itself (picture adapted from [17]).

## 2.2 Conformation measured by 3D force spectroscopy

In general, several experimental approaches have been realized to resolve the conformational properties of polymers. Ensemble techniques, such as light scattering, corroborated theoretical predications on scaling laws [18, 19]. Fluorescent imaging [20, 21] and scanning probe techniques [22, 23] could also shed light on conformational properties of single polymers on surfaces. However, both procedures require special experimental conditions: in the first case, the polymers have to be fluorescently labeled. The latter case demands high friction forces between polymer and substrate, otherwise the AFM tip would dislocate the polymer while scanning. Thus, high-resolution imaging

of adsorbed polymers with a high in-plane mobility is not possible, although these systems would be ideal model systems for polymer solutions with reduced dimensionality. Therefore, information on the conformation could not be gained so far.

### Experimental strategy

Single molecule force spectroscopy experiments could reveal individual intrinsic details of polymers, such as conformational transitions [2, 4] and solvent-mediated supramolecular rearrangements [24, 25], which are not resolvable in averaging ensemble experiments. Therefore, the following system was chosen in order to demonstrate a new force spectroscopy approach, which overcomes the discussed challenges: carboxymethylamylose (CMA) is a weakly negatively charged polysaccharid, which adsorbed well on an amino functionalized glass surface being positively charged by pH. Moreover, CMA is highly mobile on the amino glass surface. Long desorption force plateaus between 8 - 9 pN were measured (see Supporting Information), which result in an adsorption enthalpy of little more than  $k_B T$  for a polymer segment on the order of the Kuhn length ( $b = 0.45$  nm). The large-scale mobility of CMA was then restricted by covalently pinning it just at one point to the surface at a low density [26]. Thereby, the conformational freedom of the polymer in 2D was unaltered.

The AFM tip was then lowered to the surface and picked up randomly such a pinned CMA polymer (indentation above a certain threshold enables the attachment of the CMA polymer to the AFM tip [4]). Thereby, an arbitrary polymer section between the pinpoint and the pickup point was defined. As explained above, the distance between these two points on the surface  $R$  and the contour length  $L_C$  of this polymer section obey the same scaling law as the end-to-end distance and the contour length of the entire polymer. Thus, the measurement of these two sectional lengths defined by the pickup process provided the scaling exponent  $\nu$  according to Equation 2.1 and Equation 2.10:  $\langle |R| \rangle \approx L_C^\nu \cdot b^{1-\nu}$ . Measuring several polymer lengths yields then the Kuhn length  $b$  by extrapolation in double logarithmic plot of  $\langle |R| \rangle$  vs.  $L_C$ . When the AFM tip is

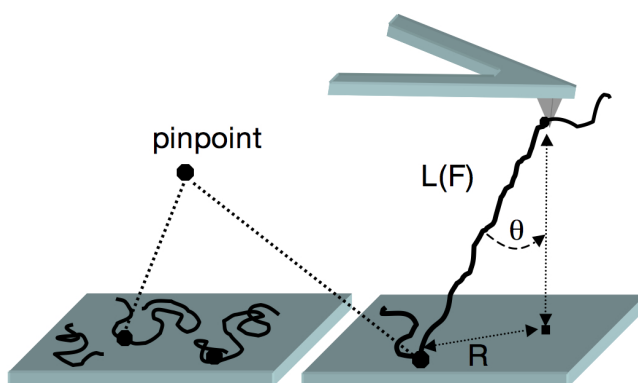


**Figure 2.2** Schematics of the experimental strategy. Polymers were covalently pinned onto a surface at very low density, restricting only their overall diffusion, not their segment mobility. Individual polymers were randomly picked up with an AFM tip cantilever tip and stretched.



retracted normal to the surface, the end-to-end distance  $R$  is simply the projection of the stretched polymer onto the surface, compare Figure 2.2. To determine the position of the pinpoint relative to the tip position, the tip was then scanned at constant height. Thereby, the force measured in the z-direction by the AFM changed depending on the position of the AFM tip relative to the pinpoint, as the CMA polymer was stretched at different extensions. Thus, the angle  $\theta$  changed continuously as well. As a consequence, horizontal force components were also acting on the tip, whereby a torque was exerted on the tip. This resulted in an additional bend of the asymmetric shaped cantilever (Figure 2.3 B), which leads to a cross talk of the lateral forces into the measured normal force. This effect needed first to be evaluated to correct asymmetric bending effects of the cantilever.

### Contribution of horizontal force components

This problem was analyzed by measuring the force acting on the cantilever for different pulling geometries. Thereby, the force-induced lengthening of the pyranose rings of CMA from their ground state chair conformation ( ${}^4C_1$ ) to the boat conformation was used as an internal force sensor [4, 27]. When the polymer is stretched vertically to

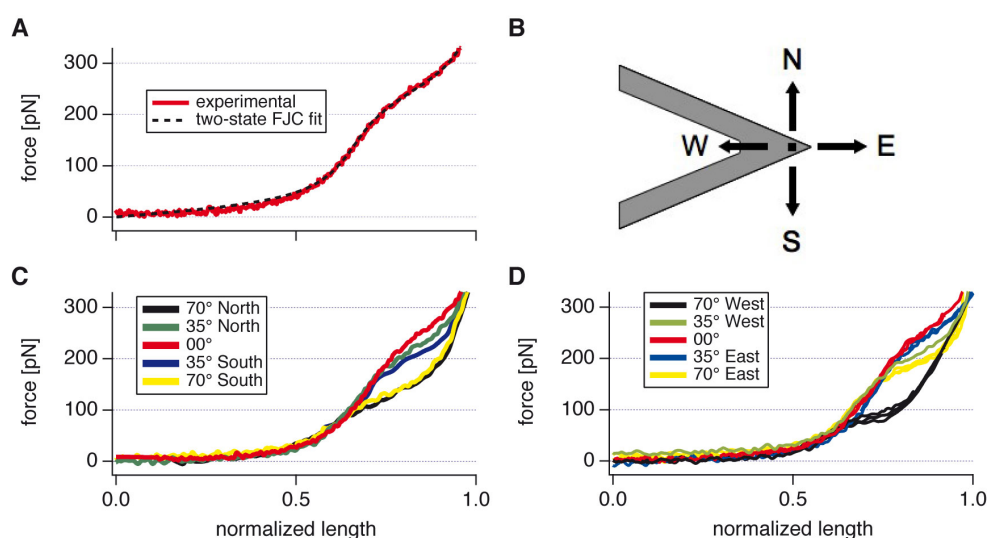


**Figure 2.3** Force extension curve (A) for a long CMA polymer, with the two-state FJC fit (dashed black line). Between 200 and 300 pN, the pyranose rings change their conformation, which was used as an internal force sensor in the polymer. In (B), the geometry of the cantilever is sketched. Normal forces acting on the cantilever tip result in an out-of-plane bend of the cantilever along the east-west direction. This bend is measured with the reflected laser beam and after calibration converted into a force. Tangential forces acting on the tip result in a torque and cause an additional bend of the cantilever. However, only the east-west components of the lateral forces are picked up this way. The north-south components are not detected. This effect can be seen in (C) and (D), where this bend is measured when pulled at an angle with respect to the surface. Whereas in the north-south direction (C) the transition force decreases with the angle, the force additionally differs markedly, when pulled east or west (D).

the surface, this internal transition occurs at approximately 275 pN and can be seen as force "hump" in the force extension curve (Figure 2.3 A). The two conformations of the segments are modeled by a two-level system according to the force dependent FJC model with  $N_{ground}/N_{boat} = \exp(\Delta G/k_B T)$  [25]. The length of a polymer  $L$  is calculated in dependence of an applied force  $F$ :

$$L(F) = N_S \left( \frac{L_{ground}}{e^{-\Delta G/k_B T} + 1} + \frac{L_{boat}}{e^{+\Delta G/k_B T} + 1} \right) \times \left( \coth \left( \frac{F L_K}{k_B T} \right) - \frac{k_B T}{F L_K} \right) + N_S \frac{F}{K_S}. \quad (2.11)$$

$N_S$  is the total number of segments,  $L_{ground}$  and  $L_{boat}$  are the length of the conformation of the stress-free and under-stress pyranose rings, respectively.  $L_K$  is the Kuhn length (a different symbol for the Kuhn length is used as before to distinguish that they were derived differently),  $K_S$  the segment elasticity, and  $\Delta G$  the free energy difference. For the fit in Figure 2.3 A, literature values were used [28]:  $L_{ground} = 0.45$  nm,  $L_{boat} = 0.54$  nm,  $L_K = 0.45$  nm,  $K_S = 28$  N/m, and  $\Delta G = 6 k_B T$ . In general, the only free fit parameter is the contour length  $L_C = L_K N_S$ . Thus, the number of segments of CMA can be directly determined by vertical force extension curves, when the CMA polymer is not stretched at an angle ( $\theta = 0$ ).

As a next step, the cantilever was retracted from the surface with different directions (north, south, east, west) and angles (Figure 2.3 B). Thereby, different forces in the  $z$ -direction for the same internal conformation transition of CMA were measured (Figure 2.3 C and D). With regard to the north-south direction, the normal force decreased symmetrically in both directions with a factor of  $\cos(\theta)$ . Due to the lateral stiffness of the cantilever, deflections in these directions are not possible for the range of applied forces. However, the same experiment in the asymmetric east-west direction revealed

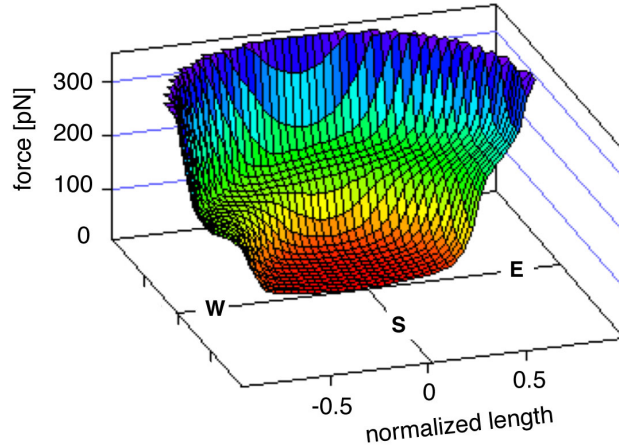


**Figure 2.4** Master-force map of a CMA molecule generated by interpolation between many force curves such as the ones in Figure 2.3. It gives the normal force component when the tip is scanned above the surface at a constant height of 1/3 of its total length. The asymmetry of the force map reflects the cantilever asymmetry as described before.

marked differences for the detected forces, at which the transition occurred. The torque increases (east) or reduces (west) the deflection of the cantilever caused by the normal component of the backbone force (compare the black and yellow curves in Figure 2.3). To summarize, at the same backbone force, the measured deflection signal of the AFM cantilever depends on angle and direction!

For a precise measurement of the polymer pinpoint, this needs to be taken into account. From the interpolation between many such curves as shown in Figure 2.3 C and D, a force map was created (Figure 2.4). In this simulation of the normal component of the force acting on the CMA backbone, the polymer is pinned at the origin at zero position, where it is also picked up by the AFM tip. The AFM tip scans in this simulation above the surface at a constant height of  $1/3$  of the total polymer length. Assuming that the pinpoint would be shifted, the force map would be also shifted relative to the zero position of the AFM tip. Therefore, this force map can be used to determine the distance between pickup point and pinpoint (the end-to-end distance) in an experiment shown in Figure 2.5 A.

### Measuring the end-to-end distance and contour length

First, the AFM tip picked up a CMA polymer and desorbed it from the surface by moving back to a certain distance. In this height, the tip was then moved in squares with increasing diameter while the force in z-direction was recorded (Figure 2.5 B). This experimental force map is quite asymmetric, as the pinpoint was located in an end-to-end distance of  $R = 88.2 \pm 7.7$  nm southwest of the pickup point. After the horizontal scan, the AFM tip could be moved to the pinpoint. Finally, the contour length  $L_C = 274 \pm 3.8$  nm was determined by a normal force extension curve, which was fitted with the FJC model (Equation 2.11).

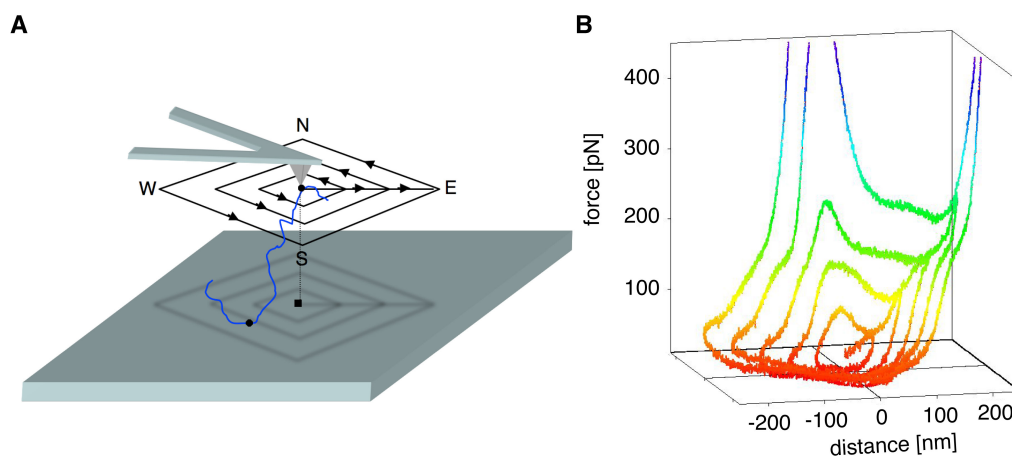


**Figure 2.5** In (A), the protocol for the cantilever motion is sketched. The cantilever is retracted and scanned parallel to the surface while the force is recorded. (B) The resulting force curve. Obviously, only a segment of the entire force map was visited. In comparison with the master curve, the pinpoint was localized southwest of the origin (see Figure 2.4).

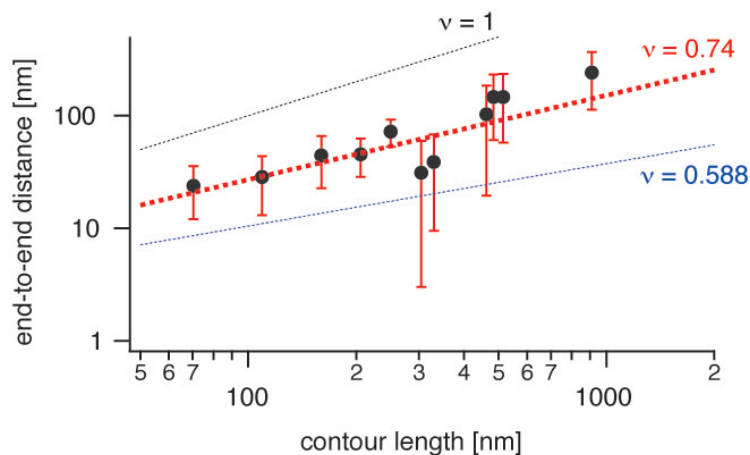


**Figure 2.6** End-to-end distance of CMA-polymer sections plotted against their contour length. The red dashed line is the fit with a scaling factor of  $0.74 \pm 0.04$  and a segment length of  $b = 0.44 \pm 0.14$  nm. The blue and black dotted lines are plots with  $\nu = 0.588$  and  $\nu = 1$  with  $b = 0.44$  nm, respectively.

This procedure was repeated for 97 CMA sections with different contour lengths  $L_C = bN$ . The measured end-to-end distances (binned with  $\pm 10$  nm) were plotted double logarithmically against their contour lengths as depicted in Figure 2.6. From the slope, the scaling factor  $\nu$  was determined to be  $0.74 \pm 0.14$ , which is close to the expected value for a 2D polymer. This signifies that the polymer rearranges on the surface after adsorption. Contrary to this 2D conformation, CMA exhibits a 3D scaling factor  $\nu = 0.588$  in solution. If the CMA formed pronounced 3D loops and trains on the surface, a different scaling factor than the 2D value would have been observed. Moreover, the y-intercept provides a Kuhn length of  $b = 0.44$  nm, if one assumes equality in Equation 2.10. This value is in good agreement with the Kuhn length  $L_K$  derived from FJC fits and the chemical structure for a single pyranose ring [27].

To summarize, the conformational parameters of adsorbed CMA polymers on an amino surface could be determined with a new 3D force spectroscopy approach. As a side effect, the horizontal force contributions in angular force spectroscopy experiments were investigated and the force detection was calibrated in view of different pulling directions and angles. Therefore, new structural insights for adsorbed, tethered, pinned or grafted polymers could be gained, which are not resolvable with conventional techniques. Furthermore, the 3D force spectroscopy approach will be used in the next chapter to investigate not only structural, but also dynamic parameters of adsorbed polymers.

## Scaling Exponent and Kuhn Length of Pinned Polymers by Single Molecule Force Spectroscopy

Ferdinand Kühner, Matthias Erdmann, and Hermann E. Gaub

Chair for Applied Physics and Center for NanoScience, Ludwig-Maximilians Universität München, Munich, Germany

(Received 7 April 2006; published 20 November 2006)

The end-to-end distance and the contour length of single polymers in dynamic adsorbate layers were measured with a mechanical approach. Individual polysaccharide chains were covalently pinned to the surface with one segment and picked up randomly with an atomic force microscope tip. The polymer section between pinpoint and the pickup point was stretched by retracting the tip from the surface. The pinpoint was derived by measuring the normal force while laterally scanning the surface at constant height. For carboxy-methyl-amylose, a Kuhn length of 0.44 nm and a scaling exponent of 0.74 were found.

DOI: 10.1103/PhysRevLett.97.218301

PACS numbers: 82.35.Gh, 82.35.Jk, 82.37.Gk

Both conformation and dynamics of polymers govern their function in numerous applications, e.g., as coatings, adhesives, in composite materials, or the like. A rich body of literature on both theory [1–4] and modeling exists [5,6], and a wealth of experimental data is available [7]. Ensemble measurements, such as light scattering [8,9], have in many instances corroborated theoretical predictions on the scaling of the end-to-end distance of a polymer  $\langle |R| \rangle$  and  $N$ , the number of segments which follows  $\langle |R| \rangle \approx bN^\nu$ . Here  $b$  is the Kuhn length and  $\nu$  the critical exponent, which depends on the dimension of the system and has a value of  $\nu = 1, 0.75, 0.588$ , and  $0.5$ , for  $d = 1, 2, 3$ , and  $d \geq 4$ , respectively [1]. If one expresses the number of units  $N$  by the contour length  $L_c = bN$ , both the end-to-end distance  $\langle |R| \rangle$  and  $L_c$  are linked by the simple relation  $\langle |R| \rangle \approx L_c^\nu b^{(1-\nu)}$ . A double logarithmic plot of the end-to-end distance  $\langle |R| \rangle$  against  $L_c$  should thus result in a linear dependency and provide  $\nu$ .

Since ensemble experiments average over a large population of polymers, individual details of the polymer molecules remain hidden, and, in polydisperse samples, length-dependent deviations are concealed. Single molecule experiments overcome such obstacles. Conformational transitions (dextran [10], titin [11], or DNA) and solvent-mediated supramolecular rearrangements were discovered [12,13], and new models for the polymer elasticity based on an interplay between backbone deformations and entropic conformations were developed [14–16].

For polymers at surfaces, scanning probe techniques were employed *in situ* and on dried samples [17–22]. However, under conditions where the lateral mobility of the polymers exceeds the cantilever scanning speed, no high-resolution imaging is possible. Recently, we and others discovered that weakly adsorbed polymers might exhibit an unexpectedly high in-plane mobility [23], although their adhesion enthalpy per segment exceeds several  $k_B T$  resulting in a quasi-irreversible adsorption already at short polymer lengths [24–26]. Because of the high in-plane mobility, information on the conformation of the polymers could not be gained up to date, even though

such adsorbate layers are ideal model systems for polymer solutions with reduced dimensionality. In this Letter, we develop a strategy to derive the key parameters for the conformation, the Kuhn length  $b$  and the scaling exponent  $\nu$ , by measuring the contour length and the end-to-end distance of individual polymers. The experimental strategy is outlined in Fig. 1.

Carboxy-methyl-amylose (CMA) was covalently pinned to a glass slide [27,28] with such a low efficiency that the probability to pick up a polymer with the atomic force microscope (AFM) tip was less than 1%. The lateral density was confirmed by AFM imaging to be 12 molecules per  $\mu\text{m}^2$  (see supplementary material [29]). This low surface density of attachment sites also ensures that the vast majority of the polymers are bound to the surface only at one segment.

Pinning at one point just restricts the large-scale mobility but leaves the conformational freedom of the polymer in 2D unaltered. Since the amino functionalized glass surface is positively charged, the weakly negatively charged CMA polymer is expected to adsorb to the surface. We confirmed this in single molecule desorption measurements (see supplementary material [29]) where we found long force plateaus between 8–9 pN. This value converts

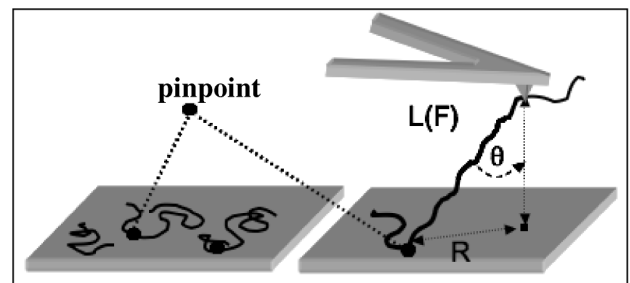


FIG. 1. Schematics of the experimental strategy. Polymers were covalently pinned onto a surface at very low density, restricting only their overall diffusion, not their segment mobility. Individual polymers were randomly picked up with an AFM-cantilever tip and stretched.

into an adsorption enthalpy of  $\approx 2k_B T/\text{nm}$  or little more than  $k_B T$  for a polymer segment on the order of the Kuhn length. According to different references [2,30], the polymer is expected to be thus largely restricted to the surface.

We now lowered an AFM tip to the surface and picked such a pinned polymer. We then stretched it upon retracting the tip from the surface (see Fig. 1). Many studies have shown that polymers may be attached to the tip of an AFM cantilever if the contact force is increased above a certain threshold [10,31]. Since the pickup of the pinned polymer at the surface is random, we define with this process an arbitrary section of the polymer between the pinning point and the pickup point. The distance between these two points on the surface and the contour length of this polymer section obey the same scaling law as the end-to-end distance and the contour length of the entire polymer. In particular, the scaling exponent  $\nu$ , which determines the degree of swelling of the polymer, will be the same in both cases, provided the section is much longer than the Kuhn length  $b$ .

The task is thus to measure the two lengths  $L_c$  and  $\langle |R| \rangle$ —the end-to-end distance, which the polymer had at the moment of the pickup—by retracting the tip from the surface in a suitable manner. Figure 1 highlights the geometry. Obviously, the polymer section is stretched at an angle  $\theta$  when the AFM tip is retracted normal to the surface, and the end-to-end distance is simply the projection of the stretched polymer onto the surface. An appropriate strategy would be to determine the position of the

pinpoint relative to the tip position. In principle, this could be achieved by scanning the tip at constant force. The tip would then move on a hemisphere with the pinpoint as the center. To avoid permanent high load on the polymer, we chose a scheme where the tip is scanned at constant height. Nevertheless, also here a basic difficulty arises from the fact that the cantilever geometry breaks the symmetry of the experiment. The horizontal components of the force, which act on the tip upon stretching a polymer, exert a torque on the tip. This results in an additional bend of the cantilever, which leads to a cross talk of the lateral forces into the measured normal force. This effect needs first to be evaluated in order to be able to correct for the asymmetric bending effects of the cantilever.

To analyze this problem, the force acting on the cantilever was measured for different pulling geometries. Figure 2(a) shows the force extension relation measured for a single CMA polymer, which was picked up following the procedure given above. The hump reflects the force-induced lengthening of the pyranose rings from their ground state chair conformation ( ${}^4C_1$ ) to the boat conformation [10,32,33]. In the following, we use this transition as an internal sensor for the force acting along the polymer backbone. The dashed line gives the best fit of the force extension relation based on the freely jointed chain model with enthalpic segment elasticity. The two conformations of the segments are modeled by a two-level system according to the following equation with  $N_{\text{ground}}/N_{\text{boat}} = \exp(\Delta G/k_B T)$  [13,34]:

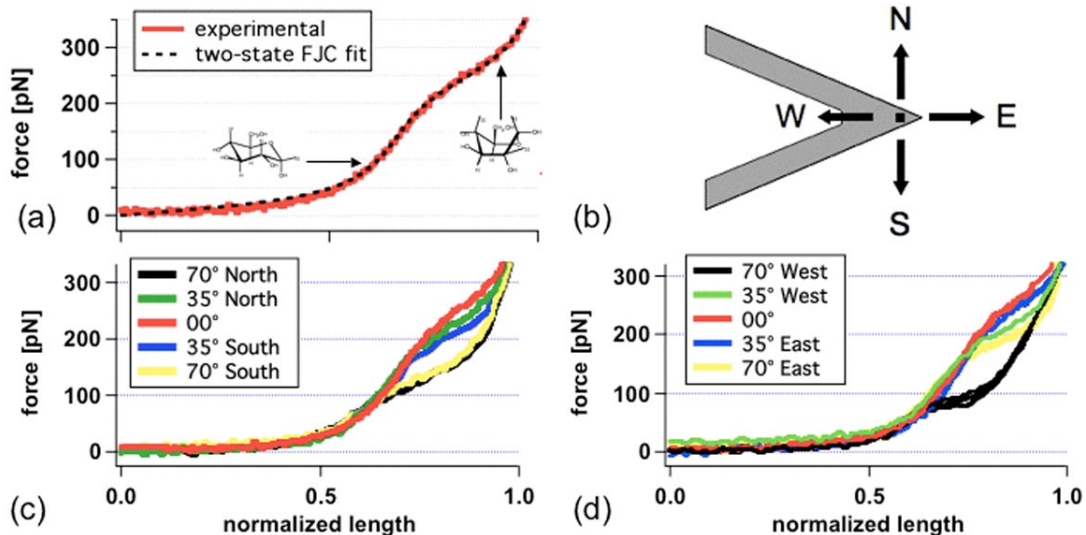


FIG. 2 (color online). Force extension curve (a) for a long CMA polymer, with the two-state FJC fit (dashed black line). Between 200 and 300 pN, the pyranose rings change their conformation, which was used as an internal force sensor in the polymer. In (b), the geometry of the cantilever is sketched. Normal forces acting on the cantilever tip result in an out-of-plane bend of the cantilever along the east-west direction. This bend is measured with the reflected laser beam and after calibration converted into a force. Tangential forces acting on the tip result in a torque and cause an additional bend of the cantilever. However, only the east-west components of the lateral forces are picked up this way. The north-south components are not detected. This effect can be seen in (c) and (d), where this bend is measured when pulled at an angle with respect to the surface. Whereas in the north-south direction (c) the transition force decreases with the angle, the force additionally differs markedly, when pulled east or west (d).

$$L(F) = N_s \left( \frac{L_{\text{ground}}}{e^{-\Delta G/k_B T} + 1} + \frac{L_{\text{boat}}}{e^{+\Delta G/k_B T} + 1} \right) \times \left[ \coth\left(\frac{FL_K}{k_B T}\right) - \frac{k_B T}{FL_K} \right] + N_s \frac{F}{K_s},$$

where  $N_s$  is the total number of segments,  $L_{\text{ground}}$  and  $L_{\text{boat}}$  are the length of the conformation of the stress-free and under-stress pyranose rings, respectively.  $L_K$  is the Kuhn length (we use a different symbol for the Kuhn length as before to distinguish that they were derived differently),  $K_s$  the segment elasticity, and  $\Delta G$  the free energy difference. For the CMA fit in Fig. 2(a), we used values from the literature:  $L_{\text{ground}} = 0.45$  nm,  $L_{\text{boat}} = 0.54$  nm,  $L_K = 0.45$  nm,  $K_C = 28$  N/m, and  $\Delta G = 6k_B T$  [35]. The only free parameter is the contour length ( $L_c = L_K N_s$ ) of the polymer, which is extracted from the fit with an accuracy of better than 1 nm [note: since  $\langle \sin(\theta) \rangle$  scales with  $N^{s-1}$ , particularly long polymers were chosen to reduce the cross talk of lateral forces]. As a control, we varied the Kuhn length in the fitting procedure and found the literature value to provide the best fit also for our curves. In Fig. 2(b), a polymer was picked up and stretched obliquely by retracting the tip at different angles towards the normal and in different directions relative to the cantilever geometry [cantilever  $C$  from MLCT-AUHW; Veeco Instruments GmbH, Mannheim, Germany. Deviations (for the west and east directions) occur at all cantilevers, because of the lateral asymmetry of the cantilever.]. As can easily be seen in Figs. 2(c) and 2(d), the conformation transition of the polymer occurs at different normal forces for different angles. Whether the tip was moved north or south had a negligible effect, as was to be expected.

The normal force acting on the cantilever decreases with the factor of  $\cos(\theta)$ . Figure 2(d) shows the same kind of experiment. However, here the difference in torque between east and west alters markedly the force at which the transitions occur. The torque increases (west) or reduces (east) the deflection of the cantilever caused by the normal component of the backbone force. To summarize, at the same backbone force, the measured deflection signal of the AFM cantilever depends on angle and direction. For a precise measurement of the polymer pinpoint, this needs to be taken into account.

From the interpolation between many such curves [36] as shown in Figs. 2(c) and 2(d), a force map was created (Fig. 3), which gives the normal component of the force acting on the sugar polymer that is pinned at the origin when the tip is scanned parallel to the surface at a certain height. The asymmetry of the cantilever results in marked distortion, which is best notable at the hump ring of the boat-chair transition. It should be pointed out here that a shift of the pinpoint of the polymer results in a shift of the force map relative to the zero position of the cantilever tip. This means that this force map can now be used as a master surface to analyze the force map measured on an arbitrary pinned polymer such as the one shown in Fig. 4. In this

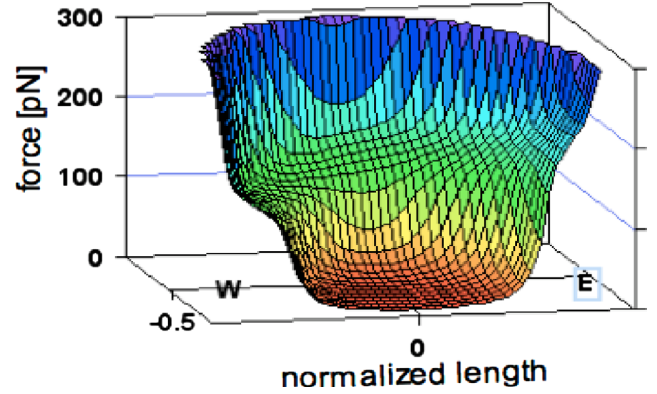


FIG. 3 (color online). Master-force map of a CMA molecule generated by interpolation between many force curves such as the ones in Fig. 2. It gives the normal force component when the tip is scanned above the surface at a constant height of  $1/3$  of its total length. The asymmetry of the force map reflects the cantilever asymmetry as described before.

experiment, the tip was moved along the trace depicted in Fig. 4(a). After the polymer was picked up, the tip was lifted normal and then scanned parallel to the surface in squares with increasing diameter. (By this approach, the polymer is pulled from 2D in 3D conformation. However, the anchor point of the polymer at one end, which is

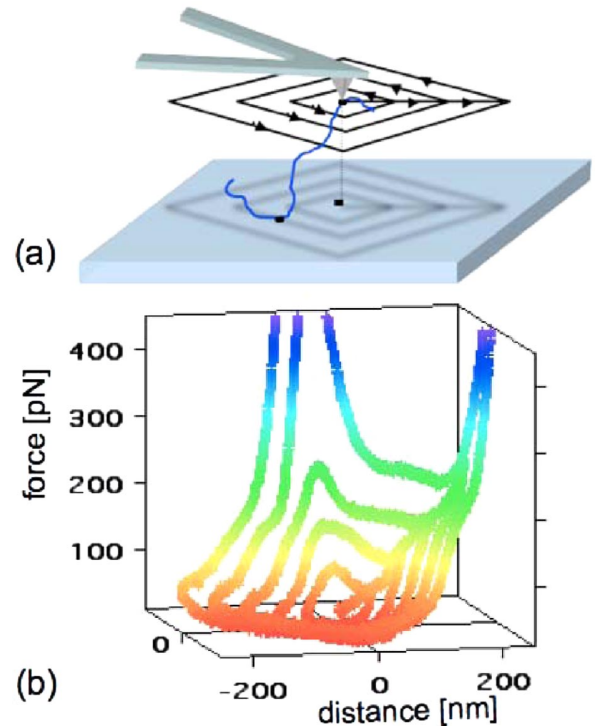


FIG. 4 (color online). In (a), the protocol for the cantilever motion is sketched. The cantilever is retracted and scanned parallel to the surface while the force is recorded. (b) The resulting force curve. Obviously, only a segment of the entire force map was visited. In comparison with the master curve, the pinpoint was localized southwest of the origin (see Fig. 3).

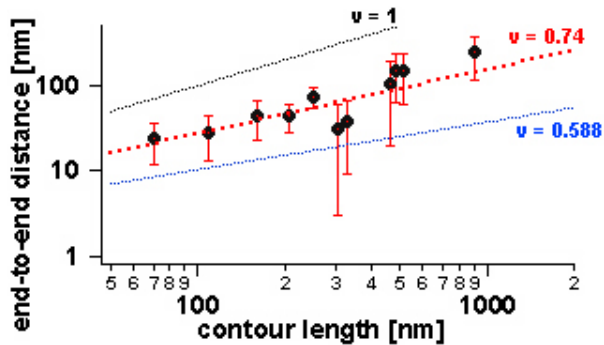


FIG. 5 (color online). End-to-end distance of CMA-polymer sections plotted against their contour length. The red dashed line is the fit with a scaling factor of  $0.74 \pm 0.04$  and a segment length of  $b = 0.44 \pm 0.14$  nm. The blue and black dotted lines are plots with  $\nu = 0.588$  and  $\nu = 1$  with  $b = 0.44$  nm, respectively.

determined by this step, is unaltered.) The measured normal force is shown in Fig. 4(b). As can be seen, the force map is quite asymmetric. This is because the pinpoint of the polymer is located southwest of the tip origin and so only roughly a quarter segment of the “bowl” was visited.

A set of polymers was investigated following the procedure given above; the distance between pinpoint and pickup point and as such the end-to-end distance of the polymer section were determined [37] by fitting the traces to the master-force map. (All data analysis was done by self-written procedures in IGOR 5.03.) Also determined was the contour length by fitting the extension traces of the polymer vertical to the surface.

In Fig. 5, the end-to-end distances (binned with  $\pm 10$  nm) of 97 CMA-polymer sections were plotted double logarithmically against their contour lengths. From the slope, the scaling factor  $\nu$  was determined to be  $0.74 \pm 0.04$ , which is close to the expected value for a 2D polymer (0.75). This signifies that the polymer rearranges on the surface after adsorption [38] and is highly dynamic [39].

If one would assume equality and not only proportionality in the scaling law for the end-to-end distance, the y intercept in Fig. 5 would provide the Kuhn length with a value of  $b = 0.44 \pm 0.14$  nm, which is in very good agreement with the Kuhn length  $L_K$  derived from the freely jointed chain (FJC) fits and the chemical structure for a single pyranose ring [40].

We envision that this approach to measure conformational parameters of dynamic polymers *in situ* is applicable to a broad spectrum of adsorbed, tethered, pinned, or grafted polymers. As a side effect, this study here has also shed light on the question of whether tangential contributions to the normal force in single molecule force spectroscopy experiments need to be considered.

We thank Erich Sackmann, Erwin Frey, Roland Netz, Lars Sonnenberg, and Richard Neher for helpful discussions and the DFG for financial support.

- [1] P.G. de Gennes, *Scaling Concepts in Polymer Physics* (Cornell University, Ithaca, 1979).
- [2] R.H.C. Michael Rubinstein, *Polymer Physics* (Oxford University Press, New York, 2003).
- [3] C. Holm *et al.*, in *Polyelectrolytes with Defined Molecular Architecture II*, Advances in Polymer Science Vol. 166 (Springer, New York, 2004), pp. 67-111.
- [4] O.V. Borisov *et al.*, *Eur. Phys. J. E* **6**, 37 (2001).
- [5] A. Milchev and K. Binder, *Macromolecules* **29**, 343 (1996).
- [6] E. Eisenriegler, K. Kremer, and K. Binder, *J. Chem. Phys.* **77**, 6296 (1982).
- [7] B. Maier and J.O. Radler, *Phys. Rev. Lett.* **82**, 1911 (1999).
- [8] J.P.C.M. Daoud, B. Farnoux, G. Jannink, G. Sarma, H. Benoit, C. Duplessix, C. Picot, and P.G. de Gennes, *Macromolecules* **8**, 804 (1975).
- [9] Y.E.Y. Miyaki and H. Fujita, *Macromolecules* **11**, 1180 (1978).
- [10] M. Rief *et al.*, *Science* **275**, 1295 (1997).
- [11] M. Rief *et al.*, *Science* **276**, 1109 (1997).
- [12] S. Cui *et al.*, *J. Am. Chem. Soc.* **128**, 6636 (2006).
- [13] F. Oesterhelt, M. Rief, and H.E. Gaub, *New J. Phys.* **1**, 6 (1999).
- [14] T. Hugel *et al.*, *Phys. Rev. Lett.* **94**, 048301 (2005).
- [15] J. Kas *et al.*, *Europhys. Lett.* **21**, 865 (1993).
- [16] C.M. Schroeder *et al.*, *Phys. Rev. Lett.* **95**, 018301 (2005).
- [17] C. Anselmi, P. DeSantis, and A. Scipioni, *Biophys. Chem.* **113**, 209 (2005).
- [18] F. Valle *et al.*, *Phys. Rev. Lett.* **95**, 158105 (2005).
- [19] H.G. Hansma *et al.*, *Nucleic Acids Res.* **21**, 505 (1993).
- [20] L. Bourdieu, P. Silberzan, and D. Chatenay, *Phys. Rev. Lett.* **67**, 2029 (1991).
- [21] J. Marek *et al.*, *Cytometry* **63A**, 87 (2005).
- [22] N. Severin *et al.*, *Nano Lett.* **6**, 1018 (2006).
- [23] F. Kühner, M. Erdmann, and H.E. Gaub, *Langmuir* (in press).
- [24] T. Hugel *et al.*, *Macromolecules* **34**, 1039 (2001).
- [25] M. Seitz *et al.*, *Chem. Phys. Chem.* **4**, 986 (2003).
- [26] X. Chatellier *et al.*, *Europhys. Lett.* **41**, 303 (1998).
- [27] Aminoslide\_A, Schott, Nexterion, Mainz, Germany.
- [28] F. Kühner *et al.*, *Biophys. J.* **87**, 2683 (2004).
- [29] See EPAPS Document No. E-PRLTAO-97-010647 for regular force curves desorbing CMA of the amino surface and imaging in tapping mode after critical point drying. For more information on EPAPS, see <http://www.aip.org/pubservs/epaps.html>.
- [30] P.G. de Gennes, *J. Phys. (Paris)* **37**, 1445 (1976).
- [31] M. Rief, H. Clausen-Schaumann, and H.E. Gaub, *Nat. Struct. Biol.* **6**, 346 (1999).
- [32] P.E. Marszalek, H. Li, and J.M. Fernandez, *Nat. Biotechnol.* **19**, 258 (2001).
- [33] P.E. Marszalek *et al.*, *Nature (London)* **396**, 661 (1998).
- [34] M. Rief, J.M. Fernandez, and H.E. Gaub, *Phys. Rev. Lett.* **81**, 4764 (1998).
- [35] H. Li *et al.*, *Chem. Phys. Lett.* **305**, 197 (1999).
- [36] F. Kühner and H. Gaub, *Polymer* **47**, 2555 (2006).
- [37] J. Wilhelm and E. Frey, *Phys. Rev. Lett.* **77**, 2581 (1996).
- [38] C. Rivetti, M. Guthold, and C. Bustamante, *J. Mol. Biol.* **264**, 919 (1996).
- [39] S. Manneville *et al.*, *Europhys. Lett.* **36**, 413 (1996).
- [40] P.E. Marszalek *et al.*, *Nature (London)* **396**, 661 (1998).



## Supplementary Material:

### Scaling exponent and Kuhn length of pinned polymers by single molecule force spectroscopy

Ferdinand Kühner, Matthias Erdmann and Hermann E. Gaub

#### AFM scan of a nitrogen dried CMA amino surface

The CMA was covalently link to the surface as described in the paper. After rinsing the sample was dried with nitrogen and scanned by the AFM. The hydrophilic polymer contracts while drying and is forming a ball with counterions and water molecules. The conformation has drastically changed comparing to the liquid environment. The only information, which is reserved, is the average density of CMA polymers bound to the surface. The density is approximately 12 molecules per  $\mu\text{m}^2$ .

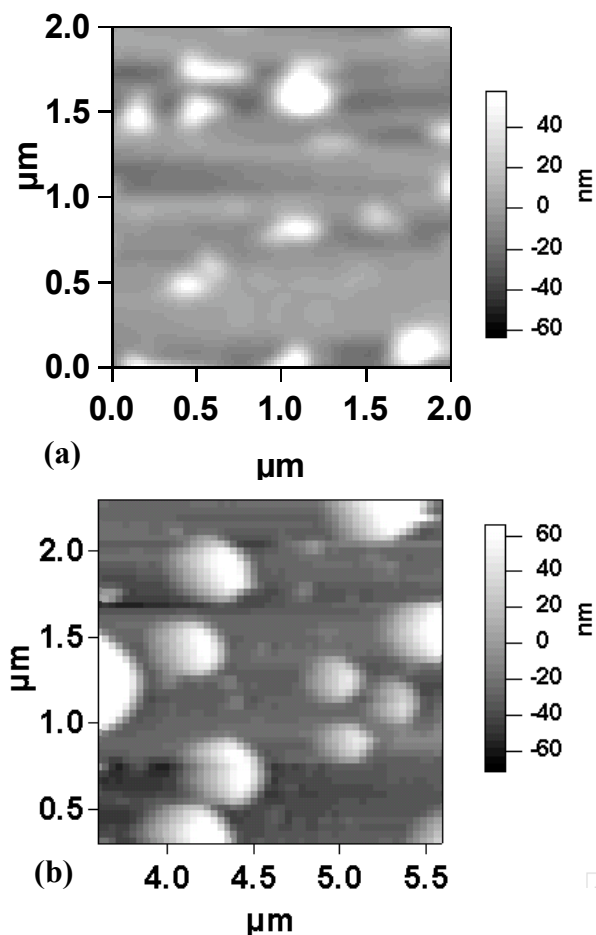


Figure A1. The AFM height signal in air of a nitrogen dried sample (a) and the height signal of a critical point dried sample (b). Drying leads to a collapse of the polymer polymers, which are covalently bound to an amino surface. However the averaged density of the polymers can be determined and results in approximately 12 molecules per  $\mu\text{m}^2$ .

To avoid the high water air surface tension, we performed critical point drying experiments. Therefore

the wet sample is closed in a chamber and filled up with isopropanol. The isopropanol is exchanged by liquid nitrogen and cooled to  $4^\circ$  until the sample is completely surrounded by liquid nitrogen. While heating the liquid does not intercept the phase transition and should therefore not lead to high stress on the polymers on the surface. However the results are not satisfied. The conformational change and the contraction to a polymer blob is even enhanced.

#### Desorption force curve of a CMA polymer

To test the absorption force of a CMA polymer on an amino surface, regular force distance curves were performed. In contrast to the sample described in the paper the CMA polymers were not exclusively covalently linked to the surface. Force plateaus in the force distance curves could be detected, which can be attributed to the desorption of the CMA polymer from the amino surface. Therefore the force distance curve must be filtered at very low frequencies by a low pass filter. The detected force at the moment of the rupture event has to overcome the thermal noise value in the force curve. Such a rupture event can be detected in figure A2 at about 185 nm. The force plateau has an averaged height of 8.3pN, which results in an absorption energy of approximately one  $k_B T$  per segment (0.44nm). According to Rubenstein (page ) the polymer the polymer is expected to be predominantly absorbed to the surface

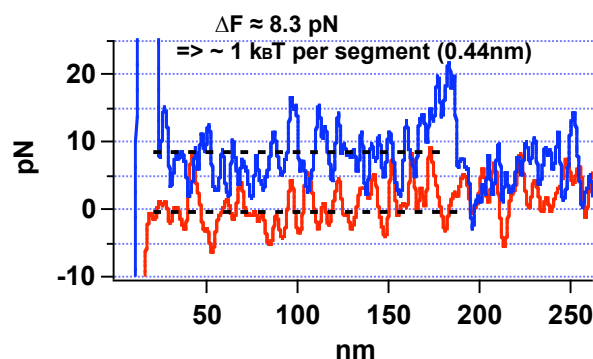


Figure A3. Desorption force curve of an absorbed CMA polymer. The polymer rupture is completely desorbed of the surface at about 185nm, which can be detected by the rupture event. The force plateau is very close to the resolution of the instrument. However the average difference of the retrace and trace curve result in a desorption force of 8.3pN.

# 3 Friction of Single Polymers on Surfaces

The last chapter introduced a new, three dimensional force spectroscopy approach in which the cantilever was moved parallel to the surface with a polymer being covalently pinned to the surface. In this study, the idea of retracting the cantilever not only vertical to the surface in the z-direction, but also parallel to the surface in the x-direction was applied to determine qualitatively the mobility of adsorbed polymers on different surfaces. Thereby, a new method to quantify the friction coefficient of an adsorbed, single polymer on a surface was established.

## 3.1 Polymer mobility

### Principles of force driven polymer motion

The mobility of single polymers is described by the Rouse model, in which the diffusion constant  $D$  and the **friction coefficient per segment**  $\zeta$  are related through the Einstein relation [17]:

$$D = \frac{k_B T}{N \zeta}, \quad (3.1)$$

where  $N$  is the number of segments of the polymer. Typical values are for example  $D = 5 \times 10^{-15} \text{ m}^2/\text{s}$  for a 1.4 kbp dsDNA polymer in solution and  $D = 5 \times 10^{-12} \text{ m}^2/\text{s}$  for a 1.2 kbp dsDNA polymer adsorbed on mica [29, 30]. The friction coefficients per base pair  $\zeta$  result in  $\sim 6 \times 10^{-10} \text{ N/s}$  and  $\sim 6 \times 10^{-13} \text{ N/s}$ , respectively. Such high diffusion constants can be directly measured with optical ensemble techniques such as fluorescence recovery after photobleaching (FRAP). However, systems with low diffusion constants require long measurement times. Limitations such as drift, bleaching or other side effects are expected. The analysis of AFM image sequence is then preferable although scanning artefacts are possible. In high friction regimes with even lower diffusion constants, the mobility due thermally driven diffusion may not be sufficient to be resolvable within experimental time scales.

To overcome these limitations, a horizontal force component was applied to a single adsorbed polymer in order to detect its mobility and rearrangement response. In a first approximation, the **microscopic friction force** for a single polymer on a surface scales

linear [21] with its number of monomers  $N$  and the speed  $v$ :<sup>1</sup>

$$F_{fric} = N\zeta v. \quad (3.2)$$

When an adsorbed polymer is dragged across a surface, it follows the AFM tip depending on the friction coefficient and the velocity. Thereby, the polymer maximizes at the same time the adhesion enthalpy. In an equilibrium state, a constant polymer angle  $\Phi$  is adjusted, if the tangential component of the desorption force equals the total friction force  $F_R$  of the adsorbed polymer. Higher friction forces and thus larger polymer angles are expected, when the length of the adsorbed segment, the friction coefficient, or the pulling velocity in x-direction of the polymer increases [32]. Being able to measure the polymer angle  $\Phi$ , the friction force or coefficient of the adsorbed polymer could thus be determined (Figure 3.1).

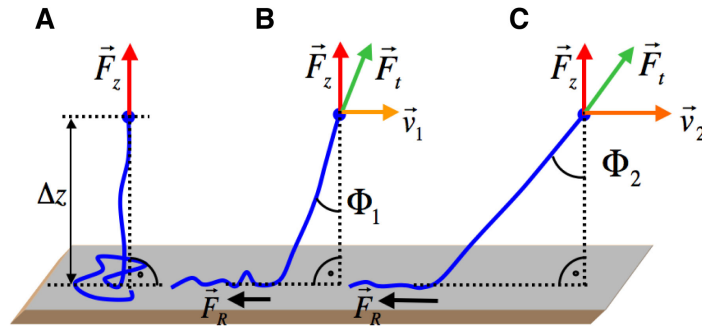


**Figure 3.1** The geometric scheme of a polymer movement in the x-direction under an applied force. **(A)** The polymer is partly desorbed from the surface. The measured force  $F_Z$  is equivalent to the desorption force. **(B)** and **(C)** The polymer is pulled lateral to the surface with different velocities. The polymer angle  $\Phi$  stays constant if the tangential force of the desorption equals the total friction force  $F_R$  of the adsorbed polymer. The friction  $F_R$  and the desorption force are acting along the contour of the polymer.

As a proof of principle, DNA could be pulled laterally on a mica surface over distances longer than its contour length. Consequently, it was qualitatively shown that DNA is highly mobile on mica under the chosen experimental conditions and follows the lateral motion of the cantilever (compare corresponding publication). As discussed in the previous chapter, the used cantilevers exhibit a high lateral stiffness in the north-south direction. Tangential forces are in principle detectable but only with an insufficient resolution because of the high spring constant for torsion stress [3]. The east-west direction is also not favorable because of its asymmetric force detection. Measuring unknown friction forces by moving the cantilever in this direction parallel to the surface may be difficult to interpret (Figure 2.3). Hence, there is unfortunately no direct way to measure the polymer angle  $\Phi$ , when the polymer is pulled across the surface.

<sup>1</sup>In contrast, macroscopic friction is independent on the contact area and the pulling speed but proportional to the normal force [31].

### New AFM measurement protocol

For this reason, a new approach was chosen to determine indirectly the polymer angle  $\Phi$ : the cantilever was retracted from the surface at a pulling angle  $\Omega$  with respect to the z-direction (Figure 3.2). Here, a lateral displacement  $\Delta x = \Delta z \cdot \tan(\Omega)$  might cause a sliding of the polymer across the surface. In contrast, the polymer desorbs continuously, if the friction force of the remaining adsorbed polymer section is high enough to prevent lateral sliding. Thereby, the measured rupture length in z-direction should decrease depending on the pulling angle with a factor of  $\cos(\Omega)$  (for better illustration, see Figure 3.3). Polymer desorption is only process occurring, if the pulling angle  $\Omega$  is smaller than the equilibrium polymer angle  $\Phi$ . In cases  $\Omega \geq \Phi$ , sliding across the surface is possible as the tangential component of the desorption force equals or is larger than the friction force. The polymer can follow the cantilever movement and constant rupture lengths are expected.

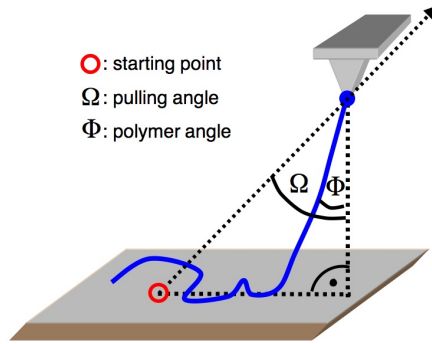


**Figure 3.2** Scheme of the experimental procedure. The cantilever is retracted at an angle  $\Omega$  from its starting point. Dependent on the rearrangement possibilities of the polymer, the polymer can follow the AFM tip and maximize its binding energy to the surface. However, the polymer angle  $\Phi$  stays constant if the friction of the adsorbed part equals the tangential desorption force.

As the cantilever is also continuously moved into the z-direction, the sliding polymer will detach as soon as it cannot bridge the gap between tip and surface any longer. Just prior to the final detachment, only a minimum segment  $l_{min}$ , which is required for adsorption, slides over the surface. The adhesion enthalpy of this minimum segment is necessary so that the polymer stays adsorbed against thermal fluctuation. The length of this segment was estimated in analogy to the Bell-Evans model [33]. The detachment obeys thus a two-state model, where  $l_{min}$  is either bound or unbound:

$$l_{min} \approx -\frac{k_B T}{F_c} \cdot \ln \left( \frac{F_c}{k_B T} \cdot \frac{v}{\nu_{off}} \right) + \kappa^{-1}. \quad (3.3)$$

The first term of the equation describes thermal activation and gives the minimum length of a polymer to stay adsorbed to the surface during the experiment. Here,  $F_c$  is the desorption force,  $v$  the retract velocity and  $\nu_{off}$  the attempt frequency. The Debye screening length  $\kappa^{-1}$  takes care of the screened Coulomb interaction, which has to be overcome when the polymer is detached from the surface by an external force. Inserting

experimental values ( $\kappa^{-1} = 2.14$  nm for 5 mM MgSO<sub>4</sub> [34],  $F_c = 50$  pN,  $\nu_{off} \approx 10^{12}$  s<sup>-1</sup> and  $v = 1$  μm/s) yields an estimated adsorbed minimum length  $l_{min} \approx 5.5$  nm.

As the tangential component of the desorption force equals the friction force at the moment of the detachment event, the friction coefficient  $\zeta$  per monomer can be correlated with the polymer angle  $\Phi$ :

$$\zeta = \frac{\tan(\Phi) \cdot F_z}{N_{min} \cdot v_x}. \quad (3.4)$$

$F_z$  is the desorption force in the vertical direction ( $\Omega = 0$ ),  $v_x$  the velocity of the polymer in the x-direction and  $N_{min}$  is the number of segments of  $l_{min}$ . Consequently, the friction coefficient  $\zeta$  can be determined by measuring the equilibrium polymer angle  $\Phi$  as discussed in the next section.

## 3.2 Measuring the friction of single polymers by AFM

The following force spectroscopy experiments were performed by retracting the cantilever with different pulling angles  $\Omega$  in the north-south direction (Figure 2.3). Thus, normal force detection with additional and unwanted horizontal force components resulting from the asymmetric shape of the cantilever was prevented. Moreover, the pulling angle was changed periodically by 10° or 15° after each force extension curve to avoid artefacts during the experiment. Three different friction regimes could be distinguished: infinite, low and mediate friction. A friction coefficient for a single sliding polymer could be measured for the latter regime.

A detailed discussion of the rupture forces for the investigated systems can be found in the attached publication. The measured rupture length distributions are of central interest in the mobility experiments and will be discussed in detail.

### Infinite friction: DNA on gold

A 4.9 kbp long ssDNA polymer was attached to AFM tip and was adsorbed on a gold substrate as shown in Figure 3.3. As can be seen here, the rupture length of the DNA molecule decreases with a factor of  $\cos(\Omega)$ . This correlates very well with the prediction that the polymer is only desorbed segment by segment and cannot follow the lateral movement of the cantilever due to high friction on the surface. The DNA molecule stays thus fixed on the surface similar to an anchor point. The geometric pulling scheme in Figure 3.3 explains the decrease of the rupture length  $R_z$  by the factor of  $\cos(\Omega)$ . In the light of the findings discussed in chapter 5, the high friction coefficient could be also explained by a coordinate bonding mechanism between primary amino groups of the DNA bases and undercoordinated gold adatoms. However, experimental differences (e.g. salt concentration, pH value and electrochemical gold reduction) between both experiments do not allow a direct comparison. Further studies combining these fields ("electro-friction") could elucidate the effect of high friction when desorbing ssDNA from a gold surface. Nevertheless, the angular retraction of the AFM tip showed qualitatively the infinite friction of ssDNA adsorbed on gold.

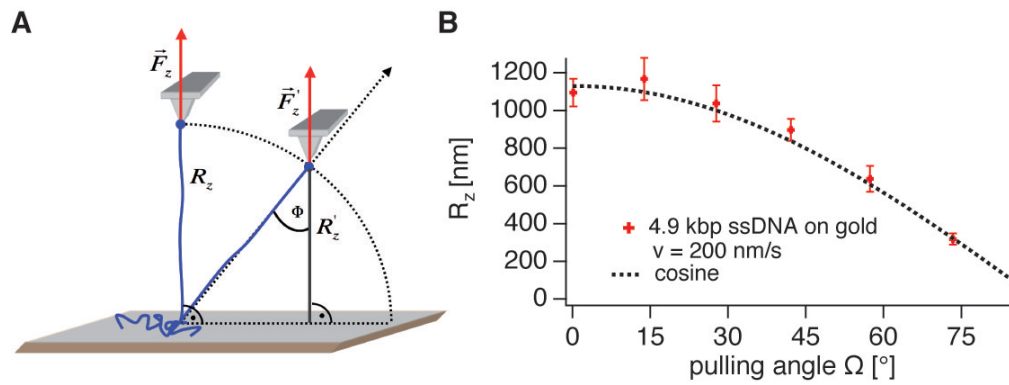


**Figure 3.3 (A)** A ssDNA polymer, which is covalently bound to the cantilever tip, is adsorbed on a gold surface and is desorbed from the surface at various angles. Because of a high friction coefficient, the adsorbed part of the ssDNA stays fixed on the surface. **(B)** Therefore, the rupture lengths  $R_z$  in the z direction decrease with increasing pulling angles  $\Omega$ .

### Low friction: DNA on mica

In the next experiment, 1.4 kbp long ssDNA polymer was adsorbed on a mica substrate as shown in Figure 3.4. The z-component  $R_z$  of the rupture length of the DNA molecule stays constant, which can only be explained with a high in-plane mobility of the adsorbed polymer at the surface. The polymer slides toward the desorption point by following the cantilever movement. Thus, ssDNA can adsorb to different surfaces with nearly the same binding energy but shows very different mobilities on the surface. The resulting polymer angle is smaller than the experimental resolution limit, which is approximately  $5^\circ$ . According to Equation 3.4, this threshold sets a limit for the minimum friction coefficient of  $\zeta \sim 3 \times 10^{-7}$  Ns/m. According to this procedure, the

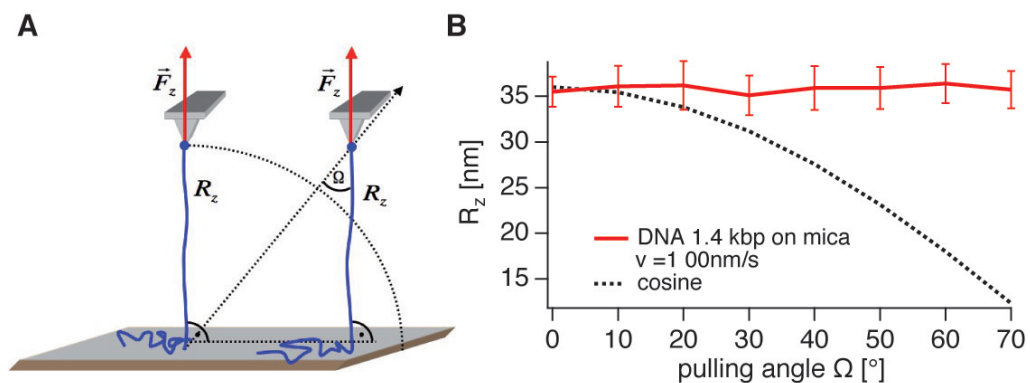


**Figure 3.4 (A)** A ssDNA polymer, which is covalently bound to the cantilever tip, is adsorbed on a mica surface and is desorbed at various angles from the surface. Because of the low friction coefficient, the ssDNA slides over the surface. **(B)** The rupture lengths  $R_z$  do not decrease with increasing pulling angles  $\Omega$ .

high mobility of ssDNA on mica could also be proven only qualitatively. Advantages of this method are thus expected for systems with higher friction coefficients, when the established methods fail because of very high observation periods or drift or bleaching reasons.

### Mediate friction: Polyallylamine on mica

Finally, we investigated the mobility of polyallylamine (PAAm) polymers on a mica surface in an equivalent experiment. Polyallylamine positively charged by its amino groups is expected to interact strong with the negatively charged mica surface. The corresponding rupture length distribution is depicted in Figure 3.5. First, the normalized z-components  $R_Z$  of two different polymer lengths decrease with the factor of  $\cos(\Omega)$  just as for infinite friction. But above an angle of about  $27^\circ$ , the measured rupture lengths  $R_Z$  deviate markedly from the infinite friction behavior and stay nearly constant for low velocities (see red curve in Figure 3.5 B). This can only be explained by sliding of the polymer during desorption. As this deviation from the infinite case occurs at the same angle and is independent of the polymer length, the friction force, and therefore the length of the segment, which slides over the surface is just given by the minimum adsorption length. As a consequence, the polymer angle  $\Phi$  does not further increase for pulling angles  $\Omega > 27^\circ$  but stays constant at  $\Phi = 27^\circ$ . The slight decrease of  $R_Z$  for higher pulling angles  $\Omega$  and higher speeds (compare blue curve in Figure 3.5 B) may be caused by the increase of the velocity in x-direction by the factor of  $\sin(\Omega)$  as the experiment were conducted with a constant total velocity  $|\vec{v}|$ . Experiments with constant horizontal velocity  $|\vec{v}_x|$  were not accomplished due to hydrodynamic effects. From the measured polymer angle  $\Phi = 27^\circ$ , the friction coefficient for PAAm on mica can be estimated with Equation 3.4 and with an estimated adsorbed minimum length  $l_{min} \approx 5.5$  nm resulting in  $\zeta = 1.4 \times 10^{-5}$  Ns/m.

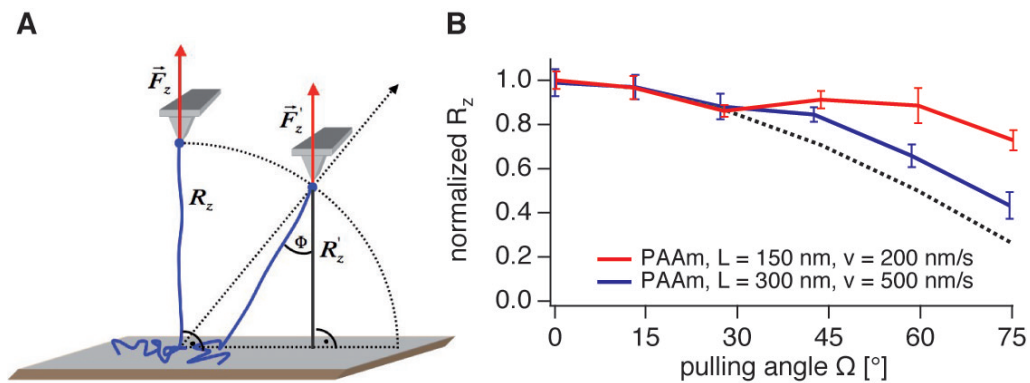


**Figure 3.5 (A)** A polyallylamine polymer is covalently bound to the cantilever tip. **(B)** First, the rupture lengths  $R_Z$  decrease analogue to the case of infinite friction. At pulling angles  $\Omega$  higher than  $27^\circ$ , the rupture length  $R_Z$  stays nearly constant for low velocities. The small additional decrease of  $R_Z$  is due to higher lateral velocities for higher pulling angles. The polymer angle is also  $27^\circ$  and results in a friction coefficient of  $\zeta = 1.4 \times 10^{-5}$  Ns/m.

In conclusion, the retraction of the AFM tip at various angles provides a new method to qualitatively determine the friction of single polymers adsorbed on surfaces. In particular, the range of  $3 \times 10^{-7} < \zeta < 2 \times 10^{-4}$  Ns/m can be resolved quantitatively by AFM. These limits are estimated values with respect to the resolvable precision for polymer angle and rupture length or drift artefacts. Within this friction range, conventional imaging experiments driven by thermal diffusion break down because of long observation periods and the associated drift or bleaching. To observe for example the movement of a PAAm polymer on the order of its own end-to-end distance would take approximately 2.6 h (estimation with the Rouse-time [17]). Further friction studies could include alternative surface geometries such as gratings, which would allow to measure friction forces in a direct way.



## Friction of Single Polymers at Surfaces

Ferdinand Kühner,<sup>\*,†</sup> Matthias Erdmann,<sup>†</sup> Lars Sonnenberg,<sup>†</sup> Andreas Serr,<sup>‡</sup>  
Julia Morfill,<sup>†</sup> and Hermann E. Gaub<sup>†</sup>

Chair for Applied Physics and Center for NanoScience, Ludwig Maximilians Universität,  
Munich, Germany, and Physics Department, Technische Universität, Munich – 85748 Garching, Germany

Received June 13, 2006. In Final Form: September 5, 2006

Atomic force microscope (AFM) single molecule force spectroscopy has been used to investigate the friction coefficient of individual polymers adsorbed onto a solid support. The polymer chains were covalently attached to an AFM tip and were allowed to adsorb on a mica surface. Different polymers (ssDNA, polyallylamine) were chosen to cover a range of friction coefficients. During the experiment, the AFM tip was retracted in- and off-plane which results, depending on the chosen conditions, in a desorption of the polymer from the surface, a sliding across the surface, or a combination of both. Thus, the obtained force-extension spectra reveal detailed information on the mobility of a polymer chain on a surface under experimentally accessible conditions. This study demonstrates that adsorbed polymers with comparable desorption forces may exhibit drastically different in plane mobility.

### Introduction

Polymers interacting with solid substrates are of general importance for many applications covering materials science, medicine, or biology. In particular, the adhesion strength of polymer chains to a certain substrate, the conformation of the molecule at the surface, and the lateral mobility or the diffusion constant of the polymer chain are essential parameters of interest.<sup>1–3</sup> On the molecular scale, these properties are determined by local interactions between polymer molecules and solid substrates at a solid–liquid interface.

Atomic force microscope (AFM) imaging was used in many instances to study the conformation of polymers adsorbed on a solid support.<sup>4–7</sup> These investigations were based on well-established theories for two-dimensional polymers, comprising excluded volume interactions.<sup>8</sup> It was shown that the properties of adsorbed DNA on surfaces depend on its diffusion constant. This was achieved by changing the friction coefficient due to chemical surface manipulations.<sup>9</sup> In general, the diffusion constant and thus the friction coefficient of a polymer molecule on a surface can be determined by monitoring the mean-square displacement of the molecule versus time. This can be realized, for example, using fluorescence microscopy<sup>10</sup> or scanning force microscopy.<sup>11,12</sup> The friction coefficient influences the conformation and the lateral mobility of a surface-adsorbed macromolecule strongly.

To study these macromolecular interactions in greater detail, AFM-based force spectroscopy has been proven to be one of the most sensitive methods. It allows the measurement of inter- and intramolecular forces with high precision.<sup>13–19</sup> These interactions reveal information about, for example, polymer conformation or molecular bond strengths.<sup>20–22</sup> Furthermore, AFM-based force spectroscopy has been applied successfully to measure the adhesion force of a single polymer adhered to a surface.<sup>23–25</sup> Further investigations yield information about the loop-size distribution of surface-adsorbed polymer chains<sup>26</sup> and the molecular weight distribution of surface-grafted chains<sup>27</sup> as well as the dependence of the adhesion force on the Debye screening length,<sup>28</sup> the non-Coulomb contributions,<sup>29</sup> and the solvent quality.<sup>30</sup>

In a typical AFM force spectroscopy experiment as conducted in this study, a single polymer is attached covalently to a cantilever tip. When approaching the solid substrate, the polymer is allowed

\* Author to whom correspondence should be addressed. E-mail: Ferdinand.Kuehner@lmu.de.

<sup>†</sup> LMU.

<sup>‡</sup> TU.

- (1) Gennes, P. G. d. Cornell University Press: Ithaca, NY, 1979.
- (2) Alexandre, M.; Dubois, P. *Mater. Sci. Eng., R* **2000**, *28*, (1–2), 1–63.
- (3) Yoshizawa, H.; Israelachvili, J. *J. Phys. Chem.* **1993**, *97*, (43), 11300–11313.
- (4) Hansma, H. G.; Kasuya, K.; Oroudjev, E. *Curr. Opin. Struct. Biol.* **2004**, *14*, (3), 380–385.
- (5) Kühner, F.; Erdmann, M.; Gaub, H. E. *Phys. Rev. Lett.* **2006**, accepted.
- (6) Clausen-Schaumann, H.; Gaub, H. E. *Langmuir* **1999**, *15*, (23), 8246–8251.
- (7) Jiao, Y.; Schaffer, T. E. *Langmuir* **2004**, *20*, (23), 10038–10045.
- (8) Milchev, A.; Binder, K. *Macromolecules* **1996**, *29*, (1), 343–354.
- (9) Pietrement, O.; Pastre, D.; Fusil, S.; Jeusset, J.; David, M. O.; Landousy, F.; Hamon, L.; Zozime, A.; Le Cam, E. *Langmuir* **2003**, *19*, (7), 2536–2539.
- (10) Maier, B.; Radler, J. O. *Phys. Rev. Lett.* **1999**, *82*, (9), 1911–1914.
- (11) Hansma, H. G.; Bezanilla, M.; Zenhausern, F.; Adrian, M.; Sinsheimer, R. L. *Nucleic Acids Res.* **1993**, *21*, (3), 505–512.
- (12) Pastre, D.; Pietrement, O.; Zozime, A.; Le Cam, E. *Biopolymers* **2005**, *77*, (1), 53–62.

- (13) Florin, E. L.; Moy, V. T.; Gaub, H. E. *Science* **1994**, *264*, (5157), 415–417.
- (14) Rief, M.; Gautel, M.; Oesterhelt, F.; Fernandez, J. M.; Gaub, H. E. *Science* **1997**, *276*, (5315), 1109–1112.
- (15) Clausen-Schaumann, H.; Rief, M.; Tolksdorf, C.; Gaub, H. E. *Biophys. J.* **2000**, *78*, (4), 1997–2007.
- (16) Janshoff, A.; Neitzert, M.; Oberdorfer, Y.; Fuchs, H. *Angew. Chem., Int. Ed.* **2000**, *39*, (18), 3213–3237.
- (17) Kühner, F.; Costa, L. T.; Bisch, P. M.; Thalhammer, S.; Heckl, W. M.; Gaub, H. E. *Biophys. J.* **2004**, *87*, (4), 2683–2690.
- (18) Hinterdorfer, P.; Baumgartner, W.; Gruber, H. J.; Schilcher, K.; Schindler, H. *Proc. Natl. Acad. Sci. U.S.A.* **1996**, *93*, (8), 3477–3481.
- (19) Unal, K.; Frommer, J.; Wickramasinghe, H. K. *Appl. Phys. Lett.* **2006**, *88*, 183105.
- (20) Grandbois, M.; Beyer, M.; Rief, M.; Clausen-Schaumann, H.; Gaub, H. E. *Science* **1999**, *283*, (5408), 1727–1730.
- (21) Rief, M.; Oesterhelt, F.; Heymann, B.; Gaub, H. E. *Science* **1997**, *275*, (5304), 1295–1297.
- (22) Minko, S.; Roiter, Y. *Curr. Opin. Colloid Interface Sci.* **2005**, *10*, (1–2), 9–15.
- (23) Hugel, T.; Grosholz, M.; Clausen-Schaumann, H.; Pfau, A.; Gaub, H.; Seitz, M. *Macromolecules* **2001**, *34*, (4), 1039–1047.
- (24) Chatellier, X.; Senden, T. J.; Joanny, J. F.; di Meglio, J. M. *Europhys. Lett.* **1998**, *41*, (3), 303–308.
- (25) Conti, M.; Bustanji, Y.; Falini, G.; Ferruti, P.; Stefoni, S.; Samori, B. *ChemPhysChem* **2001**, *2*, (10), 610–613.
- (26) Senden, T. J.; di Meglio, J.-M.; Auroy, P. *Eur. Phys. J. B* **1998**, *3*, (2), 211–216.
- (27) Sonnenberg, L.; Parvole, J.; Borisov, O.; Billon, L.; Gaub, H. E.; Seitz, M. *Macromolecules* **2006**, *39*, (1), 281–288.
- (28) Hugel, T.; Grosholz, M.; Clausen-Schaumann, H.; Pfau, A.; Gaub, H. E.; Seitz, M. *Macromolecules* **2001**, *34*, (4), 1039–1047.
- (29) Friedsam, C.; Gaub, H. E.; Netz, R. R. *Europhys. Lett.* **2005**, *72*, (5), 844–850.
- (30) Friedsam, C.; Seitz, M.; Gaub, H. E. *J. Phys.: Condens. Matter* **2004**, *16*, S2369–S2382.

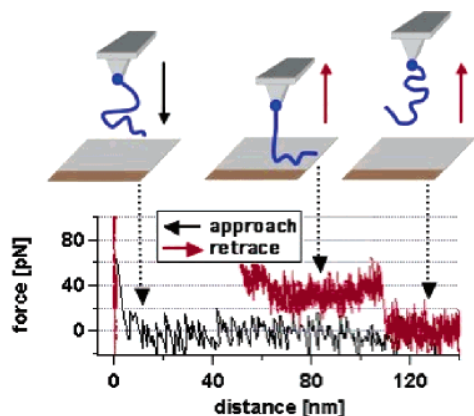


**Figure 1.** Example of a typical force extension curve of a polyallylamine polymer on mica. By approaching the cantilever to the surface, the polymer, which is covalently bound at one end to the tip, adsorbs on the surface. While retracting the cantilever, the polymer desorbs from the surface until it dissociates completely. Only the flat part of the force curve is analyzed. The force peak in the retrace curve close to the surface stems from a nonspecific interaction between the cantilever and the surface.

to adsorb onto the surface. While retracting the AFM tip, the polymer successively desorbs (de-adsorbs) from the surface (see Figure 1). This process occurs close to equilibrium conditions and therefore manifests itself as a plateau of constant force in the measured force-extension curve, which is called the desorption force  $F_c$  in the following. The force drops to zero as soon as the polymer is desorbed entirely. A recently published model for the nonequilibrium regime predicts that the desorption force varies if the angle at which the polymer is detached from the surface changes during the experiment.<sup>31</sup> However, if the polymer is able to rearrange itself on the surface on the time scale of the retraction, i.e., if the surface friction coefficient is small, it can maximize its binding energy. Therefore, the polymer will minimize its desorbed part, keeping the desorption angle relative to the surface as perpendicular as possible.

To prove that the surface mobility is high enough to allow such a rearrangement, we dragged an adsorbed ssDNA molecule over long distances across a mica surface (Figure 2). First, the length of the polymer was measured to be approximately 150 nm by desorbing it from the surface by a regular force extension curve. After the next approach, the same polymer was desorbed only partially. Then, the tip was moved parallel to the surface for several hundred nanometers.

The polymer was detached after the third step, when the tip was retracted vertical from the surface. Figure 2b shows the measured normal force when the cantilever was moved perpendicular to the surface, and Figure 2c shows when the cantilever was moved parallel to the surface. Obviously, the rupture length in the  $z$ -direction did not change significantly although the DNA was dragged across the surface up to a distance much larger than its contour length. This is only possible if the polymer is highly mobile and capable of following the lateral motion of the cantilever.

The major goal of this paper is to quantify this lateral mobility of the polymers and to measure the friction coefficient of a single polymer on a surface directly using a new approach on the basis of AFM. In contrast to the techniques described in the literature, which measure the mobility with thermally driven diffusion, we apply an external force to the molecule and detect its mobility and rearrangement response. This option to measure friction

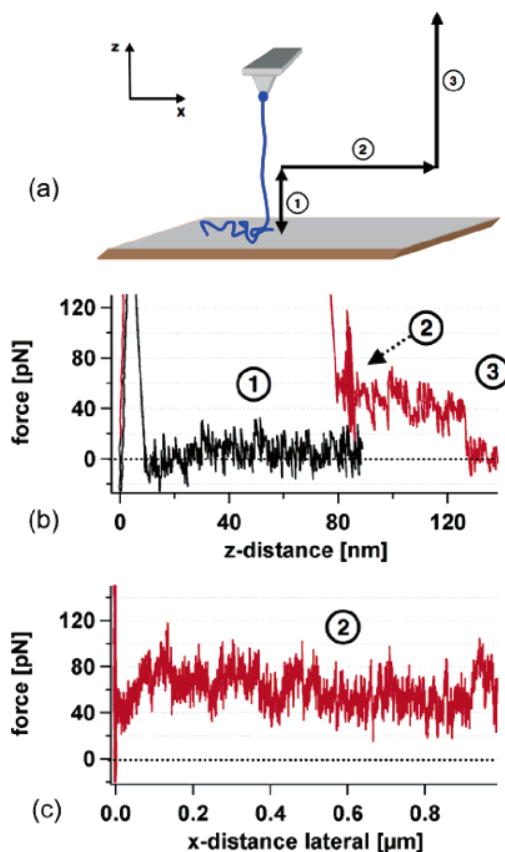


**Figure 2.** (a) An illustration of a modified protocol for measuring force curves. After retracting the cantilever to a certain distance away from the surface (1), the cantilever is moved parallel to the surface (2) and is finally retracted from the surface completely (3). (b) The measured force is plotted against the  $z$ -direction, which equals steps 1 and 3 in a. The lateral movement (2) is performed at a height of about 80 nm above the surface. The force against the  $x$ -direction is shown in c. The complete dissociation takes place at a height of about 125 nm, after pulling the DNA lateral on the surface over long distances without a considerable force increase.

locally and anisotropically will be of great importance when the sample surfaces are heterogeneous. The experimental boundaries of the new technique are explored (high friction and low friction limit).

## Materials and Methods

**AFM.** We used a commercial instrument (Molecular Force Probe 3D from Asylum Research, Santa Barbara, CA) and silicon nitride cantilevers (Veeco GmbH, Mannheim, Germany, MLCT-AUHW). The spring constants of each cantilever were calibrated individually by thermal calibration.

**Samples.** Polyallylamine solution (MD  $\sim$  65 000, 20 wt % in  $H_2O$ ) was purchased from Sigma-Aldrich, Germany.

DNA fragments of 1.4 kbp and 4.9 kbp ( $\sim$ 20 ng/ $\mu$ L concentration) were obtained from the vector pet28a by PCR, with an amino-modified primer sequence from IBA GmbH, Germany. The DNA was purified with the Qiagen PCR purification kit. Gel electrophoresis was used to confirm the homogeneity of the DNA length.

Experiments were performed in a phosphate buffer solution (10 mM, pH 7) containing 5 mM  $MgSO_4$  to ensure a positively charged mica surface.

For the DNA shear experiment, 30 nucleic acid long complementary single DNA strands were used, which are attached via a polyethyleneglycol (PEG) linker to the tip and the surface. The preparation of the DNA-shear measurement has already been published.<sup>32</sup> These measurements were performed in phosphate-buffered saline (PBS).

(31) Serr, A.; Netz, R. R. *Europhys. Lett.* **2006**, *73*, (2), 292–298.

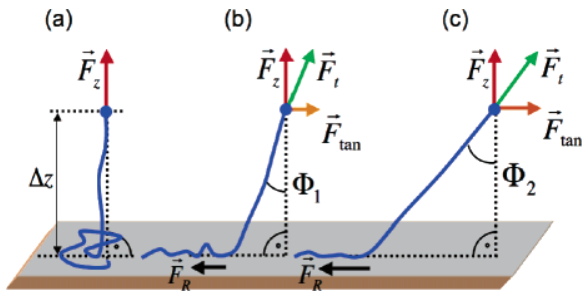


**Figure 3.** The geometric scheme of a polymer movement in the  $x$ -direction under an applied force. (a) The polymer is partly desorbed from the surface. The measured force  $F_z$  is equivalent to the desorption force. (b) and (c) The polymer is pulled lateral to the surface with different velocities. The polymer angle  $\Phi$  stays constant if the tangential force of the desorption equals the total friction force  $F_R$  of the adsorbed polymer. The friction  $F_R$  and the desorption force are acting along the contour of the polymer.

**Tip Functionalization.** The covalent attachment of polyallylamine and DNA to the AFM tip was accomplished by covalent carboxyl amino group binding. For this reason, the cantilevers were coated with a 30 Å chrome–nickel (80:20) layer followed by a 300 Å layer of gold by thermal evaporation. Afterward, the cantilevers were incubated immediately in a solution of a 16-mercaptohexadecanoic acid (15 mg) and 11-mercaptoundecanol (10 mg) in 100 mL ethanol (purissimum) for 12 h and then were rinsed with ethanol (puriss.) and Milli-Q water. Then, the carboxyl groups of the SAM<sup>33</sup> reacted with the amino end groups of the DNA in a solution of 10  $\mu$ L DNA and 20  $\mu$ L phosphate-buffered saline (PBS) containing 1-ethyl-3-(3-dimethylaminopropyl) carbodiimide (EDC) and *N*-hydroxysuccinimide (NHS) for 30 min. Fifteen micrograms of EDC and 3 mg of NHS were dissolved in 1 mL PBS for the latter stock solution. The attachment of polyallylamine to the AFM tip was realized by incubating the cantilevers in a solution of 10  $\mu$ L polyallylamine from a diluted stock solution (10  $\mu$ L polyallylamine 20 wt % in 1 mL Milli-Q water) and 20  $\mu$ L of the PBS stock solution containing EDC and NHS for 30 min. After the functionalization, the cantilevers were rinsed thoroughly with the MgSO<sub>4</sub> phosphate buffer and then were used immediately.

**Measurements and Analysis.** De-adhesion forces and rupture lengths were measured on freshly cleaved mica. The chain-functionalized AFM tips were brought into contact with the surface for several seconds and were retracted under different angles according to Figure 4. In one experiment, a thousand force curves were recorded with changing angles from curve to curve to avoid long-term drift effects. The absolute value of the cantilever speed was held constant for all angles because of hydrodynamic effects. For the calculation of the friction coefficient, the lateral component of the retrace speed was taken into account. After applying a low pass filter,<sup>34</sup> the mean average rupture force values and lengths were analyzed for each force curve with a self-written procedure in Igor 5.3. The rupture lengths were determined by a gauss fit of the rupture length histogram of every single angle. The error bars display a confidential interval of 95% of the maxima. The force values were obtained similarly.

### Theoretical Considerations

**Polymer Friction.** In the Rouse model, the diffusion constant  $D$  and the friction coefficient per segment  $\zeta$  are related through the Einstein relation:<sup>35</sup>

$$N \cdot \zeta = \frac{k_B T}{D} \quad (1)$$

where  $T$  is the absolute temperature,  $k_B$  is the Boltzmann constant, and  $N$  is the number of segments. The diffusion constant on surfaces was shown to be inversely proportional to the number

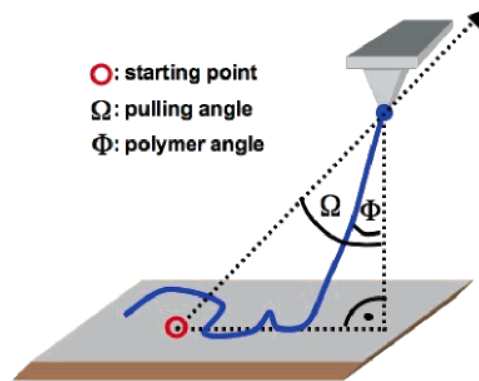


**Figure 4.** Scheme of the experimental procedure. The cantilever is retracted at an angle  $\Omega$  from its starting point. Depending on the rearrangement possibilities of the polymer, the polymer can follow the AFM tip and maximize its binding energy to the surface. However, the polymer angle  $\Phi$  stays constant if the friction of the adsorbed part equals the tangential desorption force.

of segments by Maier and Radler.<sup>10,36</sup> The measured diffusion constants vary between  $5 \times 10^{-15}$  m<sup>2</sup>/s for a 1.4 kbp<sup>12,37</sup> dsDNA polymer in 4 mM MgCl<sub>2</sub> solution and  $5 \times 10^{-12}$  m<sup>2</sup>/s for a 1.2 kbp<sup>38</sup> dsDNA polymer in 10 mM MgCl<sub>2</sub> solution on mica. The friction coefficients per base pair  $\zeta$  result in  $\sim 6 \times 10^{-10}$  Ns/m and  $\sim 6 \times 10^{-13}$  Ns/m, respectively. Such high diffusion constants can directly be measured with optical ensemble techniques such as fluorescence recovery after photobleaching (FRAP). In the case of low diffusion constants, long measurement times are required. This limits the minimum measurable diffusion constant because of drift, bleaching, or other side effects. In these cases, the analysis of image sequences is preferable albeit potential scanning artifacts.

To overcome these limitations, an external force is applied to the polymer in our study here. Inertia effects ( $< 10^{-13}$  s) are negligible for time scales longer than the thermal relaxation time ( $10^{-10}$  s).<sup>39</sup> So, if a constant force is applied to a small particle, the particle will immediately reach a constant velocity. Therefore, we assume (single molecules behave similarly to small particles; for polymer networks, other scaling laws are conceivable) that the total friction of an adsorbed polymer is given by eq 2 and scales linear with its number of monomers  $N$ ,<sup>36</sup> the friction coefficient  $\zeta$ , and the speed  $\nu$ .

$$F_R = N \cdot \zeta \cdot \nu \quad (2)$$

At a velocity  $\nu$  of 100 nm/s, the total friction force  $F_R$  acting on a 1.4 kbp DNA molecule on mica would be  $\sim 0.1$  pN only. This low friction is remarkable since the desorption force of ssDNA under these conditions reaches values of 50 pN, or in other units,  $\sim 6$   $k_B T$  per segment ( $\sim 0.5$  nm).

**Dragging a Polymer across a Surface.** Figure 3 sketches the experimental geometry for different contributions of the friction. Depending on the friction coefficient and the velocity, the adsorbed polymer follows the AFM tip whereas at the same time

(32) Kühner, F.; Morfill, J.; Neher, R. A.; Blank, K. R.; Gaub, H. E. *Biophys. J.* **2006**, submitted.

(33) Friedsam, C.; Del Campo Becares, A.; Jonas, U.; Gaub, H. E.; Seitz, M. *ChemPhysChem* **2004**, *5*, 388–393.

(34) Kühner, F.; Gaub, H. E. *Polymer* **2006**, *47*, (7), 2555–2563.

(35) Michael Rubinstein, R. H. C. *Polymer Physics*; Oxford University Press: 2003.

(36) Maier, B.; Radler, J. O. *Macromolecules* **2000**, *33*, (19), 7185–7194.

(37) Pastre, D.; Pietrement, O.; Fusil, P.; Landousy, F.; Jeusset, J.; David, M. O.; Hamon, C.; Le Cam, E.; Zozime, A. *Biophys. J.* **2003**, *85*, (4), 2507–2518.

(38) Rivetti, C.; Guthold, M.; Bustamante, C. *J. Mol. Biol.* **1996**, *264*, (5), 919–32.

(39) Hallatschek, O.; Frey, E.; Kroy, K. *Phys. Rev. Lett.* **2005**, *94*, (7), 077804.

it maximizes the adhesion energy. A constant angle  $\Phi$  results if the tangential component of the desorption force equals the total friction force  $F_R$  of the adsorbed polymer. In the following, this angle  $\Phi$  will be referred to as the polymer angle. In this model, we assume that a force applied to one end of the flexible polymer is propagating along its contour (Figure 3b and c).

Starting from one end, the friction force adds up from the last adsorbed segment to the desorption zone. The lateral applied force depends on the polymer angle. With increasing angle, the applied lateral force increases until it overcomes the total friction force of the adsorbed polymer. Higher friction forces and thus larger polymer angles are expected when the length of the adsorbed segment, the friction coefficient, or the pulling velocity in  $x$ -direction of the polymer increases.<sup>31</sup>

**Cantilever Actuation In- and Off-Plane.** Above, we have shown how the friction of a polymer on a surface is correlated to the polymer angle  $\Phi$ . In principle, tangential forces are detectable with an AFM cantilever<sup>40</sup> but only with insufficient resolution because of the enormous high spring constant for torsion stress. So, there is no direct way to measure the polymer angle  $\Phi$ .

However, in the following, we present a new approach for an indirect determination of  $\Phi$  where the cantilever is retracted from the surface at a pulling angle  $\Omega$  with respect to the  $z$ -direction (Figure 4). This way, a certain fraction of the friction couples into the deflection of the cantilever and becomes measurable, and the sliding of the polymer can be accessed.

In the case of a perpendicular force curve ( $\Omega = 0$ ), the  $z$ -component of the rupture length  $R_Z$  equals approximately the total length of the polymer (minus the length of the minimum adsorbed segment, see further below). When pulled at an oblique angle  $\Omega > 0$ , the lateral displacement  $\Delta x = \Delta z \cdot \tan(\Omega)$  of the tip might cause a sliding of the polymer chain across the surface. If the friction force of the adsorbed polymer segment is high enough to inhibit sliding over the surface, the polymer will continuously desorb from the surface and the  $z$  component of the rupture length will decrease. Desorption occurs as long as the pulling angle  $\Omega$  is smaller than the polymer angle  $\Phi$ . For pulling angles  $\Omega$  larger than the polymer angle  $\Phi$ , the polymer is able to follow the cantilever tip by sliding. Therefore, the  $z$ -component of the rupture length does not further decrease for larger pulling angles. Just prior to rupture, only the minimum polymer segment  $l_{\min}$ , which is required for adsorption, slides over the surface.

**Minimum Length of an Adsorbed Polymer  $l_{\min}$ .** To estimate the minimum polymer segment  $l_{\min}$ , we assume that the rupture event obeys a two-state model where  $l_{\min}$  is either bound or unbound. The moment when the polymer completely desorbs is defined as the dissociation process. In analogy to the Bell–Evans standard theory<sup>41,42</sup> of force-induced dissociation of a receptor–ligand system, the process is modeled as follows:

$$k_{\text{off}}(l) = \nu_{\text{off}} \cdot e^{-\frac{-(l \cdot F_c) - (\Delta x \cdot F_c)}{k_B T}} \quad \text{with } \Delta G = l \cdot F_c \quad (3)$$

$$P(l) = 1 - e^{-\int_{l_0}^l \frac{1}{\nu} k_{\text{off}}(L) dL} \quad \text{with } l = l_0 - \nu \cdot t \quad (4)$$

$$dP(l) = \frac{1}{\nu} \cdot k_{\text{off}}(l) \cdot e^{-\int_{l_0}^l k_{\text{off}}(L) dL} dl \quad (5)$$

where  $k_{\text{off}}$  is the thermal off rate,  $l$  is the adsorbed polymer length,

(40) Radmacher, M.; Tillmann, R. W.; Fritz, M.; Gaub, H. E. *Science* **1992**, *257*, (5078), 1900–1905.

(41) Evans, E.; Ritchie, K. *Biophys. J.* **1997**, *72*, (4), 1541–1555.

(42) Evans, E. *Annu. Rev. Biophys. Biomol. Struct.* **2001**, *30*, 105–128.

$\nu_{\text{off}}$  is the attempt frequency,  $\nu$  is the retrace speed of the cantilever,  $F_c$  is the desorption force, and  $\Delta x$  is the potential width of the interaction between the surface and the polymer.

$P(l)$  is the probability function for the bound or unbound state of the polymer respectively to the adsorbed length. The derivative of the probability density function  $d^2P(l)/dl^2 = 0$  defines the most likely segment length before dissociation which corresponds to  $l_{\min}$ . The potential width  $\Delta x$  of the electrostatic interaction should approximately equal the Debye length  $\kappa^{-1}$ , which depends on the buffer conditions. This results in a maximal likelihood for a minimum polymer segment  $l_{\min}$  before dissociation:

$$l_{\min} \approx -\frac{k_B T}{F_c} \cdot \ln\left(\frac{F_c}{k_B T} \cdot \frac{\nu}{\nu_{\text{off}}}\right) + \kappa^{-1} \quad (6)$$

The first term of the equation describes thermal activation and gives the minimum length of a polymer to stay adsorbed to the surface during the experiment. The second term  $\kappa^{-1}$  takes care of the screened Coulomb interaction, which has to be overcome when the polymer is detached from the surface by an external force and is transferred into the solution. Since at the given electrolyte conditions van der Waals forces are weaker and other forces such as H-bonds or ion bridges have a shorter interaction range, these interactions are subsumed in the dominating Coulomb interaction.

The Debye screening length for a 5 mMol MgSO<sub>4</sub> buffer solution is approximately 2.14 nm.<sup>43</sup> For a force  $F_c$  of 50 pN, an attempt frequency of  $10^{12} \text{ s}^{-1}$  and a velocity  $\nu$  of 1  $\mu\text{m/s}$  the length  $l_{\min}$  results in  $\sim 5.5 \text{ nm}$ .

**Correlation between the Polymer Angle and the Friction Coefficient.** In the case of friction, the  $z$ -component of the rupture length  $R_Z$  decreases for higher pulling angles  $\Omega$  with the factor of  $\cos(\Phi)$ . At the moment when the pulling angle exceeds the polymer angle, the polymer slides and as a result the rupture length  $R_Z$  stays constant as discussed above. At this polymer angle  $\Phi$ , the tangential force is high enough that the polymer can follow the lateral movement. At the moment of the rupture event, the friction force of  $l_{\min}$  equals the tangential component of the adhesion force. By eq 2, the polymer angle  $\Phi$  can be correlated with the friction coefficient  $\zeta$  per monomer

$$\zeta = \frac{\tan(\Phi) \cdot F_z}{N_{\min} \cdot \nu_x} \quad (7)$$

where  $F_z$  is the force for vertical desorption ( $\Omega = 0$ ),  $\Phi$  is the polymer angle,  $\nu_x$  is the velocity of the polymer in the  $x$ -direction, and  $N_{\min}$  is the number of segments of  $l_{\min}$ .

In the following, four different regimes are investigated in terms of the mobility of the polymer: infinite friction, high friction, low friction, and intermediate friction.

## Results and Discussion

**Infinite Friction: Covalent Attachment.** The first system can be regarded as a test for the experimental setup and the geometries discussed above.

Infinite friction is achieved by binding PEG chains (polymer) covalently to the AFM cantilever tip and to the surface, which then are functionalized additionally with conjugated DNA

(43) Israelachvili, J. *Intermolecular & Surface Forces*; Academic Press: San Diego, CA, 1992.

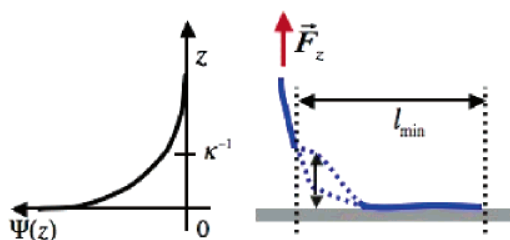


**Figure 5.** The minimum part  $l_{\min}$  is a composition of the two terms in eq 6. The polymer is attracted by an exponential potential  $\Psi(z)$  to the surface. An applied force enables the polymer to fluctuate at the desorption zone between the bound and unbound state in the Debye range, illustrated by the dashed line.

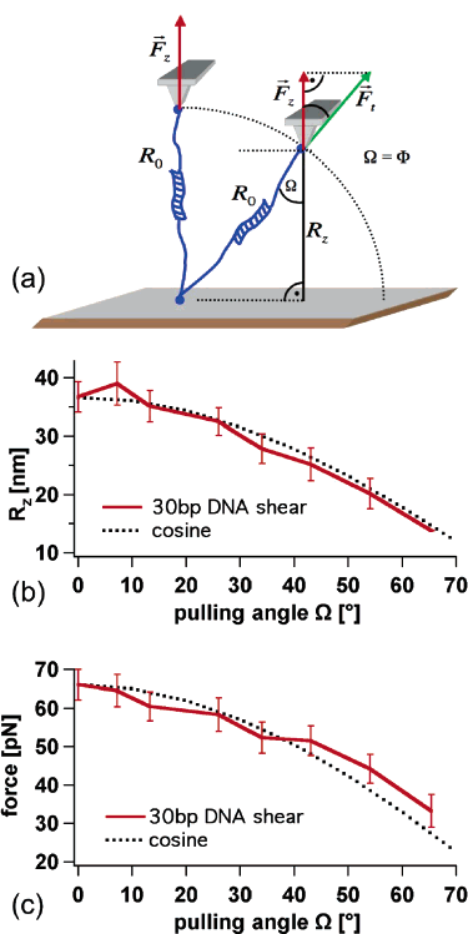


**Figure 6.** To simulate the case of infinite friction, two PEG polymers are covalently attached at their ends to the AFM cantilever tip and the surface. The free ends each are functionalized with a 30 base ssDNA oligo. If the cantilever tip approaches the surface, the two complementary DNA single strands can hybridize. By retracting the cantilever tip with an angle  $\Omega$ , the  $z$ -component  $R_z$  of the rupture length and the measured force  $F_z$  decrease with a factor  $\cos(\Phi)$ . In b, the maxima of the measured rupture length distributions  $R_z$  are plotted against the various pulling angles  $\Omega$ . In c, the maxima of the measured force distributions dependent on the pulling angles  $\Omega$  are shown. The measured force  $F_z$  is the cosinus component of the total force  $F_t$ , which acts along the contour of the polymer and drives the dissociation of the DNA.

oligomers (Figure 6a). Thus, no force arises from desorbing the PEG chain from the surface. However, the DNA duplex acts as a force sensor and limits the force applied to the polymer chain along its contour. If the force overcomes a certain threshold of 60–65 pN, the dsDNA duplex dissociates. In Figure 6b and c, the maxima of the rupture length  $R_z$  and the maxima of the

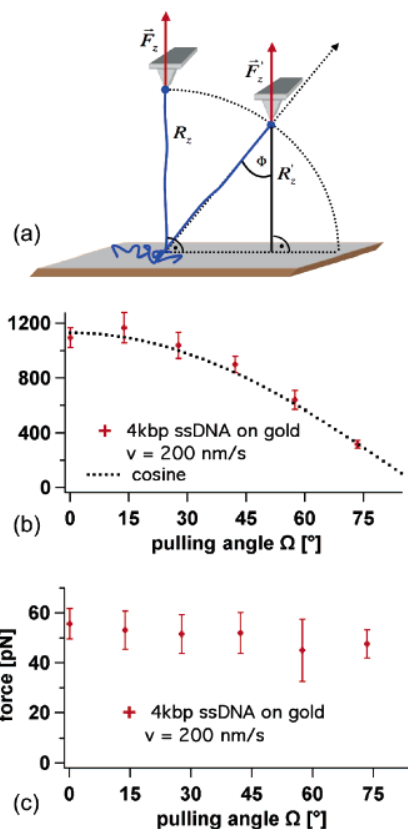


**Figure 7.** A ssDNA polymer, which is covalently bound to the cantilever tip, is adsorbed on a gold surface and is desorbed from the surface at various angles. Because of a high friction coefficient, the adsorbed part of the ssDNA stays fixed on the surface. Therefore, the rupture lengths  $R_z$  in the  $z$  direction (b) decrease with increasing pulling angles  $\Omega$ .

measured forces are plotted against the related pulling angles  $\Omega$ . As can be seen, the forces and the rupture lengths in the  $z$  direction are reduced by the factor  $\cos(\Phi)$  which correlates very well with the prediction on the basis of fixed covalent anchor points on the surface and on the cantilever tip. It also shows quite convincingly that the cantilever only detects the  $z$ -component of the force. Since the unbinding force of the DNA duplex is constant but acts via the contour of the polymer, the measured unbinding force detected by the cantilever decreases with increasing angles.

**Infinite Friction: DNA on Gold.** In the following experiment, a 1.4 kbp long ssDNA polymer was attached to the cantilever tip covalently and was adsorbed on a gold substrate as shown in Figure 7a. For a single DNA molecule, the relation between the  $z$ -component  $R_z$  of the rupture lengths and the rupture forces for different angles is shown in Figure 7b and c. As can be seen here, the  $z$ -component  $R_z$  of the rupture length of the DNA molecule decreases such as in the case of covalent binding. This means that the ssDNA cannot follow the lateral movement of the cantilever because of high friction on the surface. The friction coefficient of the ssDNA on gold is above our detection limit of  $\zeta \sim 2 \times 10^{-4}$  Ns/m.

The measured desorption force (see Figure 7c) of the ssDNA polymer, however, was found to be virtually independent from different pulling angles. This means that although the angle at which the polymer is pulled off the surface varies, the  $z$ -component of the desorption force remains constant. Since the out-of-plane friction is negligible compared to the in-plane friction at the surface, the work of de-adhesion performed by the cantilever in the  $z$ -direction equals the adhesion free enthalpy of the polymer.

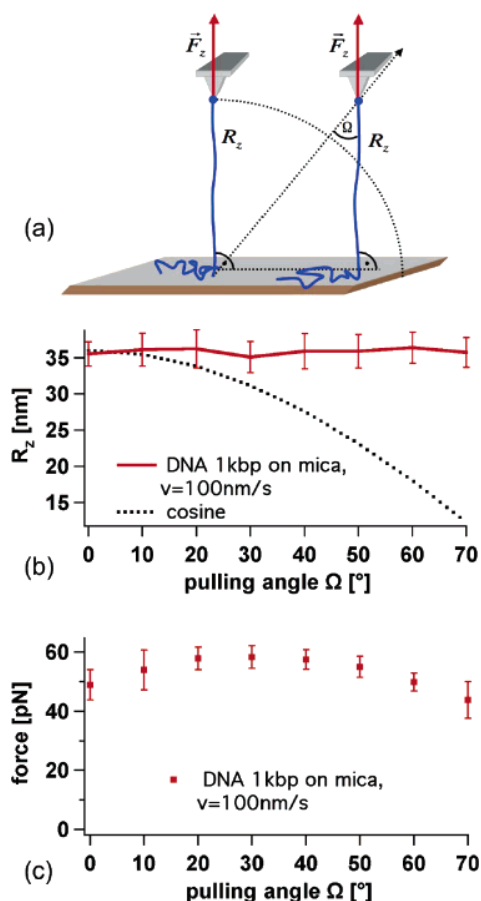


**Figure 8.** A ssDNA polymer, which is covalently bound to the cantilever tip, is adsorbed on a mica surface and is desorbed at various angles from the surface. Because of the low friction coefficient, the ssDNA slides over the surface. The rupture lengths  $R_z$  shown in b and the measured forces shown in c do not decrease with increasing pulling angles  $\Omega$ .

A constant  $z$ -component of the desorption force is the consequence. This finding explains as a side effect, why in many previous studies<sup>24,44</sup> the measured desorption plateaus are flat despite the unknown 2d configuration of the adsorbed polymer at the surface.

These two experiments demonstrate clearly the geometrical relationship between the applied, the measured, and the dissociation forces which act on the system very nicely.

#### Low Friction: DNA on Mica.

In the next experiment, the same 1.4 kbp long ssDNA polymer was adsorbed on a mica substrate as shown in Figure 8a. As can be seen here in Figure 8b, the  $z$ -component  $R_z$  of the rupture length of the DNA molecule stays constant, which can only be explained with a high in-plane mobility of the adsorbed polymer at the surface. The polymer slides toward the desorption point and the resulting polymer angle is smaller than the experimental resolution limit. The diffusion constant for ssDNA seems to be close to the diffusion constant of dsDNA. Because of drift and the rupture length distribution, the resolution limit given by eq 7 is approximately 5°. This threshold sets a limit for the minimum friction coefficient of  $\zeta \sim 3 \times 10^{-7}$  Ns/m.

Advantages of this method are expected rather for systems with higher friction, when the established methods fail because of very high observation periods or drift or bleaching reasons.

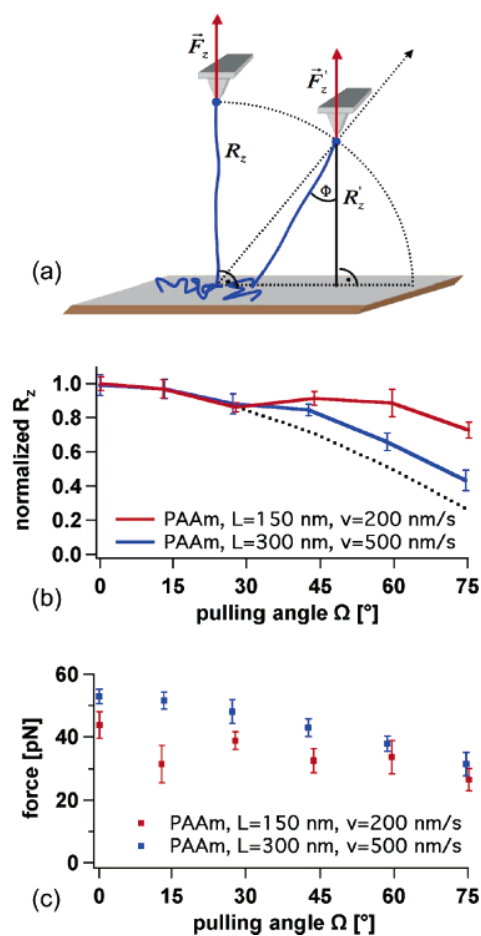


**Figure 9.** A polyallylamine polymer is covalently bound to the cantilever tip. (b) The rupture lengths  $R_z$  dependent on the pulling angles  $\Omega$ . The rupture lengths  $R_z$  decrease analogues to the case of infinite friction. At pulling angles  $\Omega$  higher than 27°, the rupture length  $R_z$  stays nearly constant for low velocities. The small additional decrease of  $R_z$  is due to higher lateral velocities for higher pulling angles. The polymer angle is also 27° and results in a friction coefficient of  $\zeta = 1.4 \times 10^{-5}$  Ns/m. (c) The measured forces are plotted against the pulling angle  $\Omega$ .

ssDNA can adsorb to different surfaces with nearly the same binding energy but shows very different motilities on the surface.

**Intermediate Friction: Polyallylamine on Mica.** As an example for an intermediate friction, polyallylamine (PAAm) on mica was investigated in an equivalent experiment just as the one above. The positively charged amine groups of the PAAm polymer are expected to interact directly and therefore stronger with the negatively charged mica surface, and no bivalent metal ions are required for adsorption as for ssDNA.

Figure 9 shows the schematics of the experimental setup, the measured  $z$ -components  $R_z$  of the rupture length, and the rupture force as a function of the pulling angle  $\Omega$  for several PAAm polymers with different lengths. Independent of the polymer length, the  $z$ -components  $R_z$  of the rupture lengths first decrease by a factor of  $\cos(\Omega)$  just as for infinite friction. Above an angle of about 27°, the measured  $z$ -components of the rupture lengths  $R_z$  deviate markedly from the infinite friction behavior and stay nearly constant for low velocities (see red curve in Figure 9b). This can only be explained by sliding of the polymer during desorption.  $R_z$  decreases because of higher lateral velocities for higher pulling angles and is more distinct at higher velocities (see blue curve in Figure 9b). The fact that the deviation of  $R_z$  from the infinite case occurs at the same angle and is independent

(44) Seitz, M.; Friedsam, C.; Jostl, W.; Hugel, T.; Gaub, H. E. *ChemPhysChem* 2003, 4, (9), 986–990.

of the polymer length means that the friction force, and therefore the length of the segment, which slides over the surface is just given by the minimum adsorption length. This again means that for pulling angles  $\Omega > 27^\circ$  the polymer angle does not further increase but stays constant at  $\Phi = 27^\circ$ . The lateral component of the force equals the friction force of the adsorbed polymer and enables the polymer to slide on the surface. From this angle, the friction coefficient can be estimated with eq 7 for an  $l_{\min}$  of 5.5 nm and results in  $\Omega = 1.4 \times 10^{-5}$  Ns/m (0.3 nm per segment). This value would convert (eq 1) into a diffusion constant of  $D \approx 6 \times 10^{-19}$  m<sup>2</sup>/s for a single 150-nm-long PAAm polymer. The slight decrease of the  $z$ -component of the rupture lengths  $R_z$  for higher pulling angles, which we find particularly for longer polymers, may be caused by the increase of the velocity in the  $x$ -direction by the factor of  $\sin(\Omega)$  (see Measurement and Analysis). This results in a higher friction force and therefore in a decreased rupture length, which can be seen in Figure 9b.

The measured rupture forces vary with speed but stay nearly constant for different angles (see Figure 9c). The slight decrease may follow from the fact that the polymer is in a stretched conformation on the surface. Compared to ssDNA on mica, which can equilibrate nearly instantaneously, the polyallylamine is out of equilibrium while pulling. This may lead to smaller desorption forces at higher angles.

As an example: the total lateral friction force for a 100-nm-long PAAm molecule at a speed of 100 nm/s would be approximately 145 pN.

### Concluding Remarks

In the present study, we have introduced a new approach to measure the friction coefficient of single polymers adsorbed on surfaces using AFM, which is particularly well suited for high friction coefficients, which are hard to quantify otherwise. We show that although a force of several tens of piconewtons is required to desorb DNA from a mica surface, the friction force for lateral movement on the surfaces is extremely low. We speculate that this might be due to the divalent positive charged ion layer of  $\text{Mg}^{2+}$  on the mica surface, which allows the ssDNA to basically float over the surface. Such mechanisms were

discussed widely in the literature,<sup>37,45</sup> and our results are in good agreement with these findings. A strong interaction between gold and the bases, which are exposed in ssDNA, was found by several groups. H-bonding and even weak coordinative bonds were discussed as molecular mechanisms.<sup>46</sup> The very high friction that we measured with this system corroborates these findings. Although the desorption force of polyallylamine on mica is comparable to the one we found with DNA, we learned that the friction is orders of magnitudes higher, which makes polyallylamine a preferable polymer for durable coatings of surfaces.<sup>47</sup> Whereas DNA is known to be fully hydrated and additionally restrained from the direct contact with the surface by the  $\text{Mg}^{2+}$  ions, we found no indications for comparable mechanisms for polyallylamine.

We found the Einstein relation to be a useful approximation for the description of the displacement of a single molecule under an external force. The friction force correlates with the speed at which the polymer is dragged over the surface. We also demonstrated that the polymer is able to rearrange and maximize its binding energy dependent on its friction coefficient, while it is desorbed from the surface by the cantilever tip. It is evident that alternative sample surface geometries with broken symmetries such as gratings or the like will allow in future experiments to access friction forces in a direct way, since not only the pulling angle with respect to the surface but also the cantilever angle and the detection geometry are tilted with respect to the surface. Additional insight may be gained from future dragging experiments in confined geometries.

**Acknowledgment.** We thank Erich Sackmann, Gregor Neuert, and Roland Netz for helpful discussions and the DFG for financial support. F. Kühner and A. Serr are supported by the Elitenetzwerk Bayern.

LA061704A

(45) Hansma, H. G.; Laney, D. E. *Biophys. J.* **1996**, *70*, (4), 1933–1939.

(46) Boland, T.; Ratner, B. D. *Majewski, J. Proc. Natl. Acad. Sci. U.S.A.* **1995**, *92*, (12), 5297–5301.

(47) Cebeci, F. C.; Wu, Z. Z.; Zhai, L.; Cohen, R. E.; Rubner, M. F. *Langmuir* **2006**, *22*, (6), 2856–2862.

# 4 Electrical controlled DNA adhesion

The previous chapters presented new force spectroscopy approaches to investigate conformational and dynamic characteristics of adsorbed polymers. Thereby, the physics of the adsorption process itself was not discussed in detail. The following chapter will focus on the adsorption of polymers and its external electrical manipulation. Therefore, AFM based single molecule experiments with dsDNA were conducted on chemically modified electrodes. As a result, the adsorption of dsDNA onto these electrodes was controlled electrically and absolute adhesion forces depending on the applied potential were measured for the first time.

## 4.1 Desorption force, applied potential and surface charge

### Calculation of the desorption force

The desorption of polymers at equilibrium conditions from solid substrates was studied comprehensively by AFM based experiments and theoretical models [35, 36, 37, 38, 39, 40]. Successively desorbing a polymer from a surface manifests itself in a plateau of constant force in the measured force extension curves, which is called the desorption force  $F_c$ . The **desorption force**  $F_c$  is described by a

$$F_c = F_0 + (4\pi l_B k_B T) \cdot \kappa^{-1} \cdot \tau \cdot \sigma \quad (4.1)$$

with  $l_B$  being the Bjerrum length (0.71 nm in water), the thermal energy  $k_B T$  (4.12 pNnm), the Debye screening length  $\kappa^{-1}$ ,  $\tau$  the line charge density in  $\text{nm}^{-1}$  of the polymer and the surface charge density  $\sigma$  in  $\text{nm}^{-2}$ . The non-coulombic term  $F_0$  contains forces ascribed to van-der-Waals forces, hydrogen bonding or hydrophobic effects etc. As can be seen from Equation 4.1, the desorption force is linearly dependent on the term  $\kappa^{-1} \cdot \tau \cdot \sigma$ . In the cited previous studies, the electrostatic contribution of the desorption force could be controlled by varying the line charge density  $\tau$  of the polymer, the salt concentration of the buffer solution ( $\kappa^{-1}$  depends on  $c_{salt}$ ) and the surface charge density  $\sigma$ , respectively. From these findings follows the motivation to control and manipulate the desorption force of single polymers from electrodes with external adjustable surface potential rather than by changing global parameters of the sample like the buffer solution or the polymer itself. A logical consequence was thus to combine AFM-based single molecule force spectroscopy with the potentiostatic control of the surface potential and adjust thereby the surface charge density.



### Relationship between applied potential and surface charge density

For the experiments, chemically modified gold electrodes were used: A self-assembled monolayer (SAM) of alkyl chains was covalently bound via S-Au bonds to the gold electrodes; the alkyl chains were terminated by a hydroxyl group (-OH) or a amino group (-NH<sub>2</sub>), respectively. These monolayers prevented a charge transfer (e.g. electrons) across the metal-solution interface and oxidation or reduction of species in the solution were consequently suppressed. Thus, electrostatic/coulombic interactions were predominantly responsible for the observed physiosorption of dsDNA to the SAM electrode (Figure 4.1).

In order to calculate the surface charge density  $\sigma$  on the SAM electrodes, which depends on the **applied potential**  $\phi$ , the potential drop between the gold electrode and the insulating SAM layer and as well as the diffuse counterion layer has to be considered. Depending on the surface charge, counterions in solution are attracted and screen the surface charge leading to an exponential decrease of the potential in the solution. In the Gouy-Chapman theory, the potential on the solution side is called **diffuse layer potential**  $\psi_D$ . The relation between the applied potential  $\phi$  and the resulting diffuse layer potential  $\psi_D$  for a SAM electrode is given by [41]:

$$\psi_D(\phi) = \frac{C_L}{C_L + C_D(\psi_D)} (\phi - \phi_{pzc}), \quad (4.2)$$

whereby  $C_L = 0.8 \mu\text{F}/\text{cm}^2$  and  $C_D(\psi_D)$  are the capacitances of the OH-SAM and the diffuse layer, respectively. The potential of zero charge  $\phi_{pzc}$  adjusts the diffuse layer potential with respect to the used reference electrode. Moreover, the Gouy-Chapman theory yields for the diffuse layer capacitance [42]:

$$C_D(\psi_D) = \left( \frac{2z^2 e^2 \epsilon \epsilon_0 n^0}{k_B T} \right)^{1/2} \cosh \left( \frac{ze\psi_D}{2k_B T} \right), \quad (4.3)$$

where  $z$  is the magnitude of charge on the ions,  $e$  is the electron charge,  $\epsilon \epsilon_0$  is the total permittivity of water and  $n^0$  is the number concentration of each ion in the bulk. Inserting this relationship into Equation 4.1 results in a transcendental expression for the diffuse layer potential  $\psi_D$ , which was solved numerically for different applied potentials  $\phi$ . To give experimental values, applying a voltage of  $\phi = +0.5 \text{ V}$  yields a diffuse layer potential of  $\psi_D = +0.07 \text{ V}$  for a self assembled monolayer of alkyl chains with 11 carbon atoms terminated by hydroxyl group (-OH). Consequently, the potential drop is in the range of 86 %.

The Grahame equation then delivers the **surface charge density**  $\sigma$  on the SAM, which is responsible for the diffuse potential above the electrode:

$$\sigma = -\sigma_D(\psi_D) = (8k_B T \epsilon \epsilon_0 n^0)^{1/2} \sinh \left( \frac{ze\psi_D}{2k_B T} \right). \quad (4.4)$$

Thus, the resulting desorption force  $F_c$  in case of an applied potential  $\phi$  can be calculated according to Equation 4.1. This theoretical description is used in the next section to model the coulombic adhesion between dsDNA and polarized SAM electrodes.

## 4.2 Electrical manipulation of the desorption force

### Experimental setup

AFM force spectroscopy measurements with 4.9 kbp dsDNA covalently bound to the AFM tip were conducted by desorbing this dsDNA from an OH-SAM-modified gold electrode under potentiostatic control (Figure 4.1). First, the dsDNA functionalized AFM tip was brought into contact with the OH-SAM electrode. The AFM tip was then retracted and the dsDNA was desorbed from the OH-SAM electrode. Only the last force step between dsDNA and the OH-SAM was analyzed to ensure the measurement of a single molecule detachment.

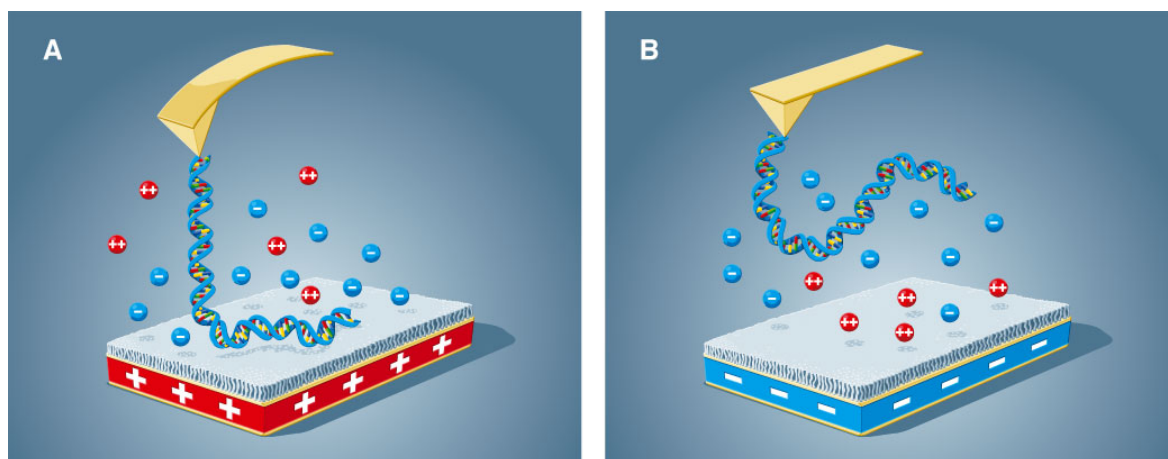


**Figure 4.1** Idealized representation of the single molecule desorption experiments on an OH-SAM electrode. 4.9kbp dsDNA was covalently bound to an AFM tip, and the functionalized tip approached a gold microelectrode covered by an OH-SAM. An aqueous magnesium chloride solution was used, and the surface potential was controlled by a potentiostat (not shown). **(A)** Positive surface potentials induced the adsorption of dsDNA on the OH-SAM resulting in adhesion forces of up to 25 pN (at +0.5 V vs. Ag/AgCl). **(B)** In case of applied negative surface potentials, no dsDNA adsorption on the OH-SAM was observed.

The measurement protocol was analogous to cyclic staircase voltammetry [43, 44]: the potential between the OH-SAM electrode (working electrode) and the Ag/AgCl reference electrode was linearly ramped between -0.4 V and 0.5 V. Simultaneously, the desorption force and the current were recorded. In order to minimize bimetal artefacts in the deflection signal, which are related to the ion current, the potential was changed by 10 mV steps after each force extension trace with the AFM tip being placed 3  $\mu\text{m}$  away from the electrode. When the AFM tip with the dsDNA then approached the surface again, the surface polarization was equilibrated according to the applied potential until the ion current ceased. Thus, the AFM tip bimetal artefacts in the deflection signal could be minimized, too. The solution contained also a low salt concentration of 100  $\mu\text{M}$   $\text{MgCl}_2$  to decrease bimetal artefacts as well and to increase the Debye screening length ( $\kappa^{-1} = 19$  nm for a 2:1 electrolyte, see discussion below).

### Desorption force depends on applied potential

The desorption force distribution of dsDNA on the OH-SAM vs. the curve number at pH 8.5 is shown in Figure 4.2 A. The resulting desorption force distribution shows well defined and almost symmetrical force peaks in the positive range around +0.5 V with a force maximum of about 25 pN, whereas no interaction between dsDNA and the OH-SAM was measured at negative potentials. This cycling process was reversible over a large number of force curves.

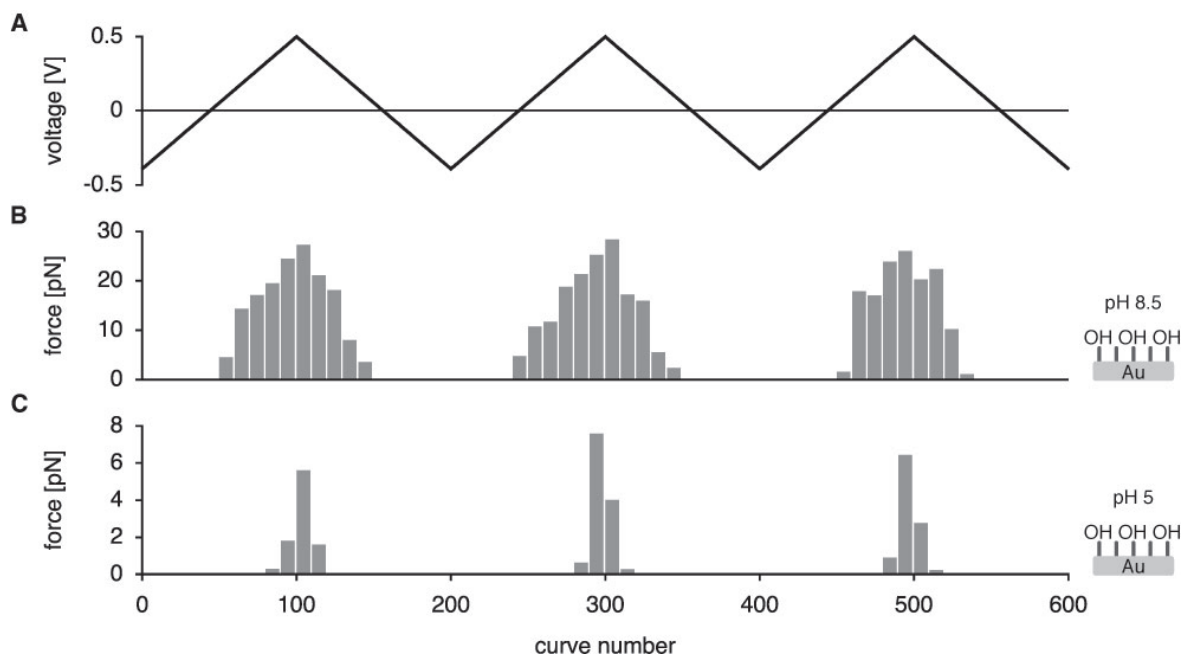


**Figure 4.2** Cyclic change of the surface potential of the OH-SAM electrode: rupture forces of dsDNA vs. curve number. **(A)** As in classic cyclic voltammetry, the potential between the SAM functionalized electrode (working electrode) and an Ag/AgCl reference electrode was linearly ramped between -0.4 V and 0.5 V and plotted versus the curve number. The potential was changed by 10 mV per curve number; the electrolyte contained 100 MgCl<sub>2</sub> at various pH-values. A platinum counter electrode completed the three-electrode setup. **(B)** At pH 8.5, the resulting rupture force distribution for the OH-SAM electrode showed well-defined and symmetrical force peaks in the positive range around +0.5 V with a force maximum of about 25 pN, whereas no interaction between dsDNA and the OH-SAM was measured at negative potentials. **(C)** The same experiment at pH 5 revealed rupture forces around 7 pN only at +0.5 V. Here, the phosphate group at the 5'-end of the dsDNA is expected to be single charged, which leads to a different coulombic interaction with the OH-SAM electrode.

Plotting and smoothing the averaged desorption forces of the three cycles versus the corresponding potentials yielded an approximately linear increase of the desorption force in the anodic direction up to  $25 \pm 3$  pN, whereby the increase started at  $-0.13 \pm 0.04$  V (Figure 4.3 A). In analogy to the well-established voltammogram, where the current is plotted against the potential, this plot is called “roburogram” according to the Latin word “robur” meaning also “force”. The approximately linear decrease of the

desorption force in the cathodic direction was slightly faster as no detachments were detected below  $0.00 \pm 0.04$  V. This hysteresis indicates memory effects of the electrode on a timescale, which is much slower than the recharging of the surface. The timescale for recharging the surface is on the order of  $\tau \approx 10 \text{ M}\Omega \cdot 10 \text{ nF} = 0.1 \text{ s}$ .

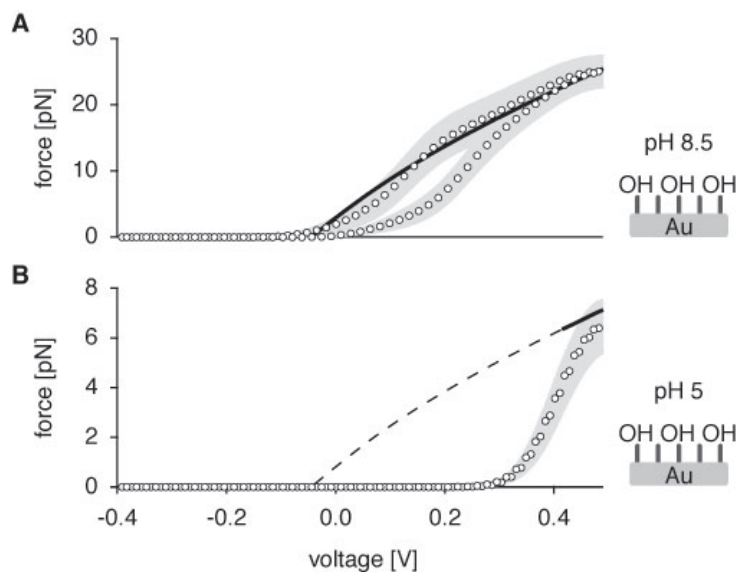


**Figure 4.3** Roburogram of dsDNA on the OH-SAM and NH<sub>2</sub>-SAM electrode: rupture force vs. applied potential. **(A)** Plotting and smoothing the averaged rupture forces (roburo means force in Latin) of the three cycles from Figure 4.2 B versus the corresponding potentials yielded a monotonic increase of the rupture force in the anodic direction up to  $25 \pm 3$  pN (upper curve), whereby the increase started at  $-0.13 \pm 0.04$  V. The approximately linear decrease of the rupture force in the cathodic direction was slightly faster as no rupture events were detected below  $0.0 \pm 0.04$  V (lower curve). A value  $\tau = 2.3 \text{ e}^-/\text{nm}$  was determined to fit the measured rupture forces indicating a higher line charge density at the double charged 5'-end of the dsDNA (black line). **(B)** The analogue experiment at pH 5 with the 5'-end being single charged showed a rupture force increase up to  $7 \pm 1$  pN. The black line represents a theoretical fit with a homogeneous line charge density of the dsDNA for  $\tau = 0.7 \text{ e}^-/\text{nm}$ . The discrepancy between the measured forces and the theoretical fit at potentials between 0.0 V and +0.4 V (dashed line) is due to the resolution limit of our instrument. In all plots, circles indicate the mean of a binning interval; grey errors bars represent the standard error of the mean.

A representative, low-pass filtered force extension curve for a single dsDNA molecule desorbed from the OH-SAM electrode at +0.5 V is depicted in Figure 4.4 A. The desorption process is characterized by a plateau at approximately 7 pN followed by a force peak of 30 pN at approximately 600 nm. In order to demonstrate this process in detail, 32 representative force extension curves have been averaged in Figure 4.4 B. Here, the desorption plateau around 7 pN is clearly distinguishable. Earlier studies had shown that this plateau stems from the reversible segment-by-segment desorption of the DNA, whereas the gradual increase of the force towards the end of the plateau and the sudden drop indicate a localized interaction of the terminal end of the DNA. The gradual increase was thus fitted by a worm-like-chain fit (WLC) [45].

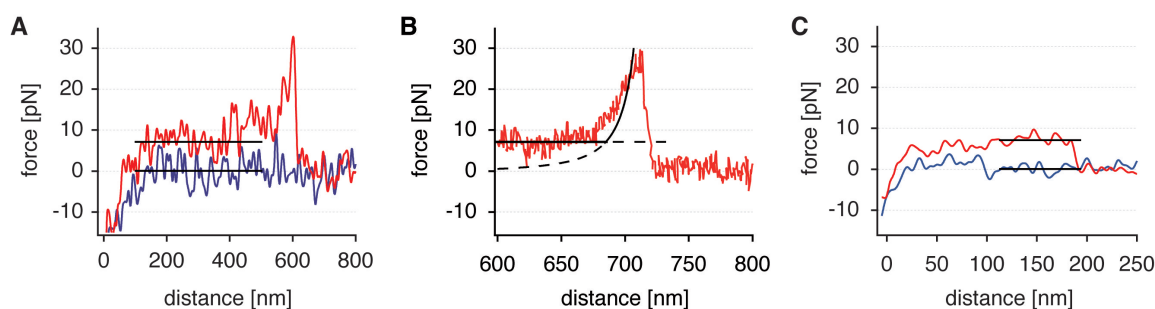


**Figure 4.4** Low pass-filtered force extension curves of dsDNA on the OH-SAM at +0.5 V. **(A)** At pH 8.5, the desorption process between a dsDNA molecule and the OH-SAM manifested itself in a single rupture event with forces around 30 pN due to the double charged 5'-end of the dsDNA. Before, a low desorption plateau of constant force ( $\sim 7$  pN) could be monitored (black lines). **(B)** An overlay of 32 force extension curves shows this process in detail. A worm-like-chain fit and the theoretical plateau of constant force (black curves) do not sufficiently match the force extension curve due to the simultaneous desorption and entropic stretching of the dsDNA molecule before dissociation. **(C)** The pronounced rupture force peak disappears at pH 5 and only a plateau of constant force around 7 pN (black lines) was detected due to the homogenous line charge density of the dsDNA in this pH-regime. In all graphs, the blue force extension curves indicates the approach to the surface, the red curves represent the retraction of the cantilever.

### Coulombic contributions of the backbone and end of dsDNA

With regard to the dsDNA structure and the force extension curve in Figure 4.4, a weak interaction between the negatively charged, but screened backbone of the dsDNA [46, 47] and a more pronounced interaction with the negatively charged 5'-end of the dsDNA with the positively charged OH-SAM electrode was assumed. Due to its asymmetric phosphodiester bonding, the 5'-end of a DNA-strand exhibits a terminal phosphate group, which is double negatively charged above pH 6 [48]. Consequently, a negatively charged molecule with a double negatively charged “anchor” at its end was desorbed at pH 8.5. To test the assumption of a negative anchor, the same experiment was conducted at pH 5 (Figure 4.2 B, Figure 4.3 B), whereby the terminal phosphate group is expected to provide only a single charge due to proton association [49]. At pH 5, the charge of the dsDNA-backbone remains unchanged. Only weak desorption plateaus in the range of 7 pN at +0.5 V could be detected, which is in good agreement to the desorption plateaus at pH 8.5 (Figure 4.4). Furthermore, the assumption of a charged backbone without a negative anchor at pH 5 is confirmed. The corresponding roburogram at pH 5 is depicted in Figure 4.3. The force increase up to  $7 \pm 1$  pN at +0.5 V was first observed at higher applied potentials due to the resolution limit of the instrument.

The measured forces at pH 5 in Figure 4.3 were fitted with Equation 4.1 by calculating the surface charge density according to the applied potentials  $\phi$  (Equation 4.4). Thereby, the literature value  $\tau = 0.7 e^-/\text{nm}$  for a homogenous line charge density was used [50, 51]. The expected desorption force is 7 pN (for an applied potential  $\phi = +0.5$  V and the used OH-SAM with alkyl chains of 11 carbon atoms), which is in good

agreement with the measured plateau force in the range of 7 pN at pH 5 with the 5'-end being single charged. The discrepancy between the measured forces and the theoretical fit at potentials between 0.0 V and +0.4 V (dashed line) is explained by the resolution limit of our instrument.

Because at pH 8.5 the double charged 5'-end interacted with the OH-SAM electrode, a higher line charge density at the end of the dsDNA-backbone was expected. The measured rupture forces were therefore fitted with a value of  $\tau = 2.3 e^-/\text{nm}$ , indicated by the black line in Figure 4.3. This value was also estimated with the adsorbed minimum length  $l_{min}$ , which was introduced in section 3.1, Equation 3.3. With experimental values of  $F_c = 25$  pN and  $v = 1500$  nm/s,  $l_{min} = 2.9$  nm was estimated for the last dsDNA segment before the final detachment. The mechanical work done by cantilever to remove this minimum length is then  $W_{mech} = F_c \cdot l_{min} = 74$  pNnm. This work equals the electrostatic energy to adsorb the dsDNA to the OH-SAM:  $W_{mech} = W_{el} = l_{min} \cdot \tau \cdot \psi_D$ . Thus, the corresponding line charge density is estimated to be  $\tau = 2.2 e^-/\text{nm}$ , which is in good agreement with the fit value from Figure 4.3.

### Further experiments

In a side study, the lateral mobility of the dsDNA on the OH-SAM was also proven to exclude pinning effects, which might cause the discussed phenomena. Thereby, the angular retraction protocol of section 3.2 was employed and a friction coefficient  $\zeta = 1.4 \pm 0.3 \times 10^{-6}$  Ns/m for dsDNA on the OH-SAM electrode ( $\phi = 0.5$  V) was determined. Further studies at different applied potential could answer the question, if also the friction of single polymers on surface can be manipulated via external control.

As a next step, potential dependent experiments on an NH<sub>2</sub>-SAM covered electrode were conducted to investigate the adsorption characteristics on an electrode with positively charged groups in combination with an applied potential. At pH 8.5, an electric manipulation could not be observed due to the dominating positively charged NH<sub>3</sub><sup>+</sup>-groups as the coulombic contribution of the NH<sub>3</sub><sup>+</sup>-groups (100 - 300 pN) is one order of magnitude higher than the coulombic contribution of the applied potential (25 pN). However, at pH 11 with the NH<sub>2</sub>-groups being uncharged, the desorption force could be altered in the range of 20 pN similar to the OH-SAM electrode. The data and a detailed discussion can be found in the attached publication. Further studies could include - besides different polymers - the variation of the alkane chain length of the SAM as well as different end groups on the SAM, different ion species and concentrations in the solution in order to explore the range of electrical control of the desorption force.

The discussed experiments quantify for the first time the electrical modulation of the adhesion force of DNA on electrodes with different surface properties. Thereby, the coulombic contributions of the backbone charges and the terminal phosphate charges were measured and identified at different pH-values; these results could be corroborated by theoretical considerations. Finally, the electrical adsorption control for single polymers offers a broad range of new technological applications (e.g. new polymer sensors and assays) and leads to an improved understanding between polyelectrolytes and substrates at the molecular level.

# Electrically controlled DNA adhesion

M. Erdmann<sup>1</sup>, R. David<sup>1,2</sup>, A. R. Fornof<sup>1</sup> & H. E. Gaub<sup>1</sup>

**We employed AFM based single molecule force spectroscopy to characterize the interaction of individual dsDNA molecules with a gold electrode covered by a self-assembled monolayer. With the composition of this monolayer we biased the Coulomb interaction with the DNA and we then externally controlled the adhesion via the electrode potential. We found that positive electrode potentials induced the adsorption of individual dsDNA molecules onto the OH-terminated SAM resulting in adhesion forces of up to 25 pN (at +0.5 V vs. Ag/AgCl). By applying negative voltages we could completely suppress dsDNA adsorption onto the OH-SAM. We were able to distinguish between the contributions of the backbone phosphate charges and the double charged terminal phosphate and corroborated our results with a model based on Gouy-Chapman-Theory. Analogue experiments on an NH<sub>2</sub>-SAM electrode resulted in similar adhesion forces but proved to be largely insensitive to external potential changes.**

The interaction of DNA with solid substrates is of utmost interest for a broad range of technological applications, e.g. in the development of new assays or the assembly of DNA-based supramolecular structures such as DNA-origamis or alike.<sup>1,2</sup> Quite generally interactions between charged polymers and charged surfaces are ubiquitous in nature, e.g. DNA/lipid or protein/cell-membrane complexes but also in material sciences e.g. in composite materials, paints or adhesives. Essential is thus an improved understanding of such interactions between polyelectrolytes and substrate at the molecular level.<sup>3,4</sup>

During the last decade, the Atomic Force Microscope (AFM) was increasingly employed as sensitive and versatile tool to study the adhesion strength of single polymers on charged surfaces.<sup>5,6</sup> Thereby, desorption forces and surface-bonding energies of single polymers on surfaces could be determined. Moreover, Hugel et al. revealed an electrostatic contribution of the desorption force, which could be controlled by varying the line charge density of the polymer, the salt concentration of the buffer solution and the surface charge, respectively.<sup>7</sup> From these findings follows the motivation to control and manipulate the desorption force of single polymers from electrodes with

external adjustable surface potential rather than by changing global parameters of the sample like the buffer solution or the polymer itself. A logical consequence is thus to combine AFM-based single molecule force spectroscopy with the potentiostatic control of the surface potential.

Rant et al. had shown that double stranded DNA (dsDNA) oligos, which were fluorescently labelled and covalently bound to a SAM-modified gold electrode, could be reversibly switched between different conformations. Applying positive potentials to the electrode attracted and adsorbed the dsDNA, thereby the fluorescent dye was quenched and the light emission decreased. Negative potentials expelled the dsDNA from the surface and reduced quenching of the fluorescent dye but increased again the light emission.<sup>8,9</sup> A similar experiment with a diluted SAM on a gold electrode revealed a reversibly switching of surface properties: the hydrophilic carboxylate end groups were attracted and bent towards the electrode at positive potentials. Thereby, the hydrophobic alkyl chain was exposed to the solution and thus changed the global state of the electrode from hydrophilic to hydrophobic.<sup>10</sup> These experiments clearly demonstrated that the adsorption of polymers on electrodes may be influenced by an applied potential. Nevertheless, to the best of our knowledge no absolute values of the adhesion forces of polymers being adsorbed on electrodes under potentiostatic control have been reported so far. For this reason we conducted AFM force spectroscopy measurements with dsDNA covalently bound to the AFM-tip and desorbed this dsDNA from a SAM-modified gold electrode under potentiostatic control (Fig. 1).

## dsDNA desorption from an OH-SAM electrode

In all experiments, a heterogeneous, 4.9 kbp long dsDNA sequence was covalently bound to the AFM-tip (see Supplementary Information). The experiments were accomplished in a solution containing 100  $\mu$ M MgCl<sub>2</sub> and traces of NaOH to establish a value of pH 8.5 and 11 or HCl for a value of pH 5. As described in the Supplementary Information, the cantilever is gold-coated on both sides for laser beam reflection and for covalent attachment of the dsDNA. Thus, it can be

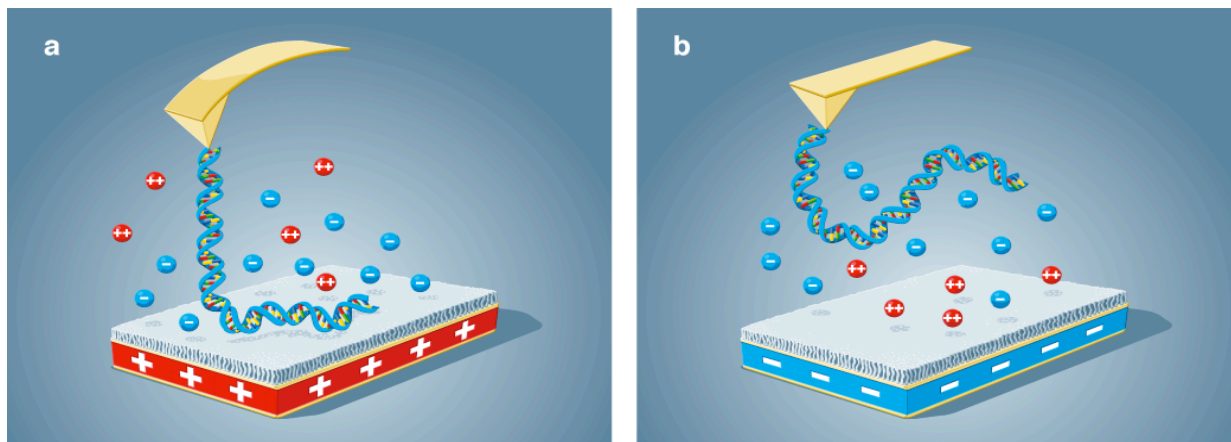


**Figure 1. Idealized representation of the single molecule desorption experiments on an OH-SAM electrode.** 4.9kbp dsDNA was covalently bound to an AFM tip, and the functionalized tip was brought into contact with a gold microelectrode covered by an OH-SAM. An aqueous magnesium chloride solution was used, and the surface potential was controlled by a potentiostat (not shown). **a**, Positive surface potentials induced the adsorption of dsDNA on the OH-SAM resulting in adhesion forces of up to 25 pN (at +0.5 V vs. Ag/AgCl). **b**, In case of applied negative surface potentials, no dsDNA adsorption on the OH-SAM was observed.

<sup>1</sup>Chair for Applied Physics and Center for NanoScience, Ludwigs-Maximilians-Universität Munich, Amalienstrasse 54, 80799 Munich

<sup>2</sup>Center for Integrated Protein Science Munich

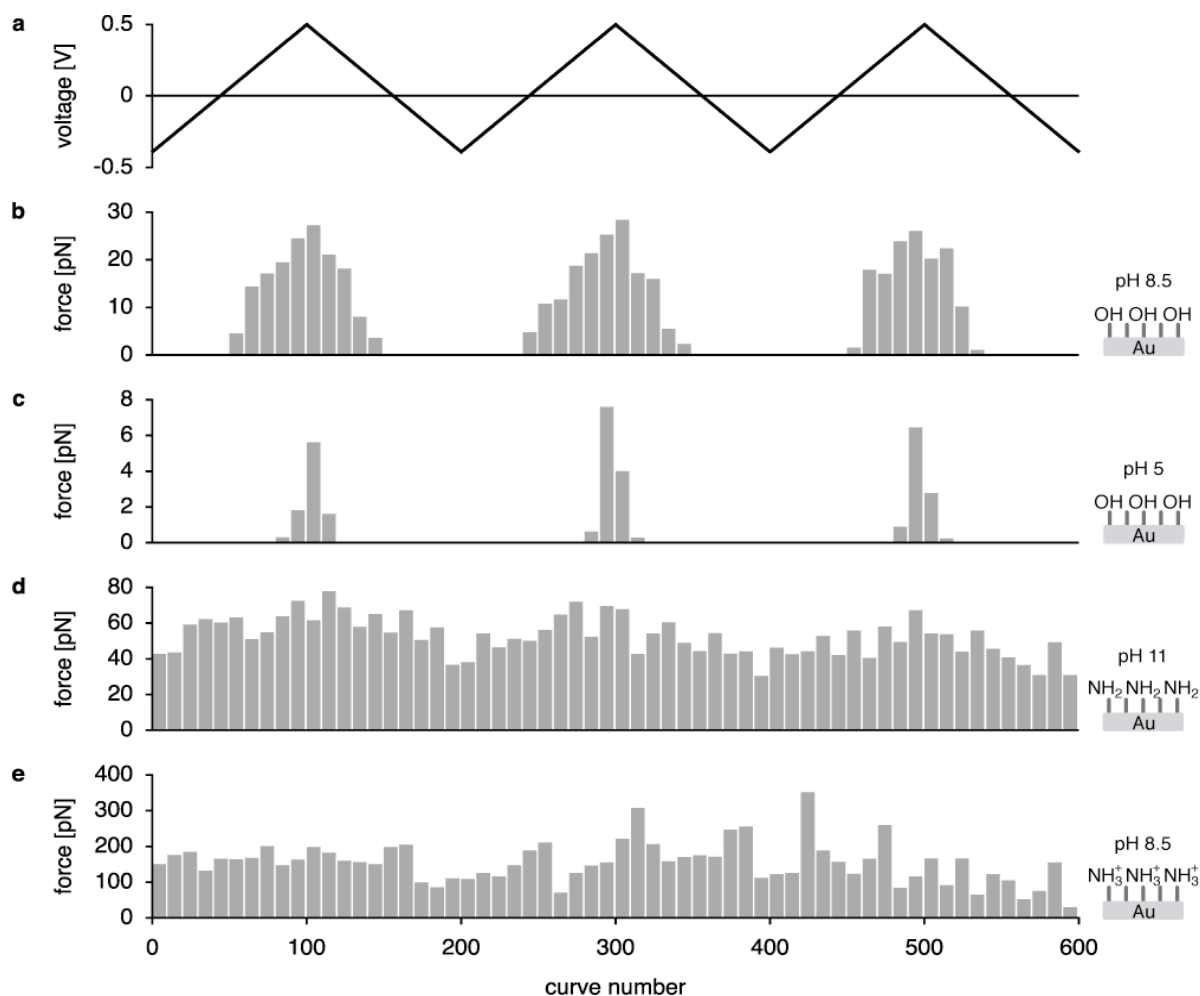


**Figure 2. Polarized SAM electrodes and dsDNA rupture forces.** **a**, A SAM electrode was polarized between -0.4 V and 0.5 V. **b**, At pH 8.5, the rupture force distribution for the OH-SAM electrode showed symmetrical force peaks up to 25 pN only around +0.5 V. **c**, The same experiment at pH 5 revealed rupture forces around 7 pN. **d**, For uncharged amino groups at pH 11, the rupture forces could be altered in the range of 20 pN around a non-coulombic force of 50 pN at 0.0 V. **e**, Protonated amino-groups ( $\text{NH}_3^+$ ) at pH 8.5 caused non-manipulable rupture forces around 200 pN.

regarded as a fourth, free-floating electrode in the three-electrodes potentiostatic setup. Due to the multiple metal coatings of the cantilever, the resulting bimetal artefacts caused by ion currents were therefore minimized by low salt concentrations in the  $\mu\text{M}$ -regime. Cations like  $\text{Mg}^{2+}$  normally screen the negatively charged backbone of the dsDNA and prevent melting of the complementary DNA strands.<sup>11-13</sup> Due to the low salt concentration, particularly long dsDNA was chosen to prevent unintended melting as the melting temperature of dsDNA increases with the contour length.<sup>14-16</sup> Additionally, we conducted a melting experiment with the dsDNA in 100  $\mu\text{M}$   $\text{MgCl}_2$  and determined a melting temperature of 84.3  $^\circ\text{C}$ , which proves the high thermal stability of the dsDNA (see Supplementary Information). Moreover, microelectrodes were utilized in order to guarantee low ion currents as the current is proportional to the electrode surface.<sup>17</sup>

First, we brought the dsDNA functionalized AFM tip into contact with a SAM-modified gold electrode under potentiostatic control, whereby the alkyl chains were terminated by a hydroxyl group (-OH). We analyzed only the last force step between dsDNA and the OH-SAM to ensure the measurement of a single molecule detachment. The measurement protocol was analogous to cyclic staircase voltammetry:<sup>18-20</sup> the potential between the OH-SAM electrode (working electrode) and the Ag/AgCl reference electrode was linearly ramped between -0.4 V and 0.5 V (see Fig. 2a and Supplementary Information). Simultaneously,

the desorption force and the current were recorded. In order to minimize artefacts in the deflection signal, which are related to the ion current, the potential was changed by 10 mV steps after each force extension trace with the AFM-tip being placed 3  $\mu\text{m}$  away from the electrode. When the AFM-tip with the dsDNA then approached the surface again, the surface polarization was equilibrated according to the applied potential until the ion current ceased (data not shown). Thus, the discussed artefacts in the deflection signal could be minimized, too.

Fig. 2b shows the desorption force distribution of dsDNA on the OH-SAM vs. the curve number at pH 8.5. The resulting desorption force distribution shows well defined and almost symmetrical force peaks in the positive range around +0.5 V with a force maximum of about 25 pN, whereas no interaction between dsDNA and the OH-SAM was measured at negative potentials. This cycling process was reversible over a large number of force curves. Plotting and smoothing the averaged desorption forces of the three cycles versus the corresponding potentials yielded an approximately linear increase of the desorption force in the anodic direction up to  $25 \pm 3$  pN, whereby the increase started at  $-0.13 \pm 0.04$  V (Fig. 3a). In analogy to the well-established voltammogram, where the current is plotted against the potential, we call this plot “roburogram” according to the Latin word “robur” meaning also “force”. The approximately linear decrease of the desorption force in the cathodic direction was slightly faster as no



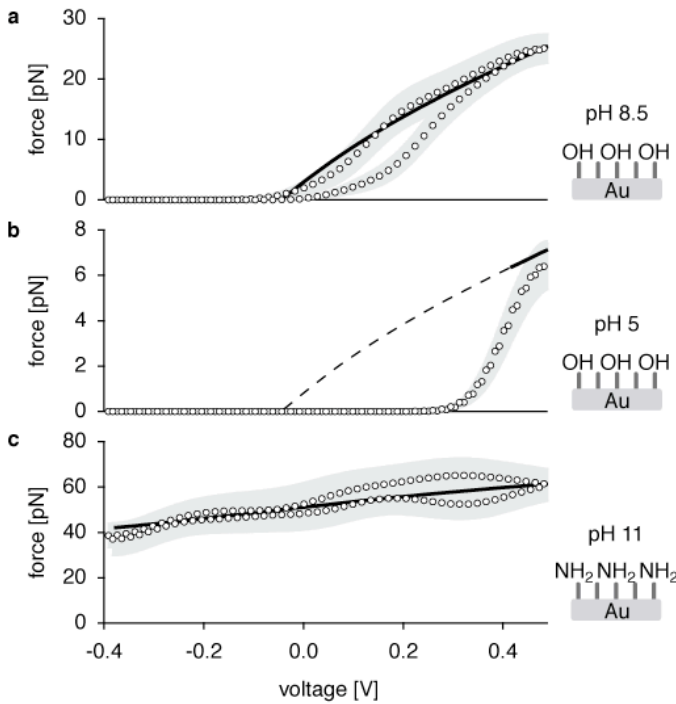


**Figure 3. Rupture force vs. potential.** **a**, Plotting and smoothing the averaged rupture forces from Fig. 2b versus their potentials yielded a monotonic increase of the rupture force up to  $25 \pm 3$  pN (black fit line:  $\tau = 2.3$  e-/nm). **b**, At pH 5, the rupture force increased up to  $7 \pm 1$  pN (black fit line:  $\tau = 0.7$  e-/nm). **c**, The uncharged  $\text{NH}_2$ -SAM electrode shows a monotonic rupture force increase from 40 pN to 60 pN. In all plots, circles indicate the mean of a binning interval; grey errors bars represent the standard error of the mean.

detachments were detected below  $0.0 \pm 0.04$  V. This hysteresis indicates memory effects of the electrode on a timescale, which is much slower than the recharging of the surface. The timescale for recharging the surface is on the order of  $\tau \approx 10 \text{ M}\Omega \cdot 10 \text{ nF} = 0.1$  s. The corresponding last rupture length distributions of Fig. 2 and 3 are discussed in the Supplementary Information.

A representative, low-pass filtered force extension curve for a single dsDNA molecule desorbed from the OH-SAM electrode at +0.5 V is depicted in Fig. 4a. The desorption process is characterized by a plateau at approximately 7 pN followed by a force peak of 30 pN at approximately 600 nm. In order to demonstrate this process in detail, 32 representative force extension curves have been averaged in Fig. 4b. Here, the desorption plateau around 7 pN is clearly distinguishable. Earlier studies had shown that this plateau stems from the reversible segment-by-segment desorption of the DNA,<sup>4</sup> whereas the

gradual increase of the force towards the end of the plateau and the sudden drop indicate a localized interaction of the terminal end of the DNA. The gradual increase was thus fitted by a worm-like-chain fit (WLC), the basic model for entropy elasticity.<sup>11,21</sup>

### Theoretical description of dsDNA desorption

Which mechanism causes the observed phenomena? With regard to the dsDNA structure, we assume a weak interaction between the negatively charged, but screened backbone of the dsDNA<sup>12,13,22</sup> and a more pronounced interaction with the negatively charged 5'-end of the dsDNA with the positively charged OH-SAM electrode. Due to its asymmetric phosphodiester bonding, the 5'-end of a DNA-strand exhibits a terminal phosphate group, which is double negatively charged above pH 6.<sup>23</sup> At pH 8.5, we consequently desorb a negatively charged molecule with a double negatively charged “anchor” at its end. To test the assumption of a negative anchor, we conducted the same experiment at pH 5, whereby the terminal phosphate group is expected to provide only a single charge due to proton association.<sup>24</sup> At pH 5, the charge of the dsDNA-backbone remains unchanged. We could only detect weak desorption plateaus in the range of 7 pN at +0.5 V, which is in good agreement to the desorption plateaus at pH 8.5 (Fig. 4c). Furthermore, the assumption of a charged backbone without a negative anchor at pH 5 is confirmed. Switching the pH value back to pH 8.5 provided again the same force extension curves. The corresponding roburogram at pH 5 is depicted in Fig. 3b. The force increase up to  $7 \pm 1$  pN at +0.5 V was first observed at higher applied potentials due to the resolution limit of the instrument.

In order to provide a quantitative description of the described desorption phenomena, we applied the desorption model introduced by Netz et al. and tested several years ago in numerous experiments.<sup>7,25-27</sup> Within this model, the desorption force  $F_c$  is described by

$$F_c = F_0 + 4\pi l_B k_B T \kappa^{-1} \tau \cdot \sigma \quad (1)$$

with  $l_B$  being the Bjerrum length (0.71 nm in water), the thermal energy  $k_B T$  (4.12 pNnm), the Debye screening length  $\kappa^{-1}$ ,  $\tau$  the line charge density in  $\text{nm}^{-1}$  of the polymer and the surface charge density  $\sigma$  in  $\text{nm}^{-2}$ . The non-coulombic term  $F_0$  contains forces ascribed to van-der-Waals forces, hydrogen bonding or hydrophobic effects etc. Here,  $F_0$  is not considered in a first approximation, since the adsorption of dsDNA to the OH-SAM starts and ends around 0 V. Moreover, a negligible surface charge is assumed at this applied potential as the potential of zero charge (pzc) is  $\phi_{pzc} = 0.0$  V vs. the Ag/AgCl electrode.<sup>28</sup> The surface charge density can be adjusted by the potentiostat as

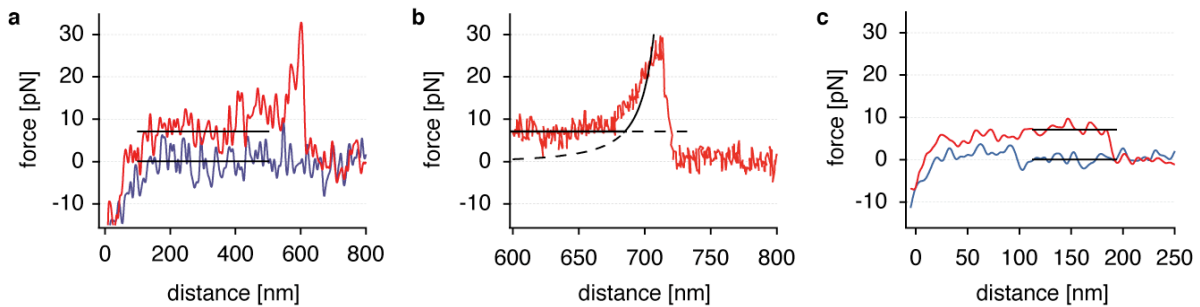


**Figure 4. Low-pass filtered force extension curves of dsDNA on the OH-SAM at +0.5 V.** **a**, At pH 8.5, the desorption process between a dsDNA molecule and the OH-SAM manifested itself in a desorption plateau of constant force ( $\sim 7$  pN) and a single rupture event ( $\sim 30$  pN). **b**, An overlay of 35 force extension curves shows a crossover between constant adhesion and worm-like chain stretching (black curves). **c**, Only a plateau of constant force around 7 pN was detected at pH 5.

described above, whereas the product  $\kappa^{-1}\tau$  was controlled in previous experiments by varying the line charge density or salt concentration, respectively. Here, the Debye screening length is 19 nm for a 2:1 electrolyte at 100  $\mu\text{M}$  concentration.<sup>17</sup> The effective line charge density for the dsDNA backbone is 0.7  $e/\text{nm}$  for an electrolyte containing divalent cations, whereby counterion condensation according to the Manning theory is taken into account.<sup>29,30</sup> Calculating the surface charge density on the OH-SAM electrode, required a model for the diffuse layer potential recently tested.<sup>28,31</sup> The surface charge density can then be calculated from the diffuse layer potential by the Grahame equation.<sup>17</sup> The relation between the applied potential  $\phi$  and the resulting diffuse layer potential  $\psi_D$  is given by:

$$\psi_D(\phi) = \frac{C_L}{C_L + C_D(\psi_D)} (\phi - \phi_{pzc}), \quad (2)$$

whereby  $C_L = 0.8 \mu\text{F}/\text{cm}^2$  and  $C_D(\psi_D)$  are the capacitances of the OH-SAM and the diffuse layer, respectively.<sup>28</sup> These two capacitances model in a first approximation the potential drop between the gold electrode and the insulating SAM layer and as well as the diffuse counterion layer. Thereby, a specific ion adsorption on the OH-SAM (Stern-layer) is not taken into account. The potential of zero charge  $\phi_{pzc}$  adjusts the diffuse layer potential with respect to the reference electrode. Moreover, the Gouy-Chapman theory<sup>17</sup> yields for the diffuse layer capacitance

$$C_D(\psi_D) = \left( \frac{2z^2 e^2 \epsilon \epsilon_0 n^0}{k_B T} \right)^{1/2} \cosh \left( \frac{ze\psi_D}{2k_B T} \right), \quad (3)$$

where  $z$  is the magnitude of charge on the ions,  $e$  is the electron charge,  $\epsilon \epsilon_0$  is the total permittivity of water and  $n^0$  is the number concentration of each ion in the bulk. We use this analytical expression for the asymmetrical 2:1 electrolyte  $\text{MgCl}_2$  and take only the  $\text{Cl}^-$  counterions at positive surface potentials into account, as little error is expected in this approximation.<sup>32,33</sup> Inserting this relationship into equation (2) results in a transcendental expression for the diffuse layer potential  $\psi_D$ , which was solved numerically for different applied potentials  $\phi$ . The Grahame equation then delivers the surface charge density  $\sigma$  on the OH-SAM, which is responsible for the diffuse potential above the electrode:

$$\sigma = -\sigma_D(\psi_D) = \left( 8k_B T \epsilon \epsilon_0 n^0 \right)^{1/2} \sinh \left( \frac{ze\psi_D}{2k_B T} \right). \quad (4)$$

Thus, the resulting desorption force can be calculated according to equation (1) and is plotted versus the applied potential in Fig. 3. The black line in Fig. 3b represents the expected desorption force for a homogeneous line charge density of 0.7  $e/\text{nm}$ , whereby a maximum force of 7 pN was calculated at an applied potential of 0.5 V. This maximum force is in good agreement with the measured plateau forces in the range of 7 pN at pH 5 with the 5'-end being single charged. The discrepancy between the measured forces and the theoretical fit at potentials between 0.0 V and +0.4 V (dashed line) is explained by the resolution limit of our instrument. However, as a double negatively charged 5'-end of the dsDNA interacted with the OH-SAM, we also expected a higher line charge density at the end of the dsDNA-backbone. The measured rupture forces were therefore fitted with a value of  $\tau = 2.3 e/\text{nm}$ , indicated by the black line in Fig. 3a. This value can also be estimated by a recently published method to describe the minimum adsorbed length during the desorption process of an adsorbed polymer.<sup>4</sup> Thereby, a two-state dissociation process between the last bound polymer segment and the surface is assumed and the minimum adsorbed length is estimated by the Bell-Evans model.<sup>34</sup> This model basically reflects the balance between the adhesion free enthalpy of  $l_{\min}$  and its thermal energy:

$$l_{\min} \approx -\frac{k_B T}{F_c} \cdot \ln \left( \frac{F_c}{k_B T} \cdot \frac{v}{v_{\text{off}}} \right) + \kappa^{-1}. \quad (5)$$

Here,  $v$  is the retract velocity of the AFM-tip and  $v_{\text{off}}$  is the attempt frequency of the thermal activation. The second part in equation (5), the Debye screening length, was introduced to take care of thermal fluctuations within the coulomb screening. However, since the persistence length of dsDNA ( $\sim 50$  nm) is much higher than the Debye screening length (19 nm), fluctuations of these long dsDNA persistence parts are not expected and the dsDNA is desorbed segment after segment, which are smaller than the persistence length. Hence, the Debye screening length in equation (5) is cancelled and the minimum adsorbed length for dsDNA on the OH-SAM is then  $l_{\min} = 2.9$  nm for  $v = 1500$  nm/s and  $v_{\text{off}} = 10^{12}$  s<sup>-1</sup>. The mechanical work done by the cantilever to remove this minimum length is  $W_{\text{mech}} = F_c \cdot l_{\min} = 74$  pNnm. This work equals the electrostatic energy to adsorb the dsDNA to the OH-SAM:  $W_{\text{mech}} = W_{\text{el}} = l_{\min} \cdot \tau \cdot \psi_D$  ( $\psi_D = 0.07$  V at an applied potential of  $\phi = 0.5$  V). Thus, the corresponding line charge density is estimated to be  $\tau = 2.2 e/\text{nm}$ , which is in good agreement with the fit value from Fig. 3a. This estimate further confirms the assumption of a higher negatively charged 5'-end of the dsDNA leading to higher desorption forces. Finally, the lateral mobility of the dsDNA on the OH-SAM electrode was proven by measuring the desorption lengths by angular retraction protocols.<sup>4</sup> As the dsDNA is laterally mobile on the OH-SAM, pinning effects, which might cause the discussed phenomena, can be excluded (see Supplementary Information).

### dsDNA desorption from an $\text{NH}_2$ -SAM electrode

As a next step, we also conducted the potential dependent experiments on an  $\text{NH}_2$ -SAM covered electrode to investigate the adsorption characteristics on an electrode with positively charged groups in combination with an applied potential. At pH 8.5, an electric manipulation could not be observed due to the dominating positively charged  $\text{NH}_3^+$ -groups (Fig. 2e), as the coulombic contribution of the  $\text{NH}_3^+$ -groups (100 - 300 pN) is one order of magnitude higher than the coulombic contribution of the applied potential ( $\sim 25$  pN). These high rupture forces in the range of 100 - 300 pN induced only the melting of the dsDNA strand.<sup>11,35,36</sup> However, at pH 11 with the  $\text{NH}_2$ -groups being uncharged, the desorption force could be altered in the range of 20 pN similar to the OH-SAM electrode (Fig. 2d). Here, a non-coulombic force of  $F_0 = 50$  pN was determined and a rougher force spectrum was observed in comparison to the OH-SAM electrode. The roughness may be related to non-coulombic effects, which are responsible for the high bias force  $F_0$  arising from van der Waals and hydrophobic forces.<sup>6,37</sup> The corresponding roburogram (Fig. 3c) clearly demonstrates the electric manipulation of the desorption force in the range of 20 - 30 pN. For the theoretical fit indicated as a black line, a capacitance of  $C_L = 0.25 \mu\text{F}/\text{cm}^2$  was determined, whereby the remaining parameters were not changed. Analogously, a potential of zero charge of  $\phi_{pzc} = 0.0$  V was assumed because of the symmetrical force increase/decrease around 0 V.

### Conclusion

Our experiments quantify for the first time the electrical modulation of the adhesion force of DNA on electrodes with different surface properties. This study demonstrates quite generally the range of possibilities to manipulate electrically the desorption force of molecules on SAMs. Further studies could include - besides different polymers - the variation of the alkane chain length of the SAM as well as different end groups on the

SAM, different ion species and concentrations in the solution in order to explore the range of electrical control of the desorption force. Nevertheless, more detailed models and further experiments will be necessary to explain the hysteresis that we found in the cathodic direction.

### Acknowledgments

We thank R.Netz, D. Ho, T. Hugel, W. Schuhmann and G. Papastavrou for helpful discussions. This work was supported by the German Science Foundation (SFB 486) and the Nanosystems Initiative Munich (NIM). AF thanks the Alexander von Humboldt Foundation for their generous support.

### Author contributions

M.E., A.F. and H.E.G. conceived and designed the experiments and co-wrote the paper. M.E. performed the experiments and analysed the data. R.D. contributed the dsDNA and provided the tip- and electrode functionalization. All authors discussed the results and commented on the manuscript.

### Supplementary Information Available

Correspondence and requests for materials should be addressed to H.E.G.

### References

1. Rothmund, P.W.K. Folding DNA to create nanoscale shapes and patterns. *Nature* **440**, 297-302 (2006).
2. Jungmann, R., Liedl, T., Sobey, T.L., Shih, W. & Simmel, F.C. Isothermal assembly of DNA origami structures using denaturing agents. *Journal of the American Chemical Society* **130**, 10062-+ (2008).
3. Kuhner, F., Erdmann, M. & Gaub, H.E. Scaling exponent and Kuhn length of pinned polymers by single molecule force spectroscopy. *Physical Review Letters* **97**(2006).
4. Kuhner, F. et al. Friction of single polymers at surfaces. *Langmuir* **22**, 11180-11186 (2006).
5. Chatellier, X., Senden, T.J., Joanny, J.F. & di Meglio, J.M. Detachment of a single polyelectrolyte chain adsorbed on a charged surface. *Europhysics Letters* **41**, 303-308 (1998).
6. Hugel, T. et al. Elasticity of single polyelectrolyte chains and their desorption from solid supports studied by AFM based single molecule force spectroscopy. *Macromolecules* **34**, 1039-1047 (2001).
7. Seitz, M., Friedsam, C., Jostl, W., Hugel, T. & Gaub, H.E. Probing solid surfaces with single polymers. *Chemphyschem* **4**, 986-990 (2003).
8. Rant, U. et al. Dynamic electrical switching of DNA layers on a metal surface. *Nano Letters* **4**, 2441-2445 (2004).
9. Rant, U. et al. Switchable DNA interfaces for the highly sensitive detection of label-free DNA targets. *Proceedings of the National Academy of Sciences of the United States of America* **104**, 17364-17369 (2007).
10. Lahann, J. et al. A reversibly switching surface. *Science* **299**, 371-374 (2003).
11. Marko, J.F. & Siggia, E.D. Stretching DNA. *Macromolecules* **28**, 8759-8770 (1995).
12. Chiu, T.K. & Dickerson, R.E. 1 angstrom crystal structures of B-DNA reveal sequence-specific binding and groove-specific bending of DNA by magnesium and calcium. *Journal of Molecular Biology* **301**, 915-945 (2000).
13. Bai, Y. et al. Quantitative and comprehensive decomposition of the ion atmosphere around nucleic acids. *Journal of the American Chemical Society* **129**, 14981-14988 (2007).
14. Schildkraut, C. & Lifson, S. Dependence of Melting Temperature of DNA on Salt Concentration. *Biopolymers* **3**, 195-& (1965).
15. SantaLucia, J. A unified view of polymer, dumbbell, and oligonucleotide DNA nearest-neighbor thermodynamics. *Proceedings of the National Academy of Sciences of the United States of America* **95**, 1460-1465 (1998).
16. Lee, L., Johnston, A.P.R. & Caruso, F. Manipulating the Salt and Thermal Stability of DNA Multilayer Films via Oligonucleotide Length. *Biomacromolecules* **9**, 3070-3078 (2008).
17. Bard, A.J. & Faulkner, L.R. *Electrochemical Methods: Fundamentals and Applications* (Wiley & Sons, 2000).
18. Christie, J.H. & Lingane, P.J. Theory of Staircase Voltammetry. *Journal of Electroanalytical Chemistry* **10**, 176-& (1965).
19. Ferrier, D.R. & Schroeder, R.R. Staircase Voltammetry with Varied Current Sampling Times - Theory for Diffusion Controlled, Rate Controlled, and Mixed Rate and Diffusion Controlled Electrode-Reactions. *Journal of Electroanalytical Chemistry* **45**, 343-359 (1973).
20. Zipper, J.J. & Perone, S.P. Theoretical and Experimental Evaluation of Staircase Voltammetry. *Analytical Chemistry* **45**, 452-458 (1973).
21. Bustamante, C., Marko, J.F., Siggia, E.D. & Smith, S. Entropic Elasticity of Lambda-Phage DNA. *Science* **265**, 1599-1600 (1994).
22. Netz, R.R. & Joanny, J.F. Complexation behavior of polyampholytes and charged objects. *Macromolecules* **31**, 5123-5141 (1998).
23. Lehninger, A., Cox, M. & Nelson, D.L. *Lehninger Principles of Biochemistry*, (W H Freeman & Co, 2008).
24. Kosenkov, D., Gorb, L., Shishkin, O.V., Spöner, J. & Leszczynski, J. Tautomeric equilibrium, stability, and hydrogen bonding in 2'-deoxyguanosine monophosphate complexed with Mg<sup>2+</sup>. *Journal of Physical Chemistry B* **112**, 150-157 (2008).
25. Sonnenberg, L., Parvole, J., Kuhner, F., Billon, L. & Gaub, H.E. Choose sides: Differential polymer adhesion. *Langmuir* **23**, 6660-6666 (2007).
26. Friedsam, C., Seitz, M. & Gaub, H.E. Investigation of polyelectrolyte desorption by single molecule force spectroscopy. *Journal of Physics-Condensed Matter* **16**, S2369-S2382 (2004).
27. Netz, R.R. & Joanny, J.F. Adsorption of semiflexible polyelectrolytes on charged planar surfaces: Charge compensation, charge reversal, and multilayer formation. *Macromolecules* **32**, 9013-9025 (1999).
28. Rentsch, S., Siegenthaler, H. & Papastavrou, G. Diffuse layer properties of thiol-modified gold electrodes probed by direct force measurements. *Langmuir* **23**, 9083-9091 (2007).
29. Manning, G.S. Molecular Theory of Polyelectrolyte Solutions with Applications to Electrostatic Properties of Polynucleotides. *Quarterly Reviews of Biophysics* **11**, 179-246 (1978).
30. Maier, B., Seifert, U. & Radler, J.O. Elastic response of DNA to external electric fields in two dimensions. *Europhysics Letters* **60**, 622-628 (2002).
31. Widrig, C.A., Chung, C. & Porter, M.D. The Electrochemical Desorption of N-Alkanethiol Monolayers from Polycrystalline Au and Ag Electrodes. *Journal of Electroanalytical Chemistry* **310**, 335-359 (1991).
32. Ross, S. & Morrison, I.D. *Colloidal Systems and Interfaces*, (Wiley & Sons, New York, 1988).
33. Chen, Z. & Singh, R.K. General solution for Poisson-Boltzmann equation in semiinfinite planar symmetry. *Journal of Colloid and Interface Science* **245**, 301-306 (2002).
34. Evans, E. & Ritchie, K. Dynamic strength of molecular adhesion bonds. *Biophysical Journal* **72**, 1541-1555 (1997).
35. Smith, S.B., Cui, Y.J. & Bustamante, C. Overstretching B-DNA: The elastic response of individual double-stranded and single-stranded DNA molecules. *Science* **271**, 795-799 (1996).
36. Rief, M., Clausen-Schaumann, H. & Gaub, H.E. Sequence-dependent mechanics of single DNA molecules. *Nature Structural Biology* **6**, 346-349 (1999).
37. Horinek, D. et al. Peptide adsorption on a hydrophobic surface results from an interplay of solvation, surface, and intrapeptide forces. *Proceedings of the National Academy of Sciences of the United States of America* **105**, 2842-2847 (2008).

# Supplementary Information

## Electrically controlled DNA adhesion

*Matthias Erdmann, Ralf David<sup>†</sup>, Ann Fornof and Hermann E. Gaub\**

Chair for Applied Physics and Center for NanoScience,

Ludwigs-Maximilians-Universität Munich,

Amalienstrasse 54, 80799 Munich

+ Center for Integrated Protein Science Munich

\*to whom the correspondence should be addressed. Email: [gaub@lmu.de](mailto:gaub@lmu.de)

## Material and Methods

**AFM.** We used a commercial instrument (Molecular Force Probe 3D from Asylum Research, Santa Barbara, CA/USA) and silicon nitride cantilevers (Veeco GmbH, Mannheim, Germany, MLCT-AUHW). The spring constants of each cantilever were individually calibrated by thermal calibration. Moreover, a PEEK-cantilever holder from Asylum Research was used to avoid metal parts in the solution.

**Samples.** dsDNA fragments of 4.9kbp (~100ng/ $\mu$ l concentration) were obtained from the vector pet28a by PCR, with an amino modified forward primer sequence from IBA GmbH, Germany. The dsDNA was purified with the Qiagen PCR Purification Kit. Gel electrophoresis was used to confirm the homogeneity of the DNA length.

Experiments were performed in 100  $\mu$ M MgCl<sub>2</sub> (water: chromatography water (LiChrosolv, Merck, Darmstadt)) containing traces of NaOH or HCl to ensure pH values of 5, 8.5 or 12, respectively. We checked the pH after 45 min, which is the timescale of an experiment, and did not observe significant changes. All chemicals were purchased from Sigma Aldrich if not otherwise identified.

The thermal stability of dsDNA in 100  $\mu$ M MgCl<sub>2</sub> was confirmed by absorbance versus temperature profiles in an UV/Vis spectrometer (Perkin Elmer Lambda 20).

**Tip functionalization.** The covalent attachment of dsDNA to the AFM tip was accomplished by covalent carboxyl amino group binding. Therefore, the cantilevers were coated with a 30Å chrome-nickel (80:20) layer followed by a 300Å layer of gold by thermal evaporation. These cantilevers were then etched for 2 min in a solution containing H<sub>2</sub>O (Milli-Q water), NH<sub>3</sub> (37%) and H<sub>2</sub>O<sub>2</sub> (30%) with the ratio 10:1:1 and then rinsed with ethanol (puriss.). Afterwards, the cantilevers were immediately incubated in a solution of 16-mercaptohexadecanoic acid (0.05 mM), 11-mercaptoundecanol (0.5 mM) and tris(2-carboxyethyl)phosphine-hydrochloride (TCEP, 0.05 mM) in ethanol (puriss.) for at least 12h. For the dsDNA functionalization, the cantilevers were first rinsed in chromatography water (LiChrosolv, Merck, Darmstadt). Then the carboxyl groups of the SAM reacted with the end amino groups of the dsDNA in a solution of 10 $\mu$ l DNA and 20 $\mu$ l chromatography water containing 1-ethyl-3-(3-dimethylaminopropyl) carbodiimide (EDC) for 30min. 15mg EDC were dissolved in 300  $\mu$ l chromatography water for the latter stock solution. The large excess of EDC enables the carboxy-amino coupling in the polar solution; the usage of chromatography water ensures constant coupling conditions at pH 7. After the functionalization, the cantilevers were rinsed thoroughly in the MgCl<sub>2</sub> solution and then immediately used for the experiments.

**Electrodes.** The gold electrodes were directly evaporated on a clean polycarbonate slide and had an area of 0.1 mm x 20 mm plus an area of 1 cm<sup>2</sup> for electrical contacting. The thickness of the electrode was 200 nm. A mask of stainless steel (Ätztechnik Herz GmbH&Co, Epfendorf, Germany) was used during thermal evaporation. The OH-SAM functionalization was accomplished similar to the cantilever function: the electrodes were etched for 2 min in a solution containing H<sub>2</sub>O (Milli-Q water), NH<sub>3</sub> (37%) and H<sub>2</sub>O<sub>2</sub> (32%) with the ratio 10:1:1 and then rinsed with ethanol (puriss.). Afterwards, the electrodes were immediately incubated in a solution of 11-mercaptoundecanol (0.05 mM) and tris(2-carboxyethyl)phosphine-hydrochloride (TCEP, 0.05 mM) in ethanol (puriss.) for at least 12h. For the NH<sub>2</sub>-SAM, 11-amino-undecanethiol was purchased from GERBU, Germany. Before use in the experiment, the electrodes were first rinsed with ethanol (puriss.) and the MgCl<sub>2</sub> solution. The electrodes were then gently dried with nitrogen to ensure a dry contacting area for BNC cables. For a three-electrode setup, a commercial Ag/AgCl microelectrode (Microelectrodes Inc., Bedford, USA) was used as reference electrode and a platinum wire as counter electrode. All potentials applied to the SAM electrodes are given versus the Ag/AgCl electrode. The counter and reference electrodes were inserted into a bare shaped cavity, which was milled into the polycarbonate slide before functionalization. Then the MgCl<sub>2</sub> solution was added to determine an effective electrode area of 0.1 mm x 10 mm covered by the solution. Before the AFM experiment, 20 cleaning voltammograms in the range of from -0.4 to 0.5 V were recorded with a sweep rate of 0.1 V/s. The SAMs proved to be highly stable during the experiment. An increase in the ionic currents or ox/red peaks was not observed.

**Measurements and Analysis.** (De-)adhesion forces and rupture lengths were measured on the OH-SAM electrode. The dsDNA-functionalized AFM tips were brought into contact with the surface for 0.5 s and retracted with a speed of 1.5 μm/s. In an experiment thousands of force curves were recorded with changing potential from curve to curve (10 mV potential change per curve). In order to minimize artefacts in the deflection signal, which are related to the ion current, the potential was changed by 10 mV steps after each force extension trace with the AFM-tip being 3 μm away from the electrode. The potential was adjusted by a commercial potentiostat (1002 PC.T., Jaissle Elektronik GmbH, Waiblingen, Germany), whereby a self-written procedure in Igor 6.0 controlled the potential change with regard to the AFM force curves. This procedure was implemented in the MFP3D-code. The last rupture forces and lengths were also determined by a self-written procedure in Igor 6.0. Additionally, the last ruptures force and length spectra being plotted versus the curve number were binned in following manner: the average rupture force or length values of 10 force extension curves were

determined in Igor 6.0 and plotted as bars in the corresponding graph. The resulting standard deviation of one binning interval can be found in the corresponding roburo- or longitudogram as error bar. This explains the occurrence of low forces in the range of 0 to 5 pN: if only one rupture event with a last rupture force of 10 pN was monitored over 10 force curves, the resulting average force appears to be 1 pN in the binning interval of the roburogram. The WLC-fit according to Bustamante et al. in Fig. 4b was accomplished in Igor 6.0 with a persistence length of 50 nm in agreement with literature values.<sup>1,2</sup> Finally, we performed control experiments without DNA and measured no interaction.

## Rupture length distributions for the OH-SAM and NH<sub>2</sub>-SAM electrode

Here we present the corresponding rupture length distributions for the OH-SAM and NH<sub>2</sub>-SAM electrode. For the OH-SAM electrode, the corresponding rupture length distribution shows constant maximum rupture lengths of about 800 nm at +0.5 V at pH 8.5 (Fig. S1a). This consistent maximum length indicates the long-term stability of the tip functionalization. Similarly at pH 5, a rupture length maximum of 150 nm at +0.5 V was detected. For the deprotonated NH<sub>2</sub>-electrode at pH 11, a constant rupture length of 1,000 nm was measured. This may be related to the high non-coulombic force in this system. However, the rupture lengths decrease at the minimum potentials around -0.5 V. In case of a protonated NH<sub>3</sub><sup>+</sup>-electrode, an electric control could not be identified in accordance with Fig. 2e. However, a global decrease of the rupture lengths can be seen due to melting and rupture events at forces around 300 pN. Control experiments showed that a long ssDNA strand on cantilever seems to crumple up and adsorbs on the AFM tip surface rather than scanning the space around the tip.

In general, the reduced adhesion length at lower potentials than +0.5 V can be described by a differential adhesion model since the dsDNA is able to adsorb on the charged electrode as well as on the AFM tip surface itself.<sup>3</sup> If the ad-/desorption force is decreased on the SAM electrode relative to the AFM tip surface, shorter rupture lengths are expected. As the AFM tip surface becomes then energetically more favourable for a dsDNA molecule, only shorter polymer segments adsorb on the electrode surface: the DNA in the gap between tip and electrode is free to choose between both surfaces, it will entirely adhere to the preferred surface. Only if the DNA is covalently attached to the surface with the lower adhesion force (in our case the tip), will the DNA bridge between both surfaces. The measured force is the adhesion force between DNA and, in our case, the electrode. The magnitude of this force is then in a good approximation independent of the tip DNA interaction. Not so the bridging length. If both adhesion forces become comparable, the DNA fluctuates between both surfaces, and the effective DNA length may be greatly reduced.

This feature can be seen in detail in the corresponding longitudograms (longitudo is the Latin word for length). Similar to Fig. 3, the rupture lengths plotted versus the corresponding potentials exhibited the same behaviour as the rupture forces with a maximum rupture length of  $764 \pm 27$  nm (pH 8.5, Fig. S2a) and  $142 \pm 13$  nm (pH 5, Fig. S2b) at +0.5 V for the OH-SAM electrode. With respect to the NH-SAM electrode, the rupture length decrease at -0.4 V can be seen in Fig. S2c.



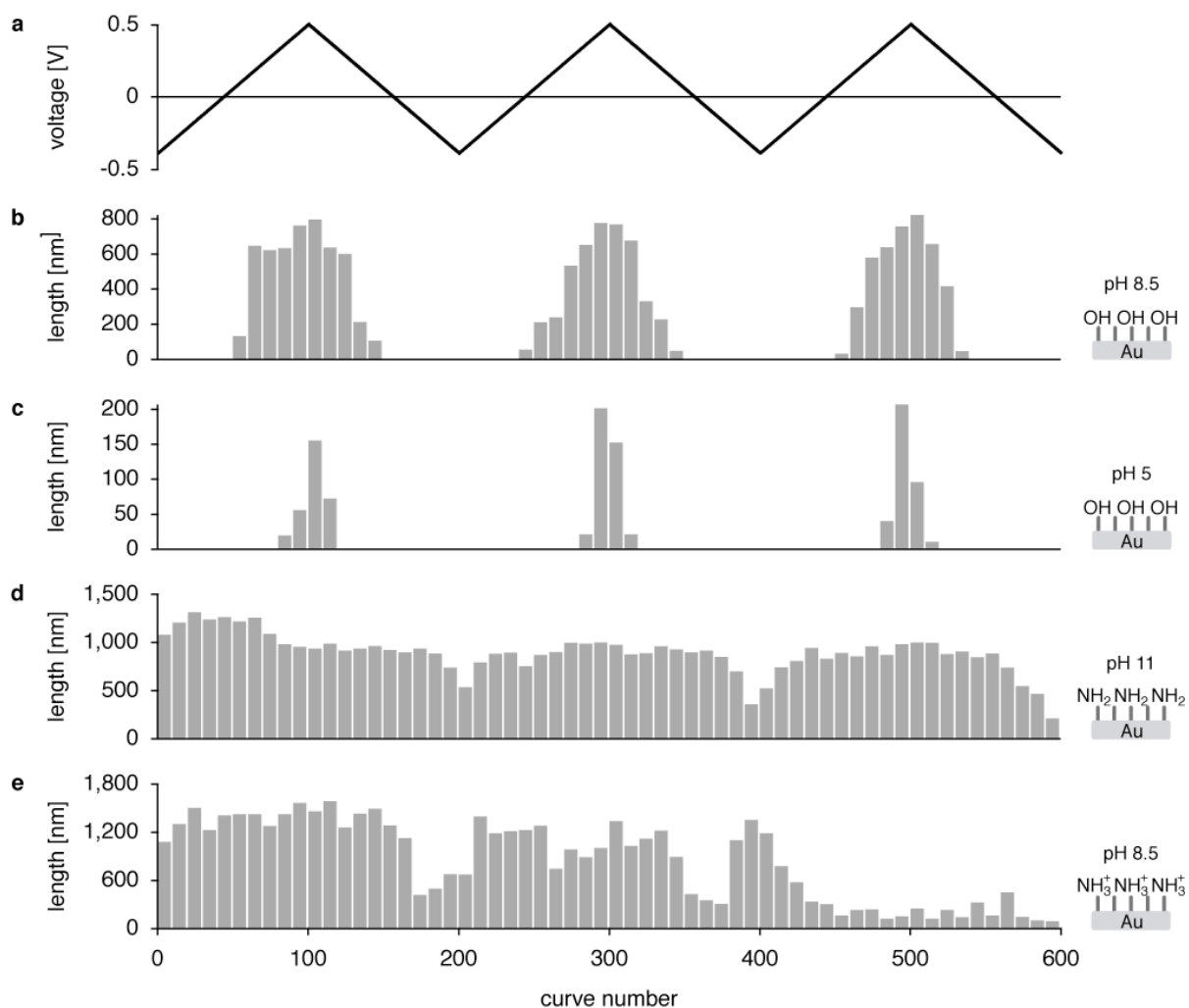


**Figure S1. Cyclic change of the surface potential of the OH-SAM and NH<sub>2</sub>-SAM electrode: rupture lengths of dsDNA vs. curve number.** **a**, The potential between the SAM functionalized electrode (working electrode) and an Ag/AgCl reference electrode was linearly ramped between -0.4 V and 0.5 V and plotted versus the curve number. The potential was changed by 10 mV per curve number; the electrolyte contained 100 μM MgCl<sub>2</sub> at various pH-values. A platinum counter electrode completed the three-electrode setup. **b**, At pH 8.5, the resulting rupture length distribution for the OH-SAM electrode showed well defined and symmetrical length peaks in the positive range around +0.5 V with a constant length maximum of about 800 nm. **c**, The same experiment at pH 5 revealed rupture lengths around 150 nm only at +0.5V. **d**, The amino groups of the NH<sub>2</sub>-SAM electrode were uncharged at pH 11. The measured rupture lengths stay basically constant at 1,000 nm but decrease at the minimum potentials of -0.5 V. **e**, At pH 8.5, the measured rupture lengths continuously decrease due to melting and rupture events at forces around 300 pN. As ssDNA is expected to adsorb on the AFM tip surface, only the dsDNA molecules, which were attached at higher AFM-tip positions, can adsorb on the NH<sub>3</sub><sup>+</sup>-SAM. For this reason, the measured rupture lengths decrease and vanish, if all dsDNA are melted after 600 force-extension curves.

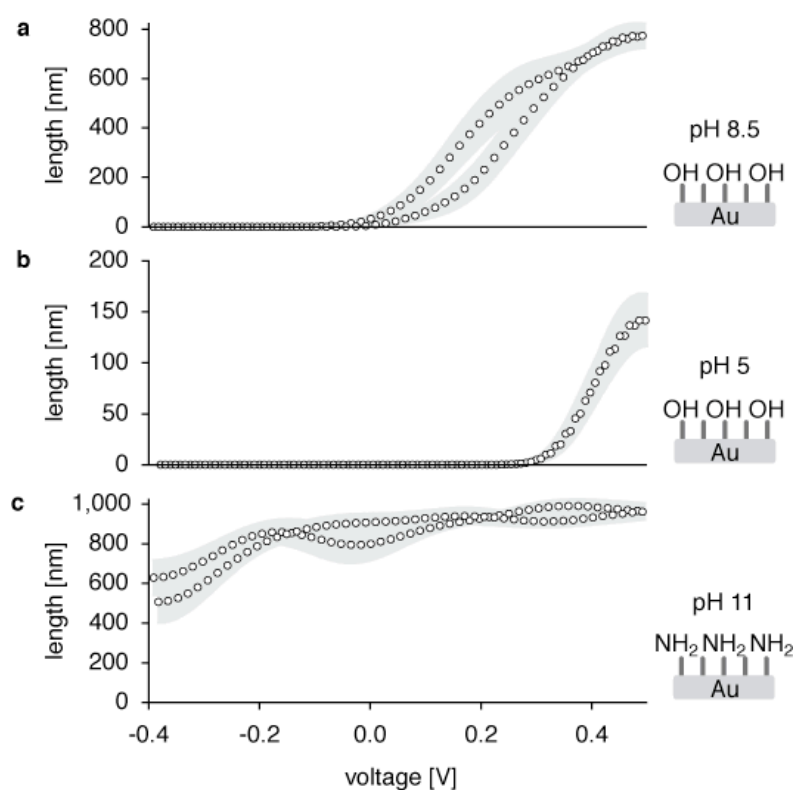


**Figure S2. Longitudograms of dsDNA on the OH-SAM and NH<sub>2</sub>-SAM electrode: rupture length vs. applied potential.** **a**, Plotting and smoothing the averaged rupture length (longitudo means length in Latin) of the three cycles from Fig. S2a versus the corresponding potentials yielded an monotonic increase of the rupture force up to  $764 \pm 27$  nm at +0.5 V. The approximately linear decrease of the rupture length in the cathodic direction was slightly faster as no rupture events were detected below  $0.0 \pm 0.04$  V (lower curve). **b**, The analogue experiment at pH 5 showed a rupture length increase up to  $142 \pm 13$  nm. **c**, The longitudogram for the uncharged NH<sub>2</sub>-SAM electrode discloses an decrease of the rupture length at -0.4 V. In all plots, circles indicate the mean of a binning interval, grey errors bars represent the standard error of the mean.

## Calculation of the diffuse layer potential and surface charge

According to the model proposed by Rentsch et al.<sup>4</sup>, the diffuse layer potential was calculated numerically by equations (E1) and (E2), the corresponding diffuse layer charge according to equation (E3):

$$\psi_D(\phi) = \frac{C_L}{C_L + C_D(\psi_D)} (\phi - \phi_{pzc}) \quad (\text{E1})$$

$$C_D(\psi_D) = \left( \frac{2z^2 e^2 \epsilon \epsilon_0 n^0}{k_B T} \right)^{1/2} \cosh\left( \frac{ze\psi_D}{2k_B T} \right) \quad (\text{E2})$$

$$\sigma = -\sigma_D(\psi_D) = \left( 8k_B T \epsilon \epsilon_0 n^0 \right)^{1/2} \sinh\left( \frac{ze\psi_D}{2k_B T} \right) \quad (\text{E3})$$

Thereby, the concentration is 100  $\mu\text{M}$   $\text{MgCl}_2$  and the literature value  $C_L = 0.8 \mu\text{F}/\text{cm}^2$  and  $\phi_{pzc} = -0.045 \text{ V}$  vs.  $\text{Ag}/\text{AgCl}$  for the  $\text{SH}-((\text{CH}_2)_{11})\text{-OH}$  self assembled monolayer was used.<sup>4</sup> Moreover, in a first approximation, the valency values of the counterions are  $z = 1$  for applied positive potentials and  $z = 2$  for applied negative potentials.<sup>5,6</sup>

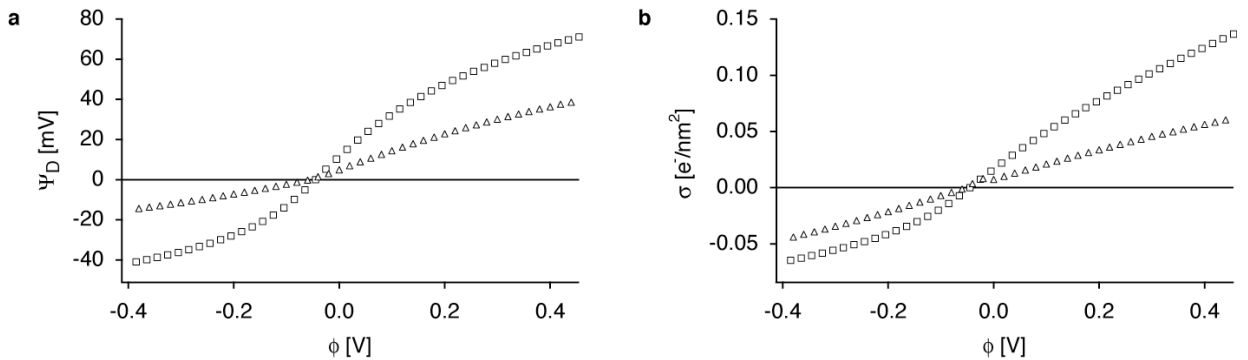


**Figure S3. Calculated diffuse layer quantities.** Squares mark the OH-SAM quantities, triangles the NH<sub>2</sub>-SAM quantities. **a**, Applying a potential of 0.455 V yields only a potential of 70 mV for the diffuse layer potential on a OH-SAM and 40 mV on an NH<sub>2</sub>-SAM. **b**, The corresponding charge densities on the surface yields 0.15 or 0.006 positive charges per  $\text{nm}^2$ , respectively.

As is it can be seen in Fig. S3 (squares), the potential drop between the gold electrode and the  $\text{SH}-((\text{CH}_2)_{11})\text{-OH}$  self assembled monolayer is so drastic that only 15% of the applied potentials builds up the diffuse double layer. The resulting positive surface charge density is then around  $0.15 e^-/\text{nm}^2$  for  $\phi = +0.5 \text{ V}$ . The surface charge values  $\sigma_0$  are relevant for the calculation of the desorption force  $F_c = 4\pi l_b k_B T \kappa^{-1} \tau \cdot \sigma_0$  as described.<sup>7</sup>

With regard to the SH-((CH<sub>2</sub>))<sub>11</sub>-NH<sub>2</sub> self assembled monolayer, the potential drop is even higher as it can be seen in Fig. S3a (triangles): the output diffuse layer potential is in the range of 8% of the applied potential. The corresponding charge density is then 0.006 e<sup>-</sup>/nm<sup>2</sup> for  $\phi = +0.5$  V. From the roburogram in Fig. 3c, a capacitance of  $C_L = 0.25$   $\mu\text{F}/\text{cm}^2$  was determined for the deprotonated NH<sub>2</sub>-SAM electrode, whereby the remaining parameters were not changed. Analogously, a potential of zero charge of  $\phi_{\text{pzc}} = -0.045$  V was assumed because of the symmetrical force in/decrease around 0 V.

## Lateral mobility of dsDNA on the OH-SAM

In order to exclude pinning effects, which might cause the force increase at the end of the discussed force extension curves, the lateral mobility of dsDNA on the OH-SAM was confirmed by the following experiment:<sup>8</sup> the cantilever was not only retracted vertically, but also at different pulling angles  $\Omega$  with respect to the surface. Thereby, the rupture forces and lengths were measured. If an adsorbed dsDNA molecule was pinned at surface and was not able to follow the horizontal movement of the cantilever, the measured rupture lengths would decrease with a factor of  $\cos(\Omega)$ . On the other hand, if the dsDNA is laterally mobile and may follow the cantilever movement, an equilibrium polymer angle  $\Phi$  is established and the rupture lengths do not decrease with a factor of  $\cos(\Omega)$ .

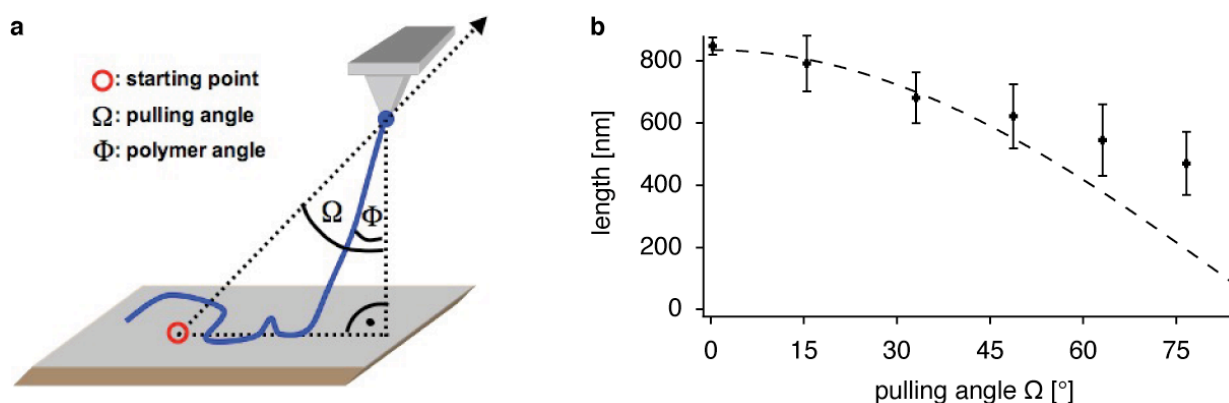


**Figure S4. Mobility of dsDNA on the OH-SAM.** **a**, Scheme of the experimental procedure: the cantilever is retracted at an angle  $\Omega$  from its starting point. Dependent on the rearrangement possibilities of the polymer, the polymer can follow the AFM tip and maximize its binding energy to the surface. However the polymer angle  $\Phi$  stays constant, if the friction of the adsorbed part equals the tangential desorption force. **b**, The deviation of the rupture length from the cosine (dashed line) for higher pulling angles indicates a sliding of the dsDNA on the OH-SAM. Error bars represent the s.e.m.

This process depends also on the friction coefficient between the molecule and the surface. If friction is negligible, the rupture lengths stay constant. But in case of measurable friction, the rupture lengths decrease similar to Fig. S4b. Here, the friction coefficient between a single dsDNA molecule and the OH-SAM at +0.5V is determined to be  $\zeta \approx (1.4 \pm 0.3) \cdot 10^{-6}$  Ns/m with an adsorbed minimum length of  $l_{\min} = 2.9$  nm as discussed in the paper and a total retract speed of  $v = 1500$  nm/s.

## Voltammograms of the OH-SAM electrode

The cyclic voltammograms for electrode cleaning as described in the methods section guaranteed an insulating OH-SAM coverage, as redox-peaks were absent in the applied voltage range (Fig. S5a). Likewise, the cyclic staircase voltammograms, which were recorded during the force spectroscopy experiments, confirmed the stable coverage of a large number of potential cycles (Fig. S5b).

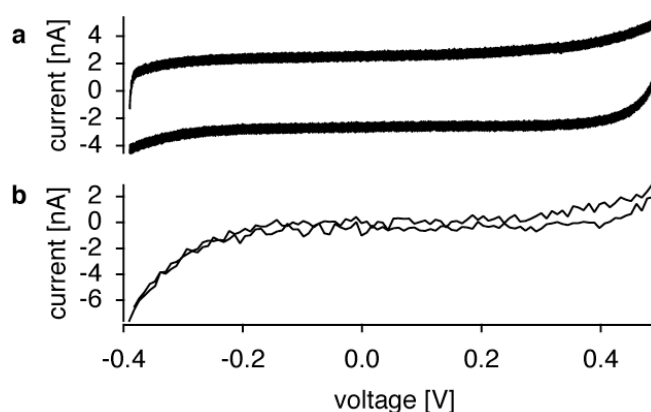


**Figure S5. Voltammograms of the OH-SAM electrode.** **a**, Before the AFM experiment, 20 cleaning voltammograms in the range of from -0.4 to 0.5 V were recorded with a sweep rate of 0.1 V/s. **b**, The resolution of the cyclic staircase voltammograms is decreased as only one measurement point per force curve was recorded. However, the stable coverage by the OH-SAM was confirmed, as redox-peaks were absent throughout the AFM-experiment.

In general, charging of the electrodes and the leak current through inhomogeneities of the SAM contribute to the measured current. The hysteresis in Fig. S5a is attributed to the fast, linear voltage sweep (0.1 V/s): here, currents to charge the double layer capacity are dominating.<sup>9</sup> In contrast, the current in the AFM experiment was measured only after the 10 mV potential change in steps of 4.5s (Fig. S5b). Consequently, the quasi-DC current through the resistance of the SAM covered electrode and the solution is measured. The slight increase at both voltage extremes in Fig. S5 mark the beginning of oxidation/reduction of the SAM electrode.<sup>9</sup> Nevertheless, the long-term stability of the SAM was confirmed, as no oxidation/reduction peaks were monitored over several cycles in an AFM experiment.

## Thermal stability of dsDNA

In order to prove the thermal stability of the 4.9 kbp dsDNA in 100  $\mu\text{M}$   $\text{MgCl}_2$  at room temperature, a temperature dependent UV absorption measurement was performed.<sup>10</sup> Thermal denaturation is measured at a melting temperature of 84.3  $^\circ\text{C}$ . Consequently, the dsDNA is thermally stable under experimental conditions.

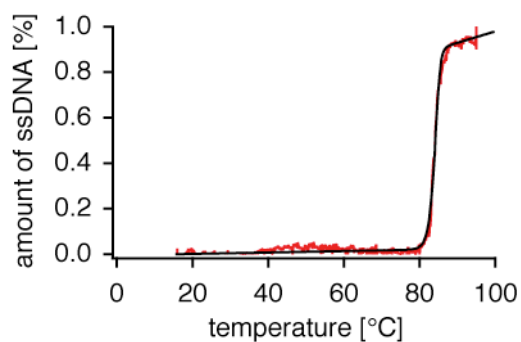


**Figure S6. Melting curve of 4.9 kbp DNA.** The amount of ssDNA was determined by UV absorption over a temperature range from 16 – 95  $^\circ\text{C}$  (red curve). The theoretical fit (black curve) delivers a melting temperature of 84.3  $^\circ\text{C}$ . This demonstrates the high thermal stability of dsDNA in a 100  $\mu\text{M}$   $\text{MgCl}_2$  solution.

## References

1. Bustamante, C., Marko, J.F., Siggia, E.D. & Smith, S. Entropic Elasticity of Lambda-Phage DNA. *Science* **265**, 1599-1600 (1994).
2. Marko, J.F. & Siggia, E.D. Stretching DNA. *Macromolecules* **28**, 8759-8770 (1995).
3. Sonnenberg, L., Parvole, J., Kuhner, F., Billon, L. & Gaub, H.E. Choose sides: Differential polymer adhesion. *Langmuir* **23**, 6660-6666 (2007).
4. Rentsch, S., Siegenthaler, H. & Papastavrou, G. Diffuse layer properties of thiol-modified gold electrodes probed by direct force measurements. *Langmuir* **23**, 9083-9091 (2007).
5. Chen, Z. & Singh, R.K. General solution for Poisson-Boltzmann equation in semiinfinite planar symmetry. *Journal of Colloid and Interface Science* **245**, 301-306 (2002).
6. Ross, S. & Morrison, I.D. *Colloidal Systems and Interfaces*, (Wiley & Sons, New York, 1988).
7. Seitz, M., Friedsam, C., Jostl, W., Hugel, T. & Gaub, H.E. Probing solid surfaces with single polymers. *Chemphyschem* **4**, 986-990 (2003).
8. Kuhner, F. et al. Friction of single polymers at surfaces. *Langmuir* **22**, 11180-11186 (2006).
9. Florin, E.L. & Gaub, H.E. Painted Supported Lipid-Membranes. *Biophysical Journal* **64**, 375-383 (1993).
10. Breslauer, K.J., Frank, R., Blocker, H. & Marky, L.A. Predicting DNA Duplex Stability from the Base Sequence. *Proceedings of the National Academy of Sciences of the United States of America* **83**, 3746-3750 (1986).



# 5 Bonding DNA to gold

While in the last chapter the coulombic adhesion of dsDNA on a SAM insulated gold electrode was presented, this subsequent chapter will describe the electrical induced bonding or "electrosorption" of single dsDNA molecules to a bare gold electrode. Electrochemistry and AFM based single molecule force spectroscopy were therefore combined to characterize the interaction between dsDNA and gold. With this combination of techniques, it was possible to control electrically the formation of coordinate N-Au bonds between a single dsDNA molecule and the gold substrate.

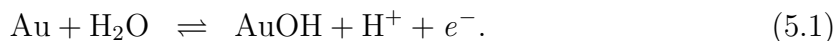
## 5.1 Electrochemistry of the gold surface

By omitting the insulating self assembled monolayer (SAM), charge transfer across the gold-solution interface is possible and leads to a complex interplay between salt adsorption, pH-value change, surface oxidation/reduction and the applied potential. These relationships are briefly explained to enable a clear description of the dsDNA-gold interaction in the next section.

### Cyclic voltammetry

Cyclic voltammetry is the established electrochemical technique to characterize the oxidation and reduction potentials of species in the solution or the electrodes themselves [42]. Thereby, the potential of a working electrode is linearly ramped versus time between two potential limits and the current is recorded for both scanning directions. Plotting current versus voltage reveals current peaks, which are related to the corresponding oxidation/reduction potential of the analyte.

In case of a polycrystalline gold electrode, the potential dependent charge transfer is responsible for the oxidation and the reduction of the gold atoms. This elementary act can be described by



It has to be noted that this equation is only a generalization of several processes comprising surface rearrangement and formation of OH lattices [52, 53]. A representative voltammogram of the gold electrode is depicted in Figure 5.2 D, red curve; the main oxidation peaks are marked as O1 and O2, the main reduction peaks as R1 and R2. Increasing the potential from -1 V to +1 V with a sweep rate of 0.1 V/s in the anodic direction oxidizes the gold surface (formation of an AuOH layer). In contrast, the surface is reduced (R1 and R2), when the scan direction is inverted in the cathodic direction. Here, the oxide layer is electrochemically removed. The solution in

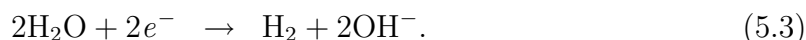
the experiments contained 50  $\mu\text{M}$   $\text{MgCl}_2$  and no other analytes (buffering agents etc.). Therefore, oxidation/reduction peaks for  $\text{MgCl}_2$  are absent as the necessary potentials [42] are beyond  $\pm 1$  V.

### Hydrolysis of water and pH-shift

As the used solution was unbuffered (to reduce cantilever bimetal artefacts caused by buffering agent currents), the hydrolysis of water changed the pH-value in the micro-environment around the electrode. For a positively charged electrode (anode), the pH-value is lowered by



In contrast, potentials below -0.7 V [54] increase the pH-value around the negatively charged electrode (cathode) by



The effect of pH-change was used to trigger the formation of an N-Au bond as discussed further below.

### Surface charge and ion adsorption

The applied electronic potential  $\phi$  leads to the formation or destruction of the oxide layer. However, the hydroxyl groups may as well be protonated or deprotonated ( $\text{AuOH}_2^+$ ,  $\text{AuO}^-$ ) due to the pH-value. This protonic surface charge density  $\sigma^p$  determines together with the applied electronic charge density  $\sigma^e$  the charge density of the diffuse ion layer  $\sigma^d$  in solution. Electroneutrality is demanded between these three charge densities [55, 56, 57]:

$$\sigma^e + \sigma^p + \sigma^d = 0. \quad (5.4)$$

From this equation results a transcendental expression for the diffuse layer potential  $\psi_D$  depending on the applied potential  $\phi$ , which can be solved analytically. Thereby, the salt concentration, pH-value of the solution is considered as well. Being able to calculate  $\psi_D(\phi)$  permits to estimate the amount of ions by Langmuir adsorption isotherms, which are attracted by the charged electrode (ions in solution are affected by the diffuse layer potential). The density of adsorbed ions determines as well the dsDNA-gold interaction. The detailed formalism and calculation are given in the supplement of the attached publication.

To sum up, the discussed electrochemical relationships are crucial for the understanding of the electrical DNA bonding to a gold surface in the following section.

## 5.2 Electrochemical induced DNA-gold bonding

### Catching DNA

Equally to the previous study in chapter 4, the 4.9 kbp dsDNA was covalently attached with one strand to the AFM tip. In order to qualitatively characterize the interaction between the dsDNA and the gold electrode, a new measurement protocol was employed. The dsDNA functionalized AFM tip approached the gold electrode, whose surface potential was adjusted to 0 V. No measurable interaction was recorded neither upon approach nor retraction. The tip was then kept 200 nm above the surface while the

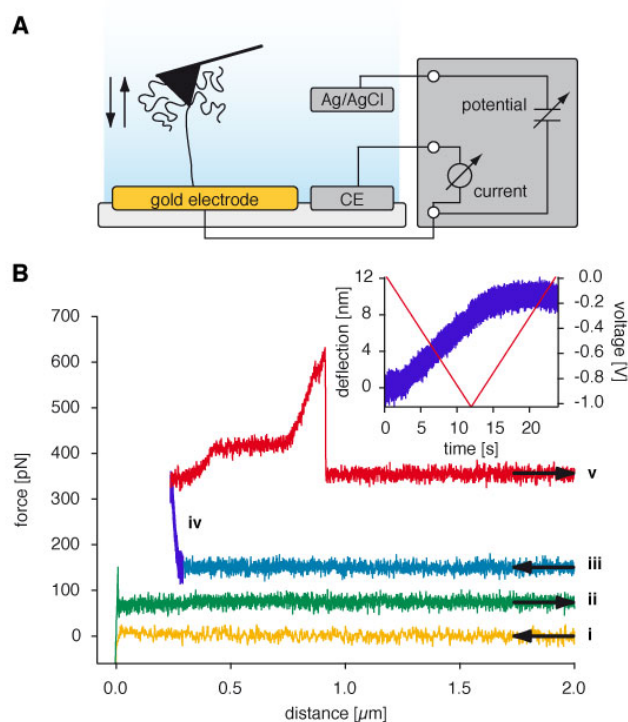


**Figure 5.1** (A) Schematic representation of the single molecule force spectroscopy experiments on a polarized gold electrode. 4.9 kbp dsDNA was covalently bound to an AFM tip and brought into contact with a bare gold microelectrode submerged in a 50  $\mu\text{M}$   $\text{MgCl}_2$  solution at pH 8.5. The surface potential of the gold electrode versus an Ag/AgCl reference electrode was controlled by a potentiostat through a platinum counter electrode (CE). (B) Electro-sorption of a dsDNA molecule. At zero potential, the AFM tip was brought into contact with the surface and was retracted (i, ii). Then the tip approached the surface again, and kept 200 nm above the surface (iii) while the potential was changed from 0 V to -1 V and back to 0 V with a sweep rate of 85 mV/s (iv) Finally, the tip was retracted completely and the stretching of a single dsDNA molecule followed by the characteristic plateau of the BS transition, the melting of the DNA and finally the complete detachment of the DNA could be monitored (v). The insert shows the drift and the crosstalk of the potential sweep into the deflection signal caused by the polarization currents. It corroborates that the tip and gold surface were not in contact while the DNA was "electrosorbed" to the surface.

potential was ramped to -1 V and back to 0 V. During this potential sweep a single dsDNA was "electrosorbed": upon retracting the tip, a force extension trace with all of the typical features of a single dsB-DNA was recorded (entropic elasticity stretching followed by the so-called BS plateau at 65 pN [45, 58, 59]). At the end of the unbinding transition at roughly 180 pN the two strands are already separated. The further increase up to 250 pN indicates that the same strand, which was covalently attached to the tip, had established a stable bond with the gold surface during the potential sweep. Furthermore, an electrostatic interaction between dsDNA and gold can be excluded, as the start and end potential were 0 V. This potential proved to trigger no electrosorption in the first force extension curve (i, ii). Finally, a desorption plateau was not monitored, which indicates a point-like interaction of the DNA with the gold surface.

### Electrochemistry of DNA gold bonding

To probe at which potential this electrically induced attachment had occurred, the same single molecule force spectroscopy scans, while ramping the surface potential in 10 mV steps, were performed as in the previous chapter (Figure 5.2). The most remarkable and at first absolutely counterintuitive feature seen in Figure 5.2 B is the asymmetric distribution of rupture forces at negative potentials. The magnitude of rupture forces was persistent over several cycles, but the number of interacting molecules constantly decreased (Figure 5.2 C). This indicates the continuous separation of dsDNA molecules upon retraction during the experiment as shown in Figure 5.1. However, the question remains, why the negatively charged dsDNA interacts exclusively at negative potentials with the gold electrode and is not repelled.

The first part of the puzzle could be solved by directly comparing the cycling voltammogram of the gold electrode with the potential dependent rupture forces (we named these force vs. potential plots roburograms as *robur* means force in Latin): obviously, dsDNA-gold bonding was only possible as soon as the gold surface was reduced within the peaks from R2 to O1, which mark the border of measurable interaction (Figure 5.2 D).

Due to the negative surface potentials while scanning the potential from R2 to O1,  $\text{Mg}^{2+}$  ions were adsorbed as discussed in section 5.1. A detailed estimation for the  $\text{Mg}^{2+}$  ion density on the gold surface is given in the Supporting Material of the attached publication. Furthermore, when the gold-coated tip touched the gold surface, the electrical contact (contact resistance of 40  $\Omega$ ) short circuits the electric field in the contact zone, and the positive charge of the magnesium ions attracts the DNA to the gold electrode. The measurement of the contact resistance is described in detail in section B.2. As an increasing number of  $\text{Mg}^{2+}$  ions were attracted due to the negative potentials, the attraction and likelihood to form multiple bonds were increased as well. For this reason, the rupture forces increased as well until surface oxidation set in, which rendered the electrode non-reactive again.

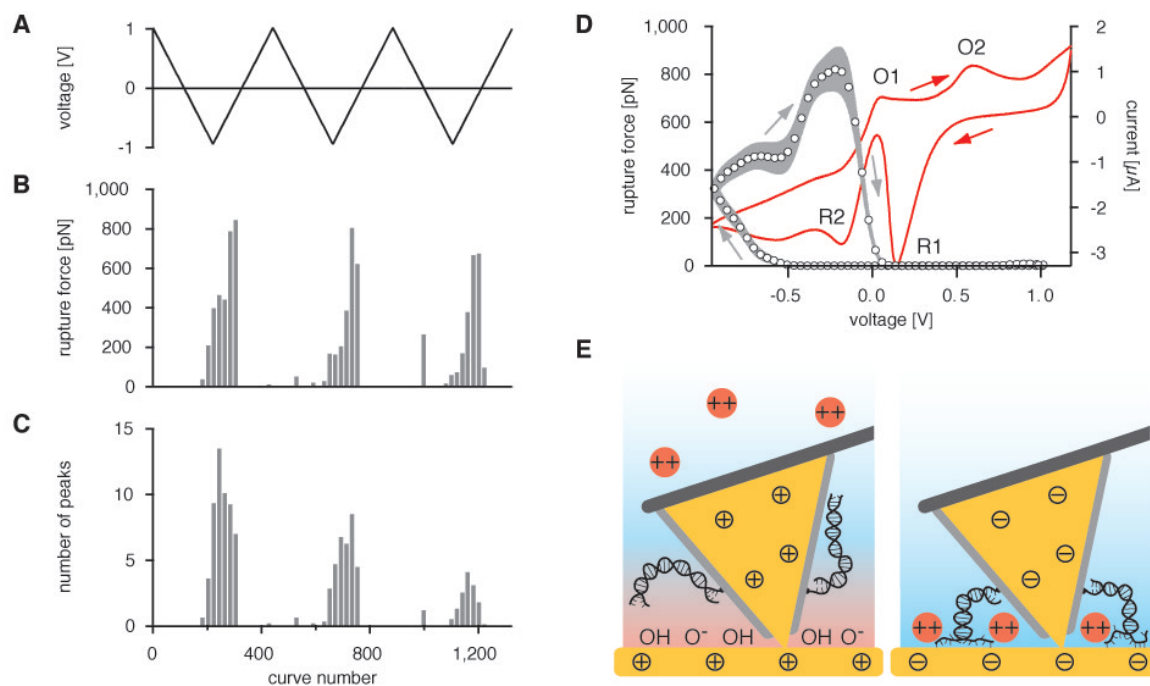


**Figure 5.2** Electrochemistry of DNA-gold bonding. **(A)** As in classic cyclic voltammetry, the potential of the gold electrode was ramped between -1.0 and 1.0 V in 10 mV steps. In between the steps, a force curve was recorded. **(B)** The magnitude of the last step in the force curve, resulting from a single molecule detachment and **(C)** the overall number of rupture peaks throughout the force curve, reflecting the number of bound molecules were extracted. dsDNA was bound to the bare gold electrode at high negative potential values around -1 V, and the resulting rupture forces with a marked hysteresis were in the range up to 800 pN. However, a global decrease in the number of bound molecules could be observed. **(D)** Direct comparison of the binned and smoothed rupture forces (circles, grey error bars indicate the interpolated standard error of the mean) and the polarization current (red) plotted in a cyclic voltammogram (recorded at 100 mV/sec). Indicated are the well-known oxidation and reduction peaks of the gold surface. **(E)** Schematics of the molecular arrangement.

## Determination of the reactive species

As the electrochemical conditions for dsDNA-gold bonding could be characterized, the "sticky part" of the dsDNA had to be determined. One result from Figure 5.1 was that the influence of the backbone of the dsDNA was negligible as desorption plateaus were not observed. Furthermore, the ends of a dsDNA are known to be not closed but tend to open up along several base pairs in a highly dynamic manner [60, 61]. Thus, the bases may come into contact with the gold electrode. The main difference between adenine, cytosine, guanine and thymine is the missing primary amino group for thymine. Consequently, the end sequence of the dsDNA, which interacted with the gold surface, was programmed to investigate the bond formation in detail (Figure 5.3). The formation of coordinate nitrogen-gold bonds is well characterized in experimental and theoretical studies [62, 63, 64, 65]. In general, nitrogen offers a lone electron pair to a undercoordinated gold (ad)atom to form a N-Au bond.

Basically two stretching conformations are possible, as the dsDNA was covalently attached only with one strand to the AFM tip: first, the other end of this strand binds to the gold surface, compare Figure 5.3 A upper row. When the dsDNA is then stretched, the coordinate bond is expected to rupture at elevated forces. The counter strand will remain at least loosely attached, so that in a repeated force extension curve, the coordinate bond can be formed again. Second, the counter strand chemisorbs to the gold surface, compare Figure 5.3 A lower row. Here, both strands are separated upon retraction before the coordinate bond ruptures. As single stranded dsDNA is known to interact strongly with the gold surface [66, 67], a new coordinate bond formation in a repeated experiment is not possible. The decreasing number of interacting molecules can then be easily measured.

The main results can be identified in Figure 5.3 C. For a detailed discussion and comparison, please refer to the Supporting Material of the attached publication. TA-dsDNA had the longest lifetimes, as in this case predominantly the strand being attached to the tip was bound to the surface. In contrast, if the counter strand exhibited primary amino groups, a rapid wear out of the AFM tip was observed due to strand separation. These results clearly show that the primary amines on the bases at the end of the dsDNA bind to the gold surface.

At this point, the influence of the pH-value can be understood: primary amino groups exhibit a  $pK_a \approx 9$  and the experiments were conducted at pH 8.5. Water hydrolysis increases the pH at low potentials around -1 V, hence most of the primary amino groups are uncharged due to proton dissociation and exhibit a lone electron pair ( $-NH_2$ ), which is needed for coordinate bonding. Starting the experiment at a higher pH 10 revealed interactions, as soon as the gold surface was reduced, see Supporting Material of the attached publication. In contrast, high potentials around +1 V lowered the pH-value, so most of the primary amino groups are charged due to proton association ( $-NH_3^+$ ) and could not offer a lone electron pair to the gold surface. This was also shown by experiments at pH 6, where no interaction at all was observed. Here, the applied potential could not increase the pH over three orders of magnitude to deprotonate the primary amino groups. To sum up, the pH-value is also an important parameter for the electrical triggered bond formation.

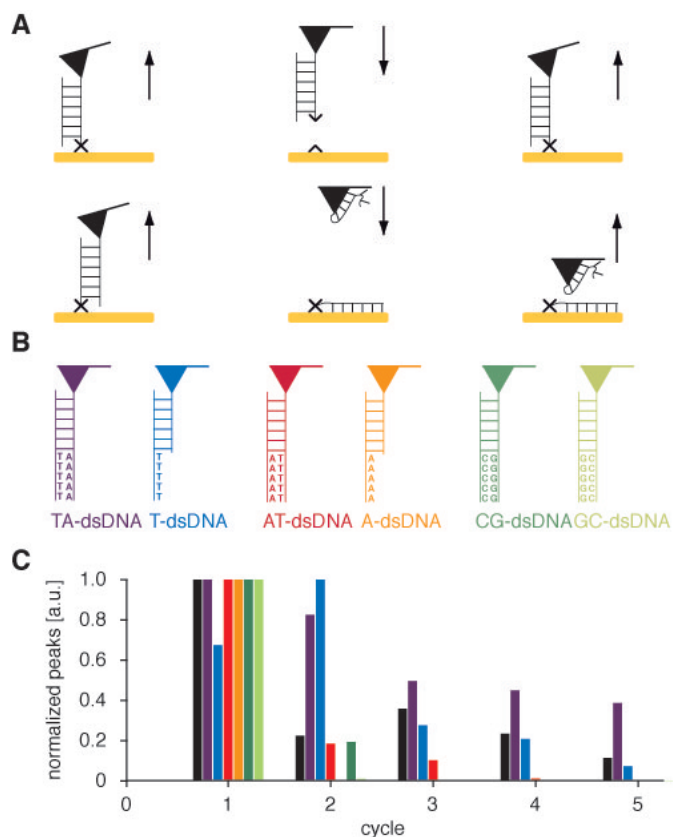


**Figure 5.3** Nucleotide specificity of DNA-gold electrodesorption. **(A)** Schematics of strand separation and bond rupture of dsDNA under force. One strand is covalently attached to the tip, and either the same (upper row) or the counter strand (lower row) is electrodesorbed to the gold surface. If the covalent bonds in the attachment and the DNA backbone are stronger than the coordinative bond, the latter will rupture with higher probability and repetitive electrodesorption is possible. If the counter strand is chemisorbed, both strands will unbind. Single stranded DNA is known to strongly interact with the gold surface and chances for re-hybridization are strongly reduced. **(B)** In addition to the heterogeneous dsDNA shown in Figure 5.2, the depicted six dsDNA molecules with five homogenous base pairs at the end or five overhang bases were tested. Thereby, the dsDNA was always covalently attached with one single strand to the AFM tip. **(C)** As a relative measure for the wear out of the tip, the number of rupture peaks for one potential cycle were summed and normalized. The heterogeneous dsDNA, TA-dsDNA and T-dsDNA (black and blue curves) could be desorbed over the five cycles, whereby the TA-dsDNA was the most stable construct. With AT-, A-, CG- and GC-dsDNA, the interaction ceased rapidly, indicating that those dsDNA molecules were separated when stretched. As only thymine exhibits no primary amino group, this result strikingly corroborates our previous assumption that chemisorption of DNA to gold occurs via the primary amino groups on the bases.

## Quantifying the bond strength

The last experiments qualitatively proved the formation of coordinate N-Au bonds between dsDNA and gold. The measured wide spread of rupture forces indicated the formation of multiple bonds. Therefore only a single adenine was attached via a polyethylene glycol spacer (PEG) to the AFM tip. The force extension curves revealed clear single molecule stretching signatures and mean forces of  $170 \pm 50$  pN. The forces varied less than 15 pN for different applied potentials, so the N-Au bond strength itself proved to be virtually potential independent. The broad distribution is contributed to the rough and heterogeneous gold surface at the atomic level. With typical energies reported for the Au-N-bond of 32 – 42 kJ/mol and estimated bond lengths of 0.3 nm one would expect a barrier force of 185 pN as a realistic estimate [68, 69]. These results indicate that the rupture of the coordinate bond is largely potential independent and that the higher rupture forces found in the DNA experiments stem from multiples bases electrosorbed to the gold surface. For a thymine functionalized AFM tip, no specific interaction was measured at all.

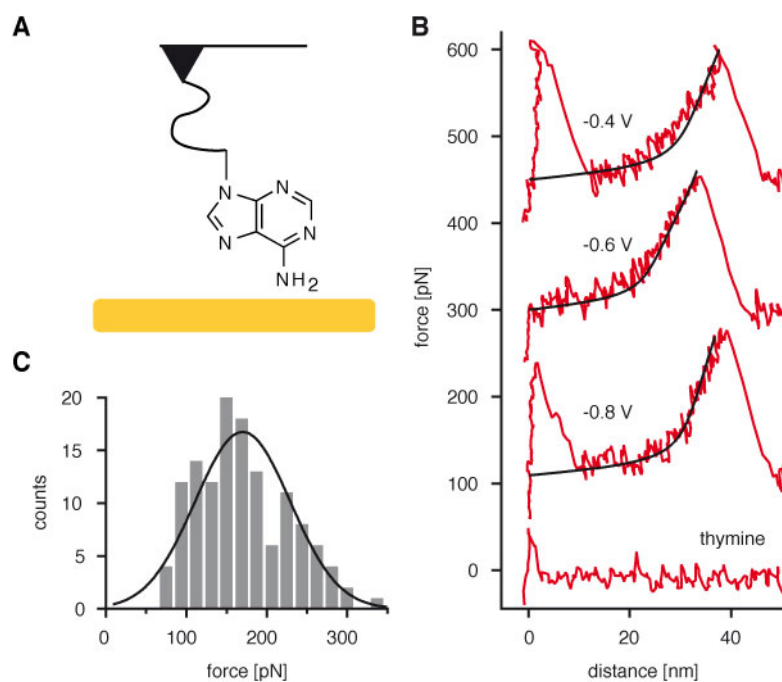


**Figure 5.4** Coordination bond rupture of individual nucleotides. **(A)** A single nucleotide was attached to a 10 kD PEG spacer molecule, which itself was covalently bound to the AFM tip. **(B)** Typical examples of force extension curves, with adenosine (upper trace) and thymidine (lower trace) as the nucleotides were recorded at constant potentials ranging from -0.4 V and to -0.7 to -1 V. No measurable interaction could be observed for the thymine PEG whereas for adenosine, the stretching of the PEG spacer (two-state FJC fit, black curve) and the rupture of the N-Au bond in the range of 180 pN could be repeatedly observed. No marked difference was found between the three different potentials. **(C)** The corresponding histogram of 135 force-extension curves delivers an average rupture force of  $170 \pm 50$  pN.



The understanding and the control of the complex interplay between salt, pH-value and applied potential enabled an individual electrosorption of dsDNA at their ends to defined positions on the gold surface. Thereby, primary amino groups of the nucleotides formed coordinate bonds with gold (ad)atoms. The N-Au bond strength was determined in experiments with single nucleotides and is in very close agreement with model calculations. Moreover, the induced chemisorption of single molecules, which could be demonstrated for the first time, provides a broad range of new experiments and theoretical studies. Thus, the combination of single molecule force spectroscopy and electrochemistry will lead to a multitude of new applications such as "electric glue".

# Bonding DNA to Gold

M. Erdmann<sup>1</sup>, R. David<sup>1,2</sup>, A. R. Fornof<sup>1</sup>, H. E. Gaub<sup>1</sup>

Being able to locally deliver and electrically control the chemisorption of individual molecules opens the door to a richness of novel applications. We directed individual DNA strands with an AFM tip to a chosen position and bonded them electrically to a gold surface. By single molecule force spectroscopy we investigated the interaction of dsDNA with the gold electrode while cycling the potential. We found that B-DNA chemisorbs to the gold electrode exclusively at the ends, and we identified the electrochemical parameters required for bond formation. By varying the sequence of the nucleotides at the free ends we identified the coordinate N-Au bonds between the primary amines of the bases and the gold surface as the dominating interaction. We corroborated this finding in force spectroscopy experiments where only a single adenosine nucleotide on a PEG spacer was “electrosorbed” to the gold electrode, resulting in a binding force of 170 pN, which is in perfect agreement with model calculations.

The introduction of single molecule cut and paste technology opened the door to a richness of novel applications (1-3). SMC&P combines the precision of the AFM with the selectivity of DNA hybridisation to pick up individual molecules and to deliver them in a target zone. While in SMC&P a passive hierarchy of interaction forces between different DNA strands dictates whether or not a molecule is delivered, it would be

highly desirable to covalently attach the delivered molecule to the target triggered by an external parameter, for example, electrically. Many other applications are conceivable where such an electrosorption of DNA to gold is desirable, for example, in biochip sensors or the like (4-6). DNA templated metal wire formation or the surface attachment of origami are other prominent examples, where a triggered chemical attachment of DNA would be of great advantage (7-10). A wealth of experimental data for DNA in electric fields at surfaces is available for instance in potentiometric and amperometric

sensors, nanodevices and other technological applications (11-17). AFM-based single molecule force spectroscopy seems a natural choice to investigate the interaction of DNA with surfaces, and cyclic voltammetry is the established technique to analyze and to control the electrochemistry of gold as a function of its potential (18-21). We employed a combination of both of these techniques for this study (see Fig. 1).

We covalently attached one strand of dsDNA to the tip of the AFM cantilever by thiol/peptide chemistry (see Supporting Online Material). We then adjusted the surface potential of a 100  $\mu\text{m}$  gold microelectrode by potentiostatic control with respect to a Ag/AgCl reference electrode. At 0 V we approached the surface with the tip. No measurable interaction was recorded neither upon approach nor retraction. The tip was then kept 200 nm above the surface while the potential was ramped to -1 V and back to 0 V. Upon retracting the tip, a force extension trace with all of the typical features of a single dsB-DNA was recorded: Entropic elasticity followed by the BS plateau at 65 pN (22-24). At the end of the unbinding transition at roughly 180 pN the two strands are already separated, so that the measured force increase up to 250 pN is a strong indication that the same strand, which was covalently attached to the tip, had established a stable interaction with the

<sup>1</sup>Chair for Applied Physics and Center for NanoScience, Ludwigs-Maximilians-Universität Munich, Amalienstrasse 54, 80799 Munich  
<sup>2</sup>Center for Integrated Protein Science Munich

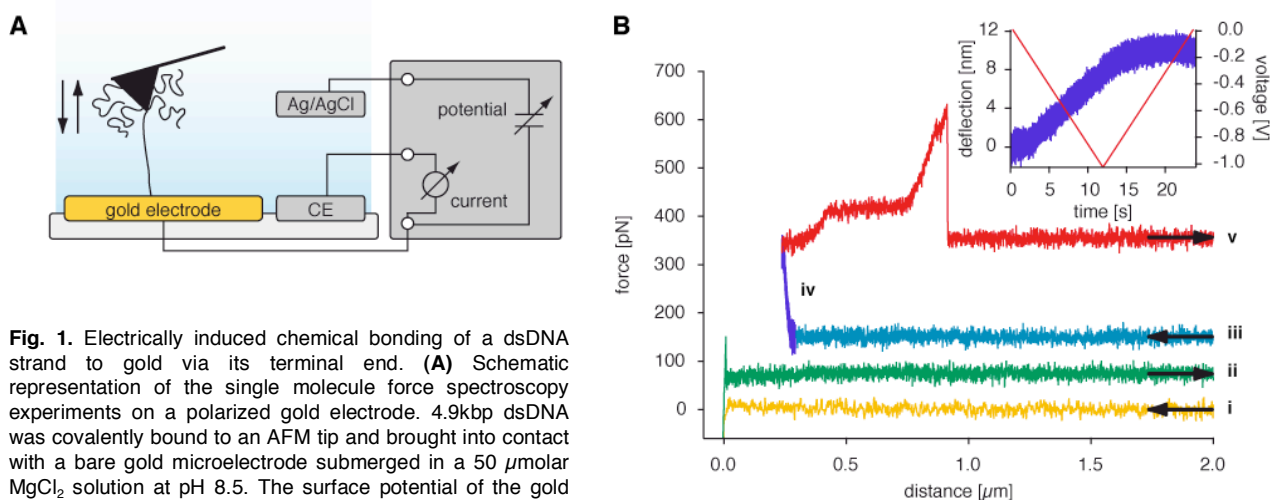


**Fig. 1.** Electrically induced chemical bonding of a dsDNA strand to gold via its terminal end. **(A)** Schematic representation of the single molecule force spectroscopy experiments on a polarized gold electrode. 4.9kbp dsDNA was covalently bound to an AFM tip and brought into contact with a bare gold microelectrode submerged in a 50  $\mu\text{molar}$   $\text{MgCl}_2$  solution at pH 8.5. The surface potential of the gold electrode versus an Ag/AgCl reference electrode was controlled by a potentiostat through a platinum counter electrode (CE). **(B)** Electrosorption of a dsDNA molecule. At zero potential, the AFM tip was brought into contact with the surface and was retracted (i, ii). Then the tip approached the surface again, and kept 200 nm above the surface (iii) while the potential was changed from 0 V to -1 V and back to 0 V with a sweep rate of 85 mV/s (iv). Finally, the tip was retracted completely and the stretching of a single dsDNA molecule followed by the characteristic plateau of the BS transition, the melting of the DNA and finally the complete detachment of the DNA could be monitored (v). The insert shows the drift and the crosstalk of the potential sweep into the deflection signal caused by the polarization currents. It corroborates that the tip and gold surface were not in contact while the DNA was “electrosorbed” to the surface.

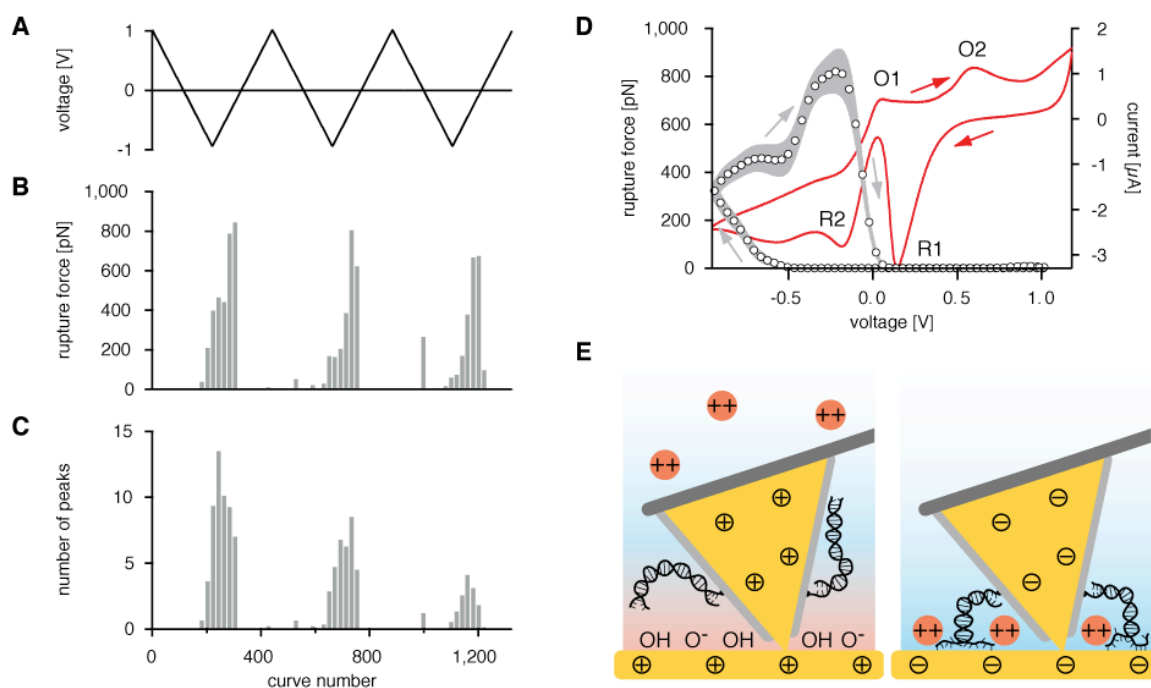


**Fig. 2.** Electrochemistry of DNA-gold bonding. **(A)** As in classic cyclic voltammetry, the potential of the gold electrode was ramped between -1.0 and 1.0 V in 10 mV steps. In between the steps, a force curve was recorded. **(B)** The magnitude of the last step in the force curve, resulting from a single molecule detachment and **(C)** the overall number of rupture peaks throughout the force curve, reflecting the number of bound molecules were extracted. A counterintuitive rupture force distribution was monitored: dsDNA was bound to the bare gold electrode at high negative potential values around -1 V, and the resulting rupture forces were in the range up to 800 pN. Moreover, the asymmetric rupture force peaks around -1 V exhibited a marked hysteresis. This pattern of the rupture forces was found to be persistent over a large number of cycles. However, a global decrease in the number of bound molecules could be observed indicating an increasing passivation or depletion in the contact zone of tip and gold surface. **(D)** Direct comparison of the binned and smoothed rupture forces (circles, grey error bars indicate the interpolated standard error of the mean) and the polarization current (red) plotted in a cyclic voltammogram (recorded at 100 mV/sec). Indicated are the well-known oxidation and reduction peaks of the gold surface. **(E)** Schematics of the molecular arrangement (see text for details).

gold surface during the potential sweep. The fact that the BS plateau is pronounced and has the standard height indicates that this is a point interaction of the DNA with the gold surface.

To probe at which potential this electrically induced attachment had occurred, we performed single molecule force spectroscopy scans while we ramped the surface potential in 10 mV steps (see Fig. 2) (25). For these prolonged scans, we had to increase the functionalization density of the tip, at the cost of multiple DNA interactions during contact. But with a higher tip functionalization density we increased the storage capacity of the tip and were able to complete several voltammetry cycles with the same tip. Nevertheless, we were still able to resolve the rupture force of individual DNA molecules by analyzing only the last step in the force curves. In addition we were able to quantify the wear out of the tip functionalization by analyzing the number of interacting molecules with time.

The most remarkable and at first absolutely counterintuitive feature seen in Fig. 2B is the asymmetric distribution of rupture forces at negative potentials! Both

the distribution as well as the magnitude of the rupture forces was persistent over several cycles. Not so for the number of interacting molecules, which constantly decreased from cycle to cycle (see Fig. 2C). In order to gain further insight into the electrochemistry of this process we plotted the rupture forces against the potential in the same format as in cyclic voltammetry and named these plots roburograms (robur means force in Latin) (Fig. 2D). The well-known oxidation and reduction peaks of the gold electrode are pronounced in the cyclic voltammogram and mark the borders of the window in which measurable rupture forces were found (19, 26). This gives the first clear hint that only a reduced gold surface binds DNA. But why is the negatively charged DNA not repelled by the negatively polarized gold electrode? The strong hysteresis of the roburogram indicates that the interaction of the DNA with the gold surface has a pronounced memory. The explanation is summarized in Fig. 2E: At positive potentials the gold surface is oxidized and not reactive. At negative potentials Mg<sup>2+</sup> ions migrate to the gold electrode and increasingly cover the gold surface. When the gold-coated tip touches

the gold surface, the electrical contact (contact resistance of 40 Ω) short circuits the electric field in the contact zone, and the positive charge of the magnesium ions attracts the DNA to the gold electrode. Even when the scan direction is reversed, the potential is still negative and an increasing number of Mg<sup>2+</sup> ions are accumulated on the electrode, increasing the attraction and increasing the likelihood for multiple bonds to form (27). As a consequence the rupture force increases until oxidation sets in, rendering the electrode non-reactive again.

As yet, we have not discussed the reactive species on the DNA. It is well known that the ends of double stranded DNA are not blunt but tend to open up along several base pairs in a highly dynamic manner (28, 29). It is thus likely that the bases come into contact with the gold surface. These bases have primary amine groups with the exception of thymine. Since in the previous experiments we had learned that a slightly basic pH, which is created through hydrolysis at negative potentials (30), is required for bonding, it is conceivable, that the amines interact with under-coordinated, reduced gold atoms and form

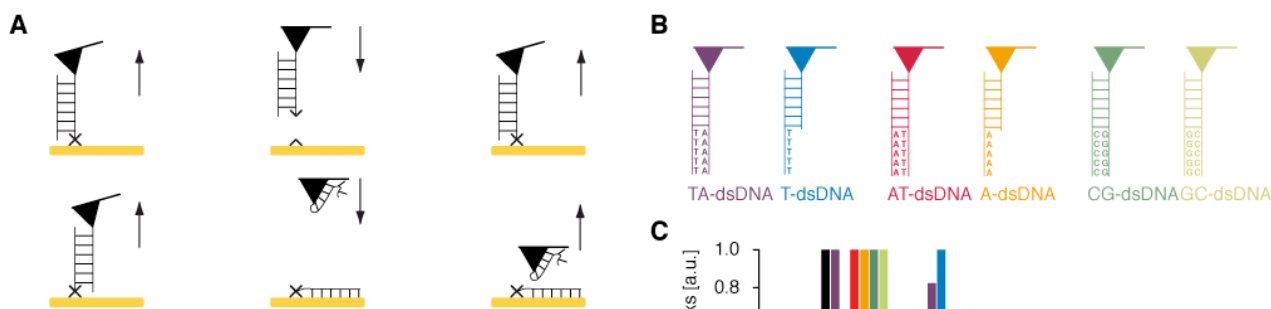


**Fig. 3.** Nucleotide specificity of DNA-gold electroadsorption. **(A)** Schematics of strand separation and bond rupture of dsDNA under force. One strand is covalently attached to the tip, and either the same (upper row) or the counter strand (lower row) is electroadsorbed to the gold surface. If the covalent bonds in the attachment and the DNA backbone are stronger than the coordinative bond, the latter will rupture with higher probability and repetitive electroadsorption is possible. If the counter strand is chemisorbed, both strands will unbind. Single stranded DNA is known to strongly interact with the gold surface and chances for re-hybridization are strongly reduced. **(B)** In addition to the heterogeneous dsDNA shown in Fig 2, the depicted six dsDNA molecules with five homogenous base pairs at the end or five overhang bases were tested. Thereby, the dsDNA was always covalently attached with one single strand to the AFM-tip. **(C)** As a relative measure for the wear out of the tip, the number of rupture peaks for one potential cycle were summed and normalized. The heterogeneous dsDNA, TA-dsDNA and T-dsDNA (black and blue curves) could be desorbed over the five cycles, whereby the TA-dsDNA was the most stable construct. With AT-, A-, CG- and GC-dsDNA, the interaction ceased rapidly, indicating that those dsDNA molecules were separated when stretched. As only thymine exhibits no primary amino group, this result strikingly corroborates our previous assumption that chemisorption of DNA to gold occurs via the primary amino groups on the bases.

a coordination bond (31-34). In order to test this hypothesis we performed the same experiment as before but now with a set of constructs, where we systematically altered the base pair sequences at the end, which were then exposed to the gold

surface.

As depicted in Fig. 3A, we expect that if the strand, which is covalently attached to the tip chemisorbs to the gold surface at the other end, this coordinate bond will rupture at elevated forces. The dsDNA

may be stretched through the BS transition but the counter strand will remain at least loosely attached, so that in repeated experiments, the coordinate bond may be formed again. However, if the counter strand chemisorbs, both strands are separated upon retraction (35, 36). Single stranded DNA is known to strongly interact with gold surfaces so that a re-annealing of the DNA is very unlikely (37, 38). This will result in an increasing deposition of single stranded DNA on the surface and therefore, a rapidly decreasing number of bond formations, which was easily measurable. Fig. 3C shows the number of rupture events recorded during a full cycle for the different constructs depicted in Fig. 3B. Strikingly those constructs, where exclusively thymines on the counter strand formed the contact zone, had the longest lifetimes, whereas wear out of the tip was maximized in those cases where thymines were on the same strand as the attachment to the tip. For detailed discussion and additional data, please refer to the Supporting Online Material. Since thymidine is the only nucleotide without a primary amine, these results clearly show that the primary amines on the bases at the end of the DNA bind to the gold surface!

We had speculated in the beginning that multiple bonds may be the cause of the wide spread of the measured rupture forces. To test this assumption we attached different single nucleotides via PEG-spacers to the tip and measured the rupture forces for several potentials. The result is depicted in Fig. 4. We found no measurable interaction for thymine, regardless of the potential. For adenine we

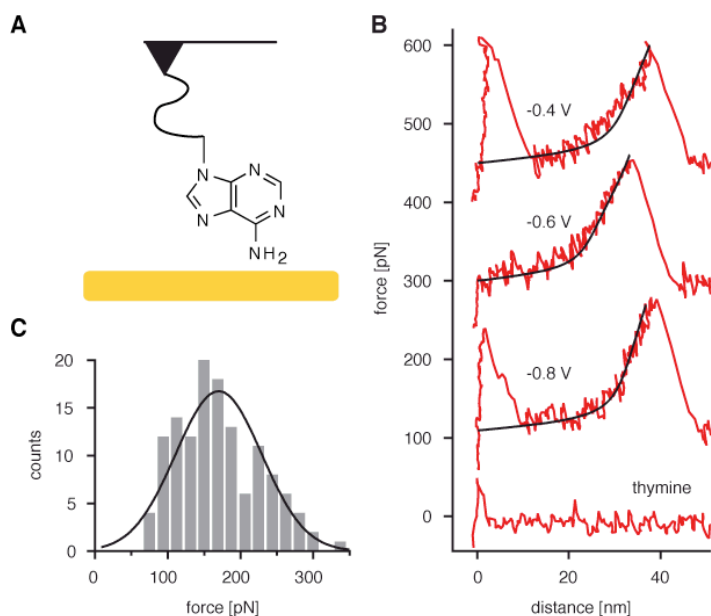


**Fig. 4.** Coordination bond rupture of individual nucleotides. **(A)** A single nucleotide was attached to a 10 kD PEG spacer molecule, which itself was covalently bound to the AFM-tip. **(B)** Typical examples of force-extension curves, with adenosine (upper trace) and thymidine (lower trace) as the nucleotides were recorded at constant potentials ranging from -0.4 V and to -0.7 to -1 V. No measurable interaction could be observed for the thymine PEG whereas for adenosine, the stretching of the PEG spacer (two-state FJC fit, black curve) and the rupture of the N-Au bond in the range of 180 pN could be repeatedly observed. No marked difference was found between the three different potentials. **(C)** The corresponding histogram of 135 force-extension curves delivers an average rupture force of  $170 \pm 50$  pN.

found clear single molecule stretching signatures in the force scans and rupture forces which were virtually indistinguishable for the different potentials.

The mean forces of 170 pN varied by less than 15 pN, whereas the half-width of the histograms was more than 50 pN. Those histograms (depicted in Fig. 4C) show a rather broad distribution with an asymmetric shape. The broad distribution is not surprising, if one takes into account, that the gold surface is rough and heterogeneous at the atomic level. The mean value can be rationalized by a simple estimate. With typical energies reported for the Au-N-bond of 32-42 kJ/mol and estimated bond lengths of 0.3 nm one would expect a barrier force of 185 pN as a realistic estimate (39, 40). These results indicate that the rupture of the coordinate bond is largely potential independent and that the higher rupture forces found in the DNA experiments stem from multiples bases electroadsorbed to the gold surface. The formation of such a bond however was found to be sensitively dependent on the electrochemistry at the surface. The control of these parameters thus enables us to electrochemically bond individual DNA strands at their ends to gold surfaces. Single molecule contacts can be guided to chosen positions and stably attached by an electrical trigger much like bonding a wire to a contact. With the enormous range of applications for DNA both as a key biomolecule and increasingly as a programmable nanoscale building block this option to electrically induce the chemisorption of individual DNA strands and define their positions on a surface with the precision of the AFM will find a richness of novel applications.

#### References and Notes

- S. K. Kufer, E. M. Puchner, H. Gumpf, T. Liedl, H. E. Gaub, *Science* **319**, 594 (Feb, 2008).
- E. M. Puchner, S. K. Kufer, M. Strackharn, S. W. Stahl, H. E. Gaub, *Nano Letters* **8**, 3692 (2008).
- S. K. Kufer *et al.*, *Nature Nanotechnology* **4**, 45 (2009).
- E. M. Boon, D. M. Ceres, T. G. Drummond, M. G. Hill, J. K. Barton, *Nature Biotechnology* **18**, 1096 (Oct, 2000).
- J. Wang, *Nucleic Acids Research* **28**, 3011 (2000).
- R. McKendry *et al.*, *Proceedings of the National Academy of Sciences of the United States of America* **99**, 9783 (Jul, 2002).
- E. Braun, Y. Eichen, U. Sivan, G. Ben-Yoseph, *Nature* **391**, 775 (1998).
- E. Winfree, F. R. Liu, L. A. Wenzler, N. C. Seeman, *Nature* **394**, 539 (1998).
- P. W. K. Rothmund, *Nature* **440**, 297 (2006).
- P. E. Marszalek, W. J. Greenleaf, H. B. Li, A. F. Oberhauser, J. M. Fernandez, *Proceedings of the National Academy of Sciences of the United States of America* **97**, 6282 (Jun, 2000).
- N. J. Tao, J. A. Derose, S. M. Lindsay, *Journal of Physical Chemistry* **97**, 910 (Jan, 1993).
- J. Wang *et al.*, *Analytica Chimica Acta* **337**, 41 (1997).
- M. C. Daniel, D. Astruc, *Chemical Reviews* **104**, 293 (Jan, 2004).
- F. R. F. Fan, A. J. Bard, *Science* **270**, 1849 (1995).
- T. G. Drummond, M. G. Hill, J. K. Barton, *Nature Biotechnology* **21**, 1192 (2003).
- L. Murphy, *Current Opinion in Chemical Biology* **10**, 177 (Apr, 2006).
- P. Frederix *et al.*, *Current Opinion in Chemical Biology* **7**, 641 (Oct, 2003).
- M. Rief, H. Clausen-Schaumann, H. E. Gaub, *Nature Structural Biology* **6**, 346 (Apr, 1999).
- H. Angerstein-Kozłowska, B. E. Conway, A. Hamelin, L. Stoicoviciu, *Electrochimica Acta* **31**, 1051 (Aug, 1986).
- H. G. Hansma, D. E. Laney, M. Bezanilla, R. L. Sinsheimer, P. K. Hansma, *Biophysical Journal* **68**, 1672 (May, 1995).
- D. Anselmetti *et al.*, *Journal of Vacuum Science & Technology B* **12**, 1500 (May-Jun, 1994).
- C. Bustamante, J. F. Marko, E. D. Siggia, S. Smith, *Science* **265**, 1599 (1994).
- J. F. Marko, E. D. Siggia, *Macromolecules* **28**, 8759 (Dec, 1995).
- S. B. Smith, Y. J. Cui, C. Bustamante, *Science* **271**, 795 (Feb, 1996).
- J. H. Christie, P. J. Lingane, *Journal of Electroanalytical Chemistry* **10**, 176 (1965).
- A. Hamelin, M. J. Sottomayor, F. Silva, S. C. Chang, M. J. Weaver, *Journal of Electroanalytical Chemistry* **295**, 291 (Nov, 1990).
- D. Pastre *et al.*, *Biophysical Journal* **85**, 2507 (Oct, 2003).
- D. Andreatta *et al.*, *Journal of the American Chemical Society* **128**, 6885 (May, 2006).
- A. E. Every, I. M. Russu, *Journal of Physical Chemistry B* **112**, 15261 (Nov, 2008).
- S. Shirahata *et al.*, *Biochemical and Biophysical Research Communications* **234**, 269 (1997).
- B. Q. Xu, N. J. J. Tao, *Science* **301**, 1221 (Aug, 2003).
- F. Chen, X. L. Li, J. Hihath, Z. F. Huang, N. J. Tao, *Journal of the American Chemical Society* **128**, 15874 (Dec, 2006).
- L. Venkataraman, J. E. Klare, C. Nuckolls, M. S. Hybertsen, M. L. Steigerwald, *Nature* **442**, 904 (Aug, 2006).
- S. Grunder *et al.*, *Journal of Organic Chemistry* **72**, 8337 (Oct, 2007).
- T. Strunz, K. Oroszlan, R. Schafer, H. J. Guntherodt, *Proceedings of the National Academy of Sciences of the United States of America* **96**, 11277 (Sep, 1999).
- J. Morfill *et al.*, *Biophysical Journal* **93**, 2400 (Oct, 2007).
- T. M. Herne, M. J. Tarlov, *Journal of the American Chemical Society* **119**, 8916 (Sep, 1997).
- J. J. Storchhoff, R. Elghanian, C. A. Mirkin, R. L. Letsinger, *Langmuir* **18**, 6666 (2002).
- A. Bilic, J. R. Reimers, N. S. Hush, J. Hafner, *Journal of Chemical Physics* **116**, 8981 (2002).
- N. A. Lambropoulos, J. R. Reimers, N. S. Hush, *Journal of Chemical Physics* **116**, 10277 (2002).
- We thank D. Ho, W. Schuhmann and U. Sivan for helpful discussions. This work was supported by the German Science Foundation (SFB 486) and the Nanosystems Initiative Munich (NIM). AF thanks the Alexander von Humboldt Foundation for their generous support.

#### Supporting Online Material

# Supporting Online Material

## Bonding DNA to Gold

*Matthias Erdmann, Ralf David<sup>+</sup>, Ann R. Fornof\* and Hermann E. Gaub*

Chair for Applied Physics and Center for NanoScience,  
Ludwigs-Maximilians-Universität Munich,  
Amalienstrasse 54, 80799 Munich

+ Center for Integrated Protein Science Munich

\*to whom correspondence should be addressed: [Ann.Fornof@physik.uni-muenchen.de](mailto:Ann.Fornof@physik.uni-muenchen.de)

## 1. Material and Methods

**AFM.** We used a commercial instrument (Molecular Force Probe 3D from Asylum Research, Santa Barbara, CA/USA) and silicon nitride cantilevers (Veeco GmbH, Mannheim, Germany, MLCT-AUHW). The spring constants of each cantilever were individually calibrated by thermal calibration. Moreover, a PEEK-cantilever holder from Asylum Research was used to avoid having additional metal parts in the solution.

**Samples.** dsDNA fragments of 4.9kbp ( $\sim 100\text{ng}/\mu\text{l}$  concentration) were obtained by PCR with Fusion polymerase (Finnzymes, Espoo, Finland) using a pet28a-vector (Novagen, Merck Biosciences, Nottingham, United Kingdom) as a template, 5'-amino-modified forward primer, and a corresponding reverse primer from a supplier (IBA GmbH, Göttingen, Germany). The dsDNA was purified with the Qiagen PCR Purification Kit (Qiagen, Hilden, Germany). Agarose gel electrophoresis was used to confirm the homogeneity of the DNA length.

For the TA-, AT-, GC- and CG-dsDNA the corresponding reverse primers were elongated at the 5'-end by an additional five homogenous bases A, T, C or G. The overhangs were filled by the polymerase with complementary bases during amplification. To generate a five A or T single strand overhang a hexaethylene glycol-spacer was inserted between the reverse primer and the A or T overhang to avoid a filling with complementary bases.

Experiments were performed in  $50\ \mu\text{M}$   $\text{MgCl}_2$  (water: chromatography water (LiChrosolv, Merck, Darmstadt)) containing traces of NaOH or HCl to ensure pH values of 5.5, 8.5 or 10. All chemicals were purchased from Sigma Aldrich if not otherwise identified.

**Tip functionalization.** The covalent attachment of dsDNA to the AFM tip was accomplished through the reaction of an activated carboxylic acid on the tip and a primary amine from the primer on the dsDNA. To accomplish this binding chemistry, the cantilevers were coated with a  $30\ \text{\AA}$  chrome-nickel (80:20) layer followed by a  $300\ \text{\AA}$  layer of gold by thermal evaporation. These cantilevers were then etched for 2 min in a solution containing  $\text{H}_2\text{O}$  (Milli-Q water),  $\text{NH}_3$  (37%) and  $\text{H}_2\text{O}_2$  (30%) with the ratio 10:1:1 and then rinsed with ethanol (puriss.). Afterwards, the cantilevers were immediately incubated in a solution of 16-mercaptohexadecanoic acid (0.5 mM), 11-mercaptoundecanol (0.05 mM) and tris(2-carboxyethyl)phosphine-hydrochloride (TCEP, 0.05 mM) in ethanol (puriss) for at least 12 h. For the dsDNA functionalization, the cantilevers were first rinsed in chromatography water (LiChrosolv, Merck, Darmstadt). Then the carboxylic acid groups of the SAM were reacted with the amino end groups of the dsDNA in a

solution of 10  $\mu\text{l}$  DNA and 20  $\mu\text{l}$  chromatography water containing 1-ethyl-3-(3-dimethylaminopropyl) carbodiimide (EDC) for 30 min. 15 mg EDC were dissolved in 300  $\mu\text{l}$  chromatography water for the latter stock solution. The large excess of EDC enables the carboxy-amino coupling in the polar solution; the usage of chromatography water ensures constant coupling conditions at pH 7. After functionalization, the cantilevers were rinsed thoroughly in the  $\text{MgCl}_2$  solution and then immediately used in the experiments.

The functionalization of 10 kD PEG and single nucleotides to the AFM-tip was accomplished according to a published and a new functionalization protocol, respectively (1, 2).

**Electrodes.** The gold electrodes were directly evaporated on a clean polycarbonate slide and had an area of 0.1 mm x 20 mm plus an area of 1  $\text{cm}^2$  for electrical contacting. The thickness of the electrode was 200 nm. A mask of stainless steel (Ätztechnik Herz GmbH&Co, Epfendorf, Germany) was used during thermal evaporation. Before use in the experiment, the electrodes were first rinsed with ethanol (puriss), Milli-Q water and the  $\text{MgCl}_2$  solution. The electrodes were then dried with nitrogen to ensure a dry contacting area for BNC cables. For a three-electrode setup, a commercial Ag/AgCl microelectrode (Microelectrodes Inc., Bedford, USA) was used as the reference electrode and a platinum wire as the counter electrode. All potentials applied to the gold electrodes are given versus the Ag/AgCl electrode. The counter and reference electrodes were inserted into a bare shaped cavity, which was milled into the polycarbonate slide before functionalization. Then the  $\text{MgCl}_2$  solution was added to determine an effective electrode area of 0.1 mm x 5 mm covered by the solution. Before the AFM experiment, 20 cleaning voltammograms in the range of  $\pm 1.2$  V were recorded with a sweep rate of 0.1 V/s.

**Measurements and Analysis.** Force extension curves were measured on the gold electrode. The dsDNA-functionalized AFM tips were brought into contact with the surface for 0.5 s and retracted with a speed of 1.5  $\mu\text{m/s}$ . In an experiment, thousands of force curves were recorded with changing potential from curve to curve (10 mV potential change per curve). In order to minimize artefacts in the deflection signal, which are related to the ion current, the potential was changed by 10 mV steps after each force extension trace with the AFM-tip held 3  $\mu\text{m}$  away from the electrode. The potential was adjusted by a commercial potentiostat (1002 PC.T., Jaissle Elektronik GmbH, Waiblingen, Germany), whereby a custom procedure in Igor 6.0 controlled the potential change with each force curve. This procedure was implemented in the MFP3D-code. The last rupture forces and peak numbers were also determined with a custom procedure in Igor 6.0. Additionally, the last rupture forces and rupture peak numbers were plotted versus the curve



number and binned in following manner: The average rupture force or peak values of 20 force extension curves were determined in Igor 6.0 and plotted as bars in the corresponding graph. The rupture force and peak number distributions were then smoothed and interpolated. The resulting standard error of the mean of one binning interval can be found as the interpolated grey area in the corresponding roburogram. This procedure explains the occurrence of forces significantly lower than 200 pN: if only two rupture events with a last rupture force of 200 pN was monitored over 20 force curves, the resulting average force appears to be 20 pN in the binning interval of the roburogram. The two-state FJC-fit for a stretched 10 kD PEG spacer in Figure 4 was accomplished in Igor 6.0 utilizing literature values (3).

## 2. Example force curves for different potentials

For different voltage regimes in the anodic and cathodic scan direction, several force extension curves are presented. Due to the high functionalization density on the AFM-tip, which was set high to allow for a long lifetime of the tip, the detachment of several dsDNA molecules can be observed.

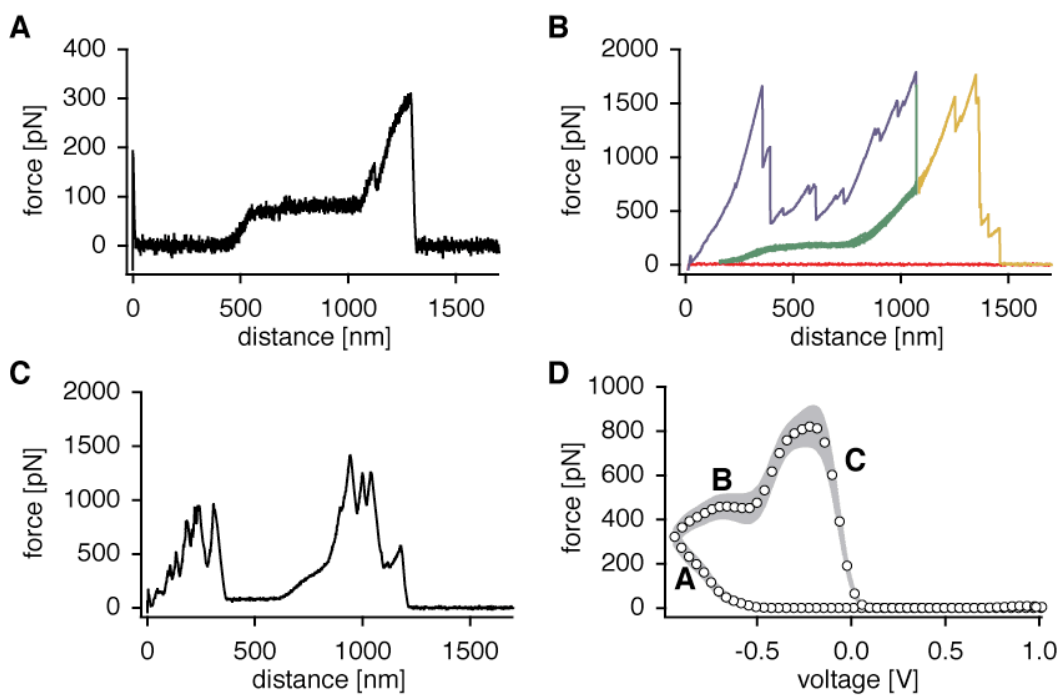


**Figure S1.** Example force extension curves. (A), (B) and (C) show different dsDNA force-extension curves from the gold electrode for different potentials (D). In order to identify dsDNA in (B), the pinned molecules were relaxed and stretched two times (green curve). Thereby, the parallel BS-transition of at least four dsDNA-molecules was observable.

In the beginning of an experiment, the known BS-transition of dsDNA is difficult to identify, as a large number of dsDNA molecules are sticking to the surface and are stretched in parallel. To prove the presence of dsDNA, the following measurement protocol in the  $z$ -direction was performed (Fig. S1B): The AFM tip was brought into contact with the electrode surface (red curve) and then retracted to 1.1  $\mu\text{m}$  above the surface (blue curve). Afterwards, the tip

approached the surface, but stopped 0.12  $\mu\text{m}$  above it. The twofold up-and-down movement of the AFM-tip (green curve) within these heights reveals the relaxation on the BS-plateaus and the subsequent stretching of three independent dsDNA molecules in parallel. Finally, the AFM tip was retracted (yellow curve) to detach the dsDNA molecules completely.

### 3. Different dsDNA endings

dsDNA molecules with different endings were synthesized and investigated with the gold electrode under potentiostatic control. Marked differences for the integrated peak distributions can be seen in Fig. 3C: only the TA-dsDNA could be reversibly detached from the gold surface. The heterogeneous dsDNA and the T-dsDNA also had longer lifetimes than the AT-, A-, GC- and CG-dsDNA constructs. After only one cycle, virtually no molecules were electrosorbed to the surface for these constructs. Hence, melting of the two strands was assumed as the basis for the short lifetimes as ssDNA eludes potentiostatic control, which was described in the manuscript. The melting mechanism was attributed to the different stretching conformations: adenine binds with gold through its primary amino group; however, thymine does not contain a primary amine and therefore, does not coordinate with gold. Thus, the TA-dsDNA molecule was attached and therefore, stretched only at a single strand. The strand, which was not under load, stayed in the vicinity of its complementary strand and melting was prevented. For the TA-dsDNA, nitrogen-gold bond rupture may be more likely before the two strands are completely melted. Therefore, several voltage cycles were possible. In contrast, if both strands of a dsDNA molecule are simultaneously stretched (shear conformation), melting of the two strands is favoured (*1*). This process was identified for the heterogeneous dsDNA and the T-dsDNA, which are comparable. Because thymine does not bind to gold, an opening of the strands of T-dsDNA was required to form N-Au bonds. This is equivalent to the bonding characteristics of dsDNA, as the same heterogeneous sequences were then interacting with the gold surface. Due to the heterogeneous sequence, the lifetime of the heterogeneous dsDNA and the T-dsDNA was shorter than the TA-dsDNA but longer than the AT-, GC- and CG-dsDNA. For A-, GC- and CG-dsDNA, there was a primary amino group exposed to enable the shear conformation, which led to the fast decay in the number of rupture peaks in Fig. 3C. GC- and CG-dsDNA showed faster rupture peak decays, since both strands exhibited a primary amino group. A-dsDNA, which provided a five-fold sticky amino end, could only be cycled once. Here, binding of the free amino groups of adenine to the gold surface was highly favoured; therefore, these molecules were predominantly stretched in the shear conformation and were melted away immediately.

## Reversible potential cycles

### TA-dsDNA

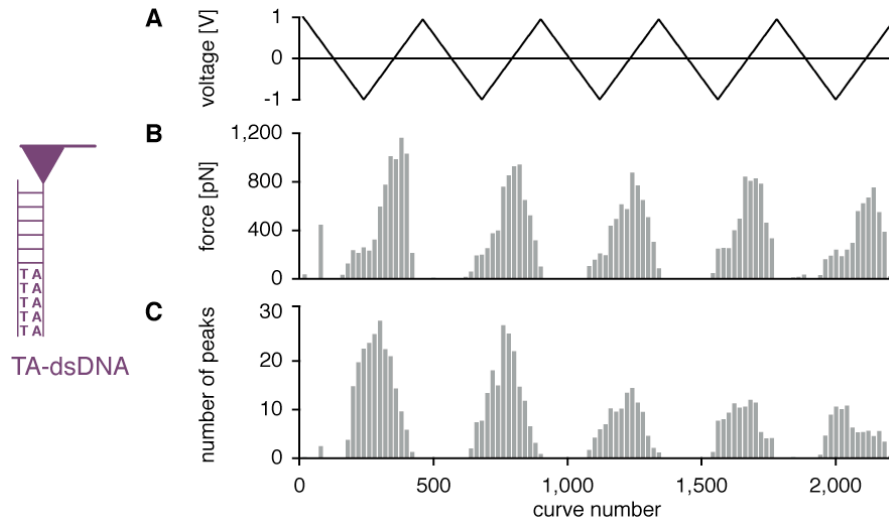


**Figure S2.** Reversible potential cycles of TA-dsDNA.

### T-dsDNA

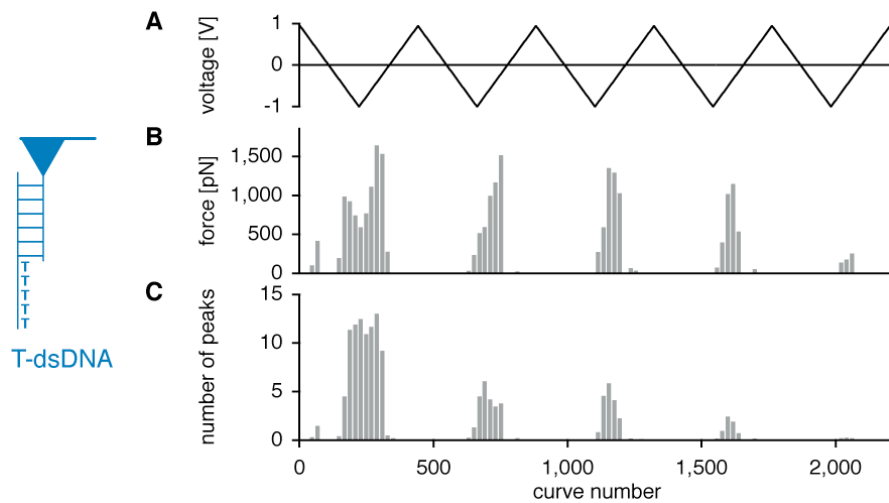


**Figure S3.** Reversible potential cycles of T-dsDNA.

## Irreversible potential cycles

### AT-dsDNA

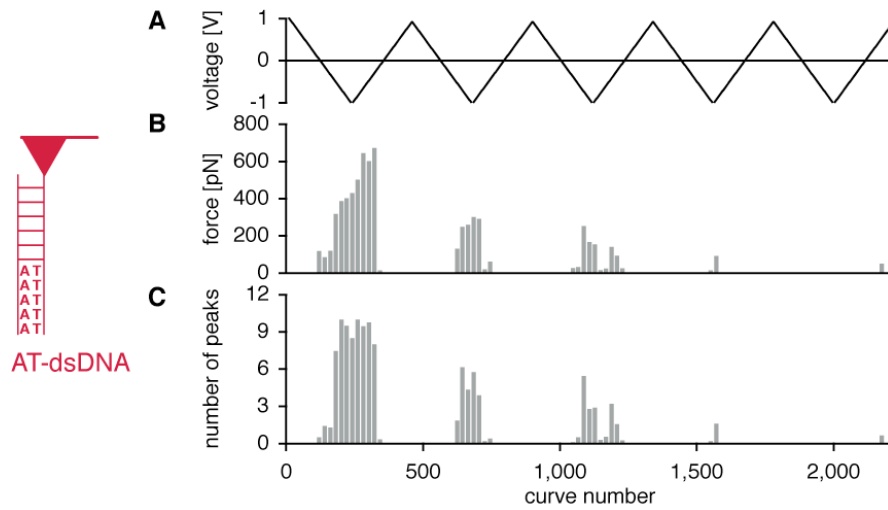


**Figure S4.** Irreversible potential cycles of AT-dsDNA.

### A-dsDNA

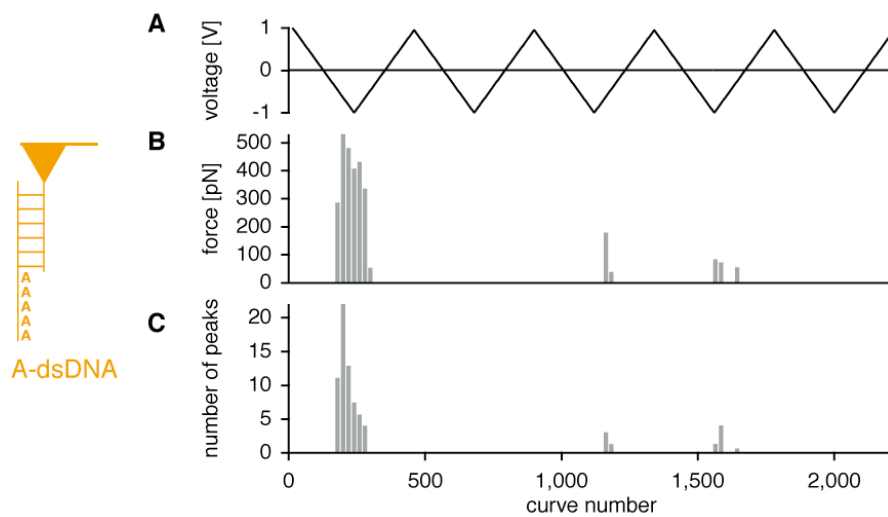


**Figure S5.** Irreversible potential cycles of A-dsDNA.

## CG-dsDNA

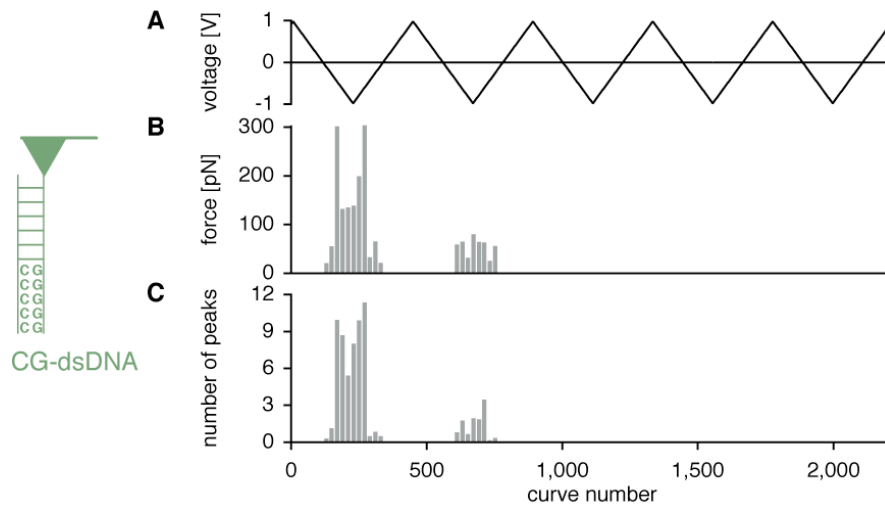


**Figure S6.** Irreversible potential cycles of CG-dsDNA.

## GC-dsDNA

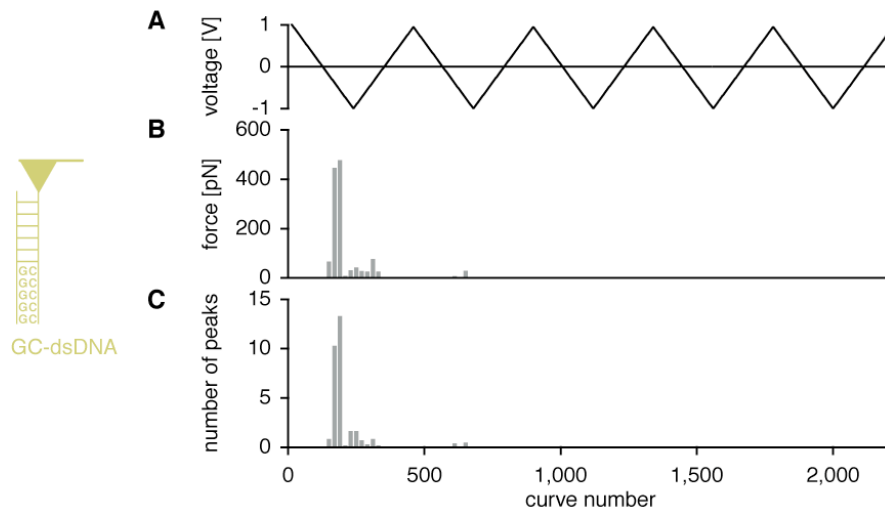


**Figure S7.** Irreversible potential cycles of GC-dsDNA.

#### 4. N-Au bonds prevent lateral mobility of dsDNA on gold

The point-like pinning (N-Au bond) of dsDNA on the gold electrode was confirmed by the following experiment (4): The cantilever was not only retracted vertically, but also at different pulling angles  $\Omega$  with respect to the surface. Thereby, the rupture forces and lengths were measured. If the dsDNA was laterally mobile and able to follow the cantilever movement as it was shown in case of physisorption, an equilibrium polymer angle  $\Phi$  would be established and the rupture lengths would not decrease with a factor of  $\cos(\Omega)$ . In contrast, if an electrosorbed dsDNA molecule is pinned at the surface and is not able to follow the horizontal movement of the cantilever, the equilibrium polymer angle  $\Phi$  equals the pulling angle  $\Omega$ . Moreover, measured rupture lengths decrease with a factor of  $\cos(\Omega)$ . The recorded rupture lengths of dsDNA on gold at -0.5 V for different pulling angles decrease in this manner, whereby point-like pinning is confirmed (Fig. S8B).

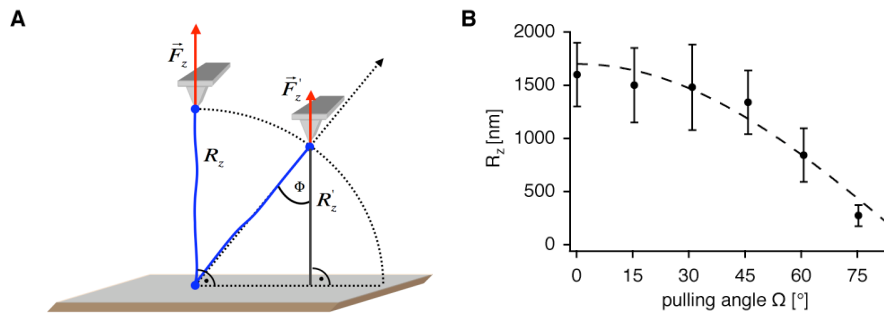


**Figure S8.** Pinning of dsDNA on the gold electrode. **(A)** Scheme of the experimental procedure: the cantilever is retracted at an angle  $\Omega$  from its starting point. If the polymer is unable to follow the lateral velocity component of the cantilever due to pinning, the equilibrium polymer angle  $\Phi$  equals the pulling angle  $\Omega$  and the rupture lengths decrease with a factor of  $\cos(\Omega)$  **(B)** The rupture lengths of dsDNA decrease with a factor of  $\cos(\Omega)$  (dashed line).



## 5. pH-value influence

The coordinate N-Au bond requires deprotonated primary amino groups, whereby  $pK_a \approx 9$  for this amino group (5). As the experiments were conducted in an unbuffered solution, water hydrolysis shifts the pH value in the vicinity of the electrode, which is normally pH 8.5. At pH 8.5 far from the electrode, more than half of the exposed amino groups should be protonated. The pH-value increase at applied potentials below  $-0.7\text{ V}$  ( $2H_2O + 2e^- \rightarrow H_2 + 2OH^-$ ) promoted the N-Au bonding due to the uncharged amino groups (6). This assumption also explains, why no rupture events were detected at applied positive potentials: because of a decreased pH-value ( $6H_2O \rightarrow O_2 + 4H_3O^+ + 4e^-$ ), more amino groups were protonated ( $NH_3^+$ ), thus N-Au bonding was not favoured. Hence, an interaction between gold and amino groups was also less likely. We could confirm the influence of the pH-value with respect to the charging of the amino group by conducting the same experiments at pH 5.5 and pH 10. At pH 5.5, no rupture events were recorded, which was attributed to the microenvironment close to the electrode staying in a pH range such that the primary amines remained protonated. Thus, the charged  $NH_3^+$ -groups, which do not have a lone electron pair, were not able to form coordinate bonds with the gold adatoms.

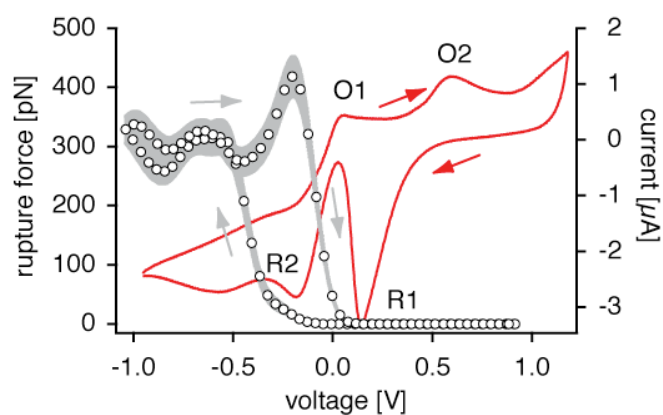


**Figure S9.** Roburogram at pH 10. The rupture force events set in earlier at  $-0.3\text{ V}$  in the cathodic direction due to the predominant basic pH-value. At  $0\text{ V}$  in the anodic direction, the rupture force events disappear due to surface oxidation.

At pH 10, when the amino group is generally uncharged, an earlier onset of rupture events could be monitored as soon as the gold surface was reduced. However, because of the increased pH-value, the dsDNA is already destabilized and less force load is necessary to melt the two strands.

At pH 11.5, the dsDNA backbone starts separating due to charge effects (7). This can be seen in reduced BS-plateau forces around 40 pN, which are normally around 65 pN (data not shown). For this reason, higher rupture forces around 800 pN (Fig. 2D) of several N-Au bonds are not observed as the dsDNA molecule is already melted and separated at lower forces.

These experiments confirm the importance of water dissociation in order to shift the pH-value. Thus, the formation of N-Au bonds by deprotonating or protonating the amino groups of the dsDNA is triggered electrochemically in the range around pH 8.5.

## 6. Amphifunctional electrified surface model and Mg<sup>2+</sup> adsorption

In order to estimate the Mg<sup>2+</sup> ion concentration on the electrode at applied negative potentials, an amphifunctional surface model from Duval et al. was utilized. (8, 9) This model derives the diffuse layer potential  $\psi_D$  according to the applied electronic potential  $\phi$ . The Mg<sup>2+</sup> ions in solution are then attracted by the diffuse layer potential.

Within this model, the diffuse double layer potential was determined with respect to the applied potential, the oxidation of the gold surface by OH-groups and the Stern-layer. Moreover, the association/dissociation of protons to/from the AuOH-groups according to the pH-value of the solution and the applied potential was taken into account. The total number of AuOH sites is  $N_s = 3 \cdot 10^{14}$  per cm<sup>2</sup> due to the oxidation at positive potentials above 0 V (the gold surface exhibits  $\sim 1.5 \cdot 10^{15}$  gold atoms per cm<sup>2</sup>). In contrast, the reduced gold surface at negative potentials below -0.3 V exhibits only  $N_s = 0.8 \cdot 10^{12}$  per cm<sup>2</sup> hydroxyl sites. (10, 11) Consequently, the gold surface at negative potentials is more reactive than the hydroxyl-passivated gold surface at positive potentials.

In detail, electroneutrality is demanded for the electric surface charge density  $\sigma^e$ , the protonic surface charge density  $\sigma^p$  and the diffuse layer charge density  $\sigma^d$ :

$$\sigma^e + \sigma^p + \sigma^d = 0 \quad (1)$$

These charge densities are written in terms of one independent variable, the diffuse layer potential  $\psi_D$ , which depends on the applied potential  $\phi$ :

$$\sigma^e(\phi, \psi_D) = C_0(\phi - \psi^0(\psi_D)) \quad (2)$$

$$\sigma^p(\psi_D) = eN_s \frac{\left(c_{H^+}^\infty / K_{a1}\right) e^{-ze\psi^0(\psi_D)/k_b T} - \left(K_{a2} / c_{H^+}^\infty\right) e^{ze\psi^0(\psi_D)/k_b T}}{1 + \left(c_{H^+}^\infty / K_{a1}\right) e^{-ze\psi^0(\psi_D)/k_b T} + \left(K_{a2} / c_{H^+}^\infty\right) e^{ze\psi^0(\psi_D)/k_b T}} \quad (3)$$

$$\sigma^d(\psi_D) = -C_1(\psi^0(\psi_D) - \psi_D) \quad (4)$$

$$\psi^0(\psi_D) = \psi_D + \left( (8I\epsilon\epsilon_0 RT)^{1/2} / C_1 \right) \sinh\left( \frac{ze\psi_D}{2k_B T} \right) \quad (5)$$

with  $N_s$  being the total number of surface oxidic sites,  $e$  the electron charge,  $c_{H^+}^\infty$  the proton concentration in the bulk,  $I$  the ionic strength,  $\epsilon\epsilon_0$  the total permittivity and the thermal energy  $k_B T$ .  $K_{a1}$  and  $K_{a2}$  are the dissociation constants for the processes





and are defined by

$$K_{a1} = \frac{[-AuOH]}{[-AuOH_2^+]} c_{H^+}^\infty e^{-\frac{e\psi^0}{k_B T}} \quad (8)$$

$$K_{a2} = \frac{[-AuO^-]}{[-AuOH]} c_{H^+}^\infty e^{-\frac{e\psi^0}{k_B T}} \quad (9)$$

Inserting equations (3) to (5) into equation (1) results then in a transcendental expression for the diffuse layer potential  $\psi_D$  depending on the applied potential  $\phi$  to a gold electrode.

For the calculation, the following literature values were used (9):  $N_S = 3 \cdot 10^{14}/\text{cm}^2$ ,  $pK_{a1} = 1$ ,  $pK_{a2} = 8$ ,  $\text{pH} = 8.5$ ,  $C_0 = 5 \mu\text{F}/\text{cm}^2$ ,  $C_1 = 50 \mu\text{F}/\text{cm}^2$ ,  $c(\text{MgCl}_2) = 50 \mu\text{M}$ . In the low voltage regime, a decreased number of oxidic sites is expected due to the reduction of the gold surface (10). A lower density number ( $N_S = 0.8 \cdot 10^{12}/\text{cm}^2$ ) does not change the calculated values drastically. For this reason, the corresponding calculation is not shown.

The calculated diffuse layer potential vs. the curve number is depicted in Fig. S10A, left axis. The number of adsorbed  $\text{Mg}^{2+}$  ions per  $\text{cm}^2$  on the electrode depending on the calculated diffuse layer potential is shown on the right axis:

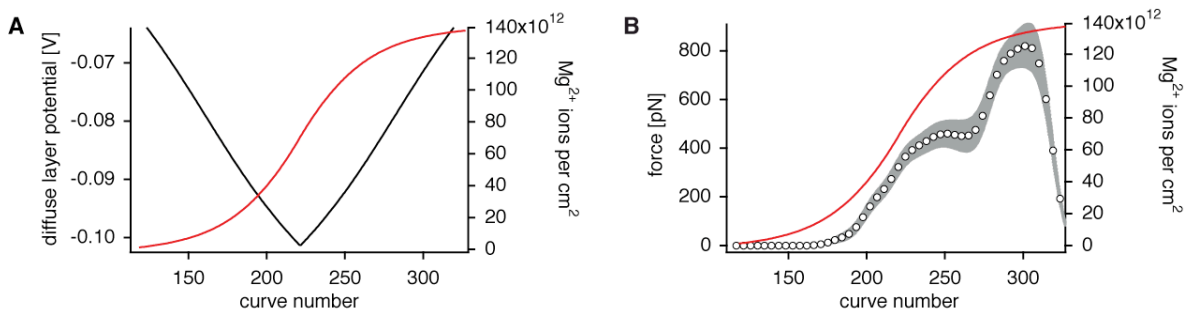


**Figure S10.** (A) Calculated diffuse layer potential and resulting adsorbed  $\text{Mg}^{2+}$  ions density on the electrode. The applied potential to solve equation (1) was taken from Fig. 2. (B) Adsorbed  $\text{Mg}^{2+}$  ions (red curve, right axis) and rupture force of dsDNA (left axis) plotted vs. the curve number. The rupture force was taken from Fig. 2. Both curves exhibit roughly the same increase during the experiment.

The  $\text{Mg}^{2+}$  ion coverage  $\Gamma(t)$  was estimated in a first approximation by the linearized Langmuir isotherms (12) for each diffuse layer potential and the time of one force-extension curve (4.5 s).

$$\Gamma(t) = \Gamma_s \beta c^\infty \cdot \left( 1 - \exp\left(\frac{Dt}{(\Gamma_s \beta)^2}\right) \operatorname{erfc}\left(\frac{(Dt)^{1/2}}{\Gamma_s \beta}\right) \right) \quad (10)$$

Here,  $\Gamma_s = 10^{-9} \text{ mol/cm}^2$  is the maximum coverage,  $\beta = \exp(-ze\psi_D/k_B T)$  is the Boltzmann factor with included activity coefficient units,  $D = 10^{-5} \text{ cm}^2/\text{s}$  is the diffusion coefficient and  $c^\infty$  is the  $\text{Mg}^{2+}$  ion concentration in the bulk solution. The assumption is that once an ion is bound, it will not be released due to the negative potentials. The adsorbed  $\text{Mg}^{2+}$  ions of the subsequent time-interval or force-extension curve are added to the number of already bound ions. As a result, the rupture force and the  $\text{Mg}^{2+}$  concentration increase roughly in the same manner. A higher  $\text{Mg}^{2+}$  coverage and concentration near the surface due to the applied potential promotes dsDNA binding to the gold electrode as discussed in the manuscript.

However, interactions between  $\text{Mg}^{2+}$  ions in general and the influence of the gold surface oxidation has not been taken into account, especially at applied potential higher than 0 V. Furthermore, the impact of the pH-value due to water dissociation, which also favours coordinate binding, is not included in this estimation. This should be noted when comparing the red and black/grey curves. Nevertheless, it can also be seen in Fig. S10B that the rupture force decreases drastically as soon as gold surface oxidation sets in despite the high ion concentration (compare Fig. 2D). Thus, the controlled N-Au bonding mechanism is based on a complex interplay between surface oxidation, pH-value, ion coverage and electrically contacting the electrode with the AFM-tip.

## References

1. S. K. Kufer, E. M. Puchner, H. Gump, T. Liedl, H. E. Gaub, *Science* **319**, 594 (Feb, 2008).
2. R. David, M. Erdmann, A. R. Fornof, H. E. Gaub, *in preparation* (2009).
3. F. Oesterhelt, M. Rief, H. E. Gaub, *New Journal of Physics*|*New Journal of Physics* **1**, 10.1088/1367 (1999).
4. F. Kuhner *et al.*, *Langmuir* **22**, 11180 (Dec, 2006).
5. F. Chen, X. L. Li, J. Hihath, Z. F. Huang, N. J. Tao, *Journal of the American Chemical Society* **128**, 15874 (Dec, 2006).
6. S. Shirahata *et al.*, *Biochemical and Biophysical Research Communications* **234**, 269 (1997).
7. A. M. Nowicka, E. Zabost, B. Klim, Z. Mazerska, Z. Stojek, *Electroanalysis* **21**, 52 (2009).
8. J. Duval, J. M. Kleijn, J. Lyklema, H. P. van Leeuwen, *Journal of Electroanalytical Chemistry* **532**, 337 (Sep, 2002).
9. J. Duval, J. Lyklema, J. M. Kleijn, H. P. van Leeuwen, *Langmuir* **17**, 7573 (Nov, 2001).
10. H. Angersteinkozłowska, B. E. Conway, A. Hamelin, L. Stoicoviciu, *Electrochimica Acta* **31**, 1051 (Aug, 1986).
11. D. Barten *et al.*, *Langmuir* **19**, 1133 (Feb, 2003).
12. A. J. Bard, L. R. Faulkner, *Electrochemical Methods: Fundamentals and Applications* (Wiley & Sons, 2000), pp.

## 6 Outlook

This thesis presented four separate studies to approach the understanding of single polymers on surfaces. Thereby, the conformation and the friction of adsorbed polymers could be determined and their adhesion or bonding mechanisms were controlled and manipulated. The combination or variation of existing experiments and techniques could serve as a basis for further studies or even initiate new technological applications. Therefore, future projects might focus on:

- *Optimization of the AFM-electrode setup.* As bimetal artefacts due to ion currents induced unwanted deflections of the AFM cantilever, the salt concentrations were minimized. Smaller electrodes and uncoated AFM cantilever would avoid this problem, whereby also new functionalization protocols in case of DNA has to be tested. A miniaturization solution could be metal wires, which are fused into etching resistant glass fibers.
- *Variation.* Of course, other polymers and the influence of different salt solutions and pH-values are worthwhile to study. Especially shorter SAM chain lengths in case of DNA adhesion should provide a higher manipulation force range via electric control due to a decreased potential drop.
- *Electrofriction.* Combining the mobility experiments with different applied surface potentials could shed light on possible electrostatic contributions for molecular friction. 2D polymer melts or single polymers with switchable mobility could provide new coatings or nanodelivery systems.
- *SMCP and Electrosorption.* The Single Molecule Cut&Paste technology, which was explained in the Introduction offers a broad range of applications, e.g. enzymatic cascades. Single molecule contacts could be guided to chosen positions and stably attached by an external electrical trigger. Thus, new programmable nanoscale building blocks could be realized.
- *Electric Glue.* Being able to electrically bond synthetic polymers to metals like steel would provide fundamental new industrial applications and adhesives on the macroscopic scale. Or imagine a scotch tape that only glues, if you turn on a switch ...

# A Bibliography

- [1] Binnig, G., C. F. Quate, and C. Gerber: *Atomic Force Microscope*. Physical Review Letters, 56(9):930–933, 1986.
- [2] Rief, M., M. Gautel, F. Oesterhelt, J. M. Fernandez, and H. E. Gaub: *Reversible unfolding of individual titin immunoglobulin domains by AFM*. Science, 276(5315):1109–1112, 1997.
- [3] Radmacher, M., R. W. Tillmann, M. Fritz, and H. E. Gaub: *From Molecules to Cells - Imaging Soft Samples with the Atomic Force Microscope*. Science, 257(5078):1900–1905, 1992.
- [4] Rief, M., F. Oesterhelt, B. Heymann und H. E. Gaub: *Single molecule force spectroscopy on polysaccharides by atomic force microscopy*. Science, 275(5304):1295–1297, 1997.
- [5] Rief, M., H. Clausen-Schaumann und H. E. Gaub: *Sequence-dependent mechanics of single DNA molecules*. Nature Structural Biology, 6(4):346–349, 1999.
- [6] Staudinger, H.: *Nobel Lectures*. Elsevier Publishing Company, Amsterdam, pages 1942–1962, 1964.
- [7] Kufer, S. K., E. M. Puchner, H. Gump, T. Liedl und H. E. Gaub: *Single-molecule cut-and-paste surface assembly*. Science, 319(5863):594–596, 2008.
- [8] Smalley, R. E.: *Of chemistry, love and nanobots - How soon will we see the nanometer-scale robots envisaged by K. Eric Drexler and other molecular nanotechnologists? The simple answer is never*. Scientific American, 285(3):76–77, 2001.
- [9] Boon, E. M., D. M. Ceres, T. G. Drummond, M. G. Hill und J. K. Barton: *Mutation detection by electrocatalysis at DNA-modified electrodes*. Nature Biotechnology, 18(10):1096–1100, 2000.
- [10] Wang, J.: *From DNA biosensors to gene chips*. Nucleic Acids Research, 28(16):3011–3016, 2000.
- [11] McKendry, R., J. Y. Zhang, Y. Arntz, T. Strunz, M. Hegner, H. P. Lang, M. K. Baller, U. Certa, E. Meyer, H. J. Guntherodt und C. Gerber: *Multiple label-free biodetection and quantitative DNA-binding assays on a nanomechanical cantilever array*. Proceedings of the National Academy of Sciences of the United States of America, 99(15):9783–9788, 2002.
- [12] Braun, E., Y. Eichen, U. Sivan und G. Ben-Yoseph: *DNA-templated assembly and electrode attachment of a conducting silver wire*. Nature, 391(6669):775–778, 1998.
- [13] Winfree, E., F. R. Liu, L. A. Wenzler und N. C. Seeman: *Design and self-assembly of two-dimensional DNA crystals*. Nature, 394(6693):539–544, 1998.
- [14] Rothmund, P. W. K.: *Folding DNA to create nanoscale shapes and patterns*. Nature, 440(7082):297–302, 2006.



- 
- [15] Marszalek, P. E., W. J. Greenleaf, H. B. Li, A. F. Oberhauser und J. M. Fernandez: *Atomic force microscopy captures quantized plastic deformation in gold nanowires*. Proceedings of the National Academy of Sciences of the United States of America, 97(12):6282–6286, 2000.
- [16] Gennes, P. G. de: *Scaling Concepts in Polymer Physics*. Cornell University Press, Ithaca, 1979.
- [17] Rubinstein, M. and R.H. Colby: *Polymer Physics*. Oxford University Press, 2003.
- [18] Miyaki, Y., Y. Einaga, and H. Fujita: *Excluded-Volume Effects in Dilute Polymer-Solutions .7. Very High Molecular-Weight Polystyrene in Benzene and Cyclohexane*. Macromolecules, 11(6):1180–1186, 1978.
- [19] Daoud, M., J. P. Cotton, B. Farnoux, G. Jannink, G. Sarma, H. Benoit, R. Duplessix, C. Picot, and P. G. D. Gennes: *Solutions of Flexible Polymers - Neutron Experiments and Interpretation*. Macromolecules, 8(6):804–818, 1975.
- [20] Maier, B. and J. O. Radler: *Conformation and self-diffusion of single DNA molecules confined to two dimensions*. Physical Review Letters, 82(9):1911–1914, 1999.
- [21] Maier, B. and J. O. Radler: *DNA on fluid membranes: A model polymer in two dimensions*. Macromolecules, 33(19):7185–7194, 2000.
- [22] Hansma, H. G., J. Vesenska, C. Siegerist, G. Kelderman, H. Morrett, R. L. Sinsheimer, V. Elings, C. Bustamante, and P. K. Hansma: *Reproducible Imaging and Dissection of Plasmid DNA under Liquid with the Atomic Force Microscope*. Science, 256(5060):1180–1184, 1992.
- [23] Valle, F., M. Favre, P. De Los Rios, A. Rosa, and G. Dietler: *Scaling exponents and probability distributions of DNA end-to-end distance*. Phys Rev Lett, 95(15):158105, 2005.
- [24] Cui, S. X., C. Albrecht, F. Kuhner und H. E. Gaub: *Weakly bound water molecules shorten single-stranded DNA*. Journal of the American Chemical Society, 128(20):6636–6639, 2006.
- [25] Oesterhelt, F., M. Rief, and H. E. Gaub: *Single molecule force spectroscopy by AFM indicates helical structure of poly(ethylene-glycol) in water*. New Journal of Physics, pages 6–6, 1999.
- [26] Kuhner, F., L. T. Costa, P. M. Bisch, S. Thalhammer, W. M. Heckl und H. E. Gaub: *LexA-DNA bond strength by single molecule force spectroscopy*. Biophysical Journal, 87(4):2683–2690, 2004.
- [27] Marszalek, P. E., A. F. Oberhauser, Y. P. Pang, and J. M. Fernandez: *Polysaccharide elasticity governed by chair-boat transitions of the glucopyranose ring*. Nature, 396(6712):661–664, 1998.
- [28] Li, H. B., M. Rief, F. Oesterhelt, H. E. Gaub, X. Zhang, and J. C. Shen: *Single-molecule force spectroscopy on polysaccharides by AFM - nanomechanical fingerprint of alpha-(1,4)-linked polysaccharides*. Chemical Physics Letters, 305(3-4):197–201, 1999.
- [29] Pastre, D., O. Pietrement, A. Zozime, and E. Le Cam: *Study of the DNA/ethidium bromide interactions on mica surface by atomic force microscope: Influence of the surface friction*. Biopolymers, 77(1):53–62, 2005.
-

- 
- [30] Rivetti, C., M. Guthold, and C. Bustamante: *Scanning force microscopy of DNA deposited onto mica: equilibration versus kinetic trapping studied by statistical polymer chain analysis*. J Mol Biol, 264(5):919–32, 1996.
- [31] Yoshizawa, H., Y.L. Chen, and J. Israelachvili: *Fundamental Mechanisms of Interfacial Friction*. J. Phys. Chem., 97:4128–4140, 1992.
- [32] Serr, A. and R. R. Netz: *Pulling adsorbed polymers from surfaces with the AFM: stick vs. slip, peeling vs. gliding*. Europhysics Letters, 73(2):292–298, 2006.
- [33] Evans, E.: *Probing the relation between force - Lifetime - and chemistry in single molecular bonds*. Annual Review of Biophysics and Biomolecular Structure, 30:105–128, 2001.
- [34] Israelachvili, J. N.: *Intermolecular and Surface Forces*. Academic Press, New York, 1992.
- [35] Hugel, T., M. Grosholz, H. Clausen-Schaumann, A. Pfau, H. Gaub und M. Seitz: *Elasticity of single polyelectrolyte chains and their desorption from solid supports studied by AFM based single molecule force spectroscopy*. Macromolecules, 34(4):1039–1047, 2001.
- [36] Seitz, M., C. Friedsam, W. Jostl, T. Hugel, and H. E. Gaub: *Probing solid surfaces with single polymers*. Chemphyschem, 4(9):986–990, 2003.
- [37] Sonnenberg, L., J. Parvole, F. Kuhner, L. Billon und H. E. Gaub: *Choose sides: Differential polymer adhesion*. Langmuir, 23(12):6660–6666, 2007.
- [38] Horinek, D., A. Serr, M. Geisler, T. Pirzer, U. Slotta, S. Q. Lud, J. A. Garrido, T. Scheibel, T. Hugel und R. R. Netz: *Peptide adsorption on a hydrophobic surface results from an interplay of solvation, surface, and intrapeptide forces*. Proceedings of the National Academy of Sciences of the United States of America, 105(8):2842–2847, 2008.
- [39] Netz, R. R. and D. Andelman: *Neutral and charged polymers at interfaces*. Physics Reports-Review Section of Physics Letters, 380(1-2):1–95, 2003.
- [40] Netz, R. R. und J. F. Joanny: *Adsorption of semiflexible polyelectrolytes on charged planar surfaces: Charge compensation, charge reversal, and multilayer formation*. Macromolecules, 32(26):9013–9025, 1999.
- [41] Rentsch, S., H. Siegenthaler und G. Papastavrou: *Diffuse layer properties of thiol-modified gold electrodes probed by direct force measurements*. Langmuir, 23(17):9083–9091, 2007.
- [42] Bard, A. J. und L. R. Faulkner: *Electrochemical Methods: Fundamentals and Applications*. Wiley and Sons, 2000.
- [43] Christie, J. H. und P. J. Lingane: *Theory of Staircase Voltammetry*. Journal of Electroanalytical Chemistry, 10(3):176ff, 1965.
- [44] Ferrier, D. R. und R.R Schroeder: *Staircase Voltammetry with Varied Current Sampling Times - Theory for Diffusion Controlled, Rate Controlled, and Mixed Rate and Diffusion Controlled Electrode-Reactions*. Journal of Electroanalytical Chemistry, 45(3):343–359, 1973.
- [45] Bustamante, C., J. F. Marko, E. D. Siggia und S. Smith: *Entropic Elasticity of Lambda-Phage DNA*. Science, 265(5178):1599–1600, 1994.

- 
- [46] Chiu, T. K. und R. E. Dickerson: *1 angstrom crystal structures of B-DNA reveal sequence-specific binding and groove-specific bending of DNA by magnesium and calcium*. Journal of Molecular Biology, 301(4):915–945, 2000.
- [47] Bai, Y., M. Greenfeld, K. J. Travers, V. B. Chu, J. Lipfert, S. Doniach und D. Herschlag: *Quantitative and comprehensive decomposition of the ion atmosphere around nucleic acids*. Journal of the American Chemical Society, 129(48):14981–14988, 2007.
- [48] Lehninger, A., M. Cox und D.L. Nelson: *Lehninger Principles of Biochemistry*. W H Freeman and Co, 2008.
- [49] Kosenkov, D., L. Gorb, O. V. Shishkin, J. Sponer und J. Leszczynski: *Tautomeric equilibrium, stability, and hydrogen bonding in 2'-deoxyguanosine monophosphate complexed with Mg<sup>2+</sup>*. Journal of Physical Chemistry B, 112(1):150–157, 2008.
- [50] Manning, G. S.: *Limiting Laws and Counterion Condensation in Polyelectrolyte Solutions .I. Colligative Properties*. Journal of Chemical Physics, 51(3):924–934, 1969.
- [51] Maier, B., U. Seifert und J. O. Radler: *Elastic response of DNA to external electric fields in two dimensions*. Europhysics Letters, 60(4):622–628, 2002.
- [52] Angersteinkozłowska, H., B. E. Conway, A. Hamelin und L. Stoicoviciu: *Elementary Steps of Electrochemical Oxidation of Single-Crystal Planes of Au .1. Chemical Basis of Processes Involving Geometry of Anions and the Electrode Surfaces*. Electrochimica Acta, 31(8):1051–1061, 1986.
- [53] Hamelin, A., M. J. Sottomayor, F. Silva, S. C. Chang und M. J. Weaver: *Cyclic Voltammetric Characterization of Oriented Monocrystalline Gold Surfaces in Aqueous Alkaline-Solution*. Journal of Electroanalytical Chemistry, 295(1-2):291–300, 1990.
- [54] Shirahata, S., S. Kabayama, M. Nakano, T. Miura, K. Kusumoto, M. Gotoh, H. Hayashi, K. Otsubo, S. Morisawa und Y. Katakura: *Electrolyzed-reduced water scavenges active oxygen species and protects DNA from oxidative damage*. Biochemical and Biophysical Research Communications, 234(1):269–274, 1997.
- [55] Duval, J., J. Lyklema, J. M. Kleijn und H. P. van Leeuwen: *Amphifunctionally electrified interfaces: Coupling of electronic and ionic surface-charging processes*. Langmuir, 17(24):7573–7581, 2001.
- [56] Duval, J., J. M. Kleijn, J. Lyklema und H. P. van Leeuwen: *Double layers at amphifunctionally electrified interfaces in the presence of electrolytes containing specifically adsorbing ions*. Journal of Electroanalytical Chemistry, 532(1-2):337–352, 2002.
- [57] Barten, D., J. M. Kleijn, J. Duval, H. P. von Leeuwen, J. Lyklema und M. A. C. Stuart: *Double layer of a gold electrode probed by AFM force measurements*. Langmuir, 19(4):1133–1139, 2003.
- [58] Marko, J. F. and E. D. Siggia: *Stretching DNA*. Macromolecules, 28(26):8759–8770, 1995.
- [59] Smith, S. B., Y. J. Cui, and C. Bustamante: *Overstretching B-DNA: The elastic response of individual double-stranded and single-stranded DNA molecules*. Science, 271(5250):795–799, 1996.
-

- [60] Andreatta, D., S. Sen, J. L. P. Lustres, S. A. Kovalenko, N. P. Ernsting, C. J. Murphy, R. S. Coleman und M. A. Berg: *Ultrafast dynamics in DNA: fraying at the end of the helix*. Journal of the American Chemical Society, 128(21):6885–6892, 2006.
- [61] Every, A. E. und I. M. Russu: *Influence of Magnesium Ions on Spontaneous Opening of DNA Base Pairs (vol 112B, pg 7694, 2008)*. Journal of Physical Chemistry B, 112(47):15261–15261, 2008.
- [62] Xu, B. Q. und N. J. J. Tao: *Measurement of single-molecule resistance by repeated formation of molecular junctions*. Science, 301(5637):1221–1223, 2003.
- [63] Chen, F., X. L. Li, J. Hihath, Z. F. Huang und N. J. Tao: *Effect of anchoring groups on single-molecule conductance: Comparative study of thiol-, amine-, and carboxylic-acid-terminated molecules*. Journal of the American Chemical Society, 128(49):15874–15881, 2006.
- [64] Venkataraman, L., J. E. Klare, C. Nuckolls, M. S. Hybertsen und M. L. Steigerwald: *Dependence of single-molecule junction conductance on molecular conformation*. Nature, 442(7105):904–907, 2006.
- [65] Grunder, S., R. Huber, V. Horhoiu, M. T. Gonzalez, C. Schonenberger, M. Calame und M. Mayor: *New cruciform structures: Toward coordination induced single molecule switches*. Journal of Organic Chemistry, 72(22):8337–8344, 2007.
- [66] Herne, T. M. and M. J. Tarlov: *Characterization of DNA probes immobilized on gold surfaces*. Journal of the American Chemical Society, 119(38):8916–8920, 1997.
- [67] Storhoff, J. J., R. Elghanian, C. A. Mirkin und R. L. Letsinger: *Sequence-dependent stability of DNA-modified gold nanoparticles*. Langmuir, 18(17):6666–6670, 2002.
- [68] Bilic, A., J. R. Reimers, N. S. Hush und J. Hafner: *Adsorption of ammonia on the gold(111) surface*. Journal of Chemical Physics, 116(20):8981–8987, 2002.
- [69] Lambropoulos, N. A., J. R. Reimers und N. S. Hush: *Binding to gold(0): Accurate computational methods with application to AuNH<sub>3</sub>*. Journal of Chemical Physics, 116(23):10277–10286, 2002.
- [70] Butt, H. J. and M. Jaschke: *Calculation of Thermal Noise in Atomic-Force Microscopy*. Nanotechnology, 6(1):1–7, 1995.
- [71] Oesterhelt, F., D. Oesterhelt, M. Pfeiffer, A. Engel, H. E. Gaub und D. J. Muller: *Unfolding pathways of individual bacteriorhodopsins*. Science, 288(5463):143–146, 2000.
- [72] Viani, M. B., T. E. Schaffer, A. Chand, M. Rief, H. E. Gaub, and P. K. Hansma: *Small cantilevers for force spectroscopy of single molecules*. Journal of Applied Physics, 86(4):2258–2262, 1999.
- [73] Kuhner, F. and H. E. Gaub: *Modelling cantilever-based force spectroscopy with polymers*. Polymer, 47(7):2555–2563, 2006.
- [74] Dölling, R.: *Potentiostaten - Eine Einführung*. <http://www.bank-ic.de/decms/downloads/potstad-2005-d.pdf>.
- [75] Antipov, A. A., G. B. Sukhorukov, E. Donath, and H. Mohwald: *Sustained release properties of polyelectrolyte multilayer capsules*. Journal of Physical Chemistry B, 105(12):2281–2284, 2001.

- [76] Ladam, G., P. Schaad, J. C. Voegel, P. Schaaf, G. Decher, and F. Cuisinier: *In situ determination of the structural properties of initially deposited polyelectrolyte multilayers*. Langmuir, 16(3):1249–1255, 2000.
- [77] Breslauer, K. J., R. Frank, H. Blocker und L. A. Marky: *Predicting DNA Duplex Stability from the Base Sequence*. Proceedings of the National Academy of Sciences of the United States of America, 83(11):3746–3750, 1986.
- [78] Smith, S. B., L. Finzi, and C. Bustamante: *Direct Mechanical Measurements of the Elasticity of Single DNA-Molecules by Using Magnetic Beads*. Science, 258(5085):1122–1126, 1992.
- [79] Alberts, B., D. Bray, J. Lewis, M. Raff, K. Roberts, and J. Watson: *Molecular Biology of The Cell*. Garland Publishing, 2002.
- [80] Watson, J. D. and F. H. C. Crick: *Molecular Structure of Nucleic Acids - a Structure for Deoxyribose Nucleic Acid*. Nature, 171(4356):737–738, 1953.

# B AFM, potentiostat and polymers

## B.1 AFM basics

The **Atomic Force Microscope (AFM)** was invented in 1986 by Binnig, Quate and Gerber in order to image solid substrates with a mechanical approach [1]: the tip of a cantilever is brought in contact with the surface of a sample and is then moved in lines by a xy-piezo (contact mode). Depending on the topographic height profile of the sample, the cantilever is deflected. This deflection is detected by focusing a laser on the backside of the cantilever, which is typically gold-coated. The reflected signal is then detected by a segmented photodiode. Depending on the deflection of the cantilever, the laser spot on the segmented photodiode is moved. Measuring the differential signal of the segmented photodiode yields a topographic image of the surface [70]. Thereby, images of conductive and insulating samples in atomic resolution are possible. Scanning in an aqueous environment allows the investigation of biological soft matter [3, 71].

### Force extension curves

In conventional AFM based single molecule force spectroscopy measurements, a molecule is fixed between the substrate and the AFM tip (Figure B.1 B). When the AFM cantilever is retracted by the z-piezo, the molecule is "stretched" and a force  $F$  acts on the cantilever due to the intramolecular mechanic characteristics of the molecule. The deflection of the cantilever is detected as mentioned above. The deflection is described by the linear elastic Hooke model

$$F(t) = k_C z_C, \quad (\text{B.1})$$

where  $k_C$  is the spring constant of the cantilever and  $z_C$  is the deflection of the cantilever. The current extension  $d(t)$  of the stretched molecule can be calculated by subtracting the deflection of the cantilever from the detected z-piezo movement  $z(t)$ :

$$d(t) = z(t) - F(t)/k_C. \quad (\text{B.2})$$

Plotting  $F(t)$  vs.  $d(t)$  yields a force extension curve as depicted for example in Figure 5.1. In this way, the resulting force depending on the current extension of a molecule is characterized. Thereby, a precision of Ångström and Piconewton for extension and force can be achieved.

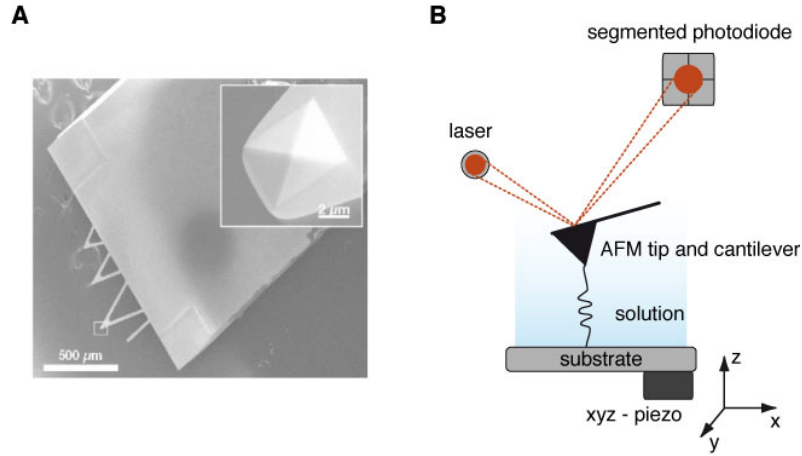


**Figure B.1** AFM cantilevers and measurement scheme. **(A)** Electronmicroscope picture of the "Parklevers" (MLCT-AUHW, Veeco Probes), which were used in this thesis. The chip consists of one rectangular and three triangular AFM cantilevers with different spring constants and resonance frequencies. The inset shows the pyramidal AFM tip of the largest pyramidal cantilever. The radius of curvature is in the range of 10 nm (sharpened version) or 40 nm, respectively. (REM picture by F. Kühner) **(B)** The AFM tip is moved relative to the substrate by the xyz-piezo and a molecule is extended. The resulting force in z-direction, which acts on the AFM cantilever, leads to a deflection depending on spring constant of the cantilever. The deflection is detected via the reflected infrared laser beam on the segmented photodiode.

### Calibration and resolution

The spring constant  $k_C$  of the AFM cantilever is determined by the equipartition theorem [70]: every degree of freedom within a thermodynamic system has the energy  $1/2k_B T$ . The cantilever exhibits only one degree of freedom for fluctuations, so its mean square deflection within a thermal bath is given by

$$\frac{1}{2}k_B T = \frac{1}{2}k_C \langle x^2 \rangle. \quad (\text{B.3})$$

The mean square deflection  $\langle x^2 \rangle$  is determined by a Fourier transformed power spectrum and the Parseval-theorem. Thus,  $k_C$  can be calculated by Equation B.3 with an accuracy of 10 - 20 % of this method.

Moreover, a calibrated conversion factor [ $InvOLS$ ] = m/V (Inverted Optical Lever Sensitivity) is needed to calculate the deflection  $z_C$  from the photodiode difference signal [ $U_D$ ] = V. This factor is obtained from the slope of force extension curves, when the AFM tip is indented on a hard surface. Consequently,  $z_C = InvOLS \cdot U_D$  and from this follows  $F = k_C z_C$ .

The signal-to-noise ratio of the force detection [72] is given by

$$SNR = \frac{\frac{F(\nu)}{k_C} G(\nu)}{\sqrt{\frac{4k_B T R B}{k_C^2} G^2(\nu) + (\text{techn. noise})^2}}, \quad (\text{B.4})$$

where  $G(\nu)$  is the frequency dependent response function,  $B$  is the bandwidth of the filter and  $R$  is the attenuation factor due to viscous damping. The minimal detectable force is then described by

$$F_{min} = \sqrt{4k_B T R B}. \quad (\text{B.5})$$

Consequently, smaller and softer cantilevers provide a better force resolution. The minimal detectable force for the used Veeco cantilevers is 7 - 8 pN [73].

## B.2 Basic principles of potential control

This section provides a short introduction to **potentiostats**, which adjust a constant potential difference between a working electrode and a reference electrode in solution [42, 74]. A counter electrode, a voltage source and an operational amplifier complete the basic setup. The working electrode is connected to the non-inverting input of an operational amplifier and the reference electrode<sup>1</sup> to its inverting input. The potential difference between working and reference electrode is then inverted and amplified by the operational amplifier and a corresponding current is induced into the counter electrode. The electric circuit is then closed via the electrolyte and the charges are directed to the grounded working electrode. This current is measured at the resistance  $R_m$ . Thus, the working electrode would be polarized until the potential difference to the reference electrode is zero. In order to adjust an arbitrary potential difference, a voltage source is connected in series between the working electrode and the non-inverting input of the operational amplifier. The potentiostat adjusts then as described this potential between

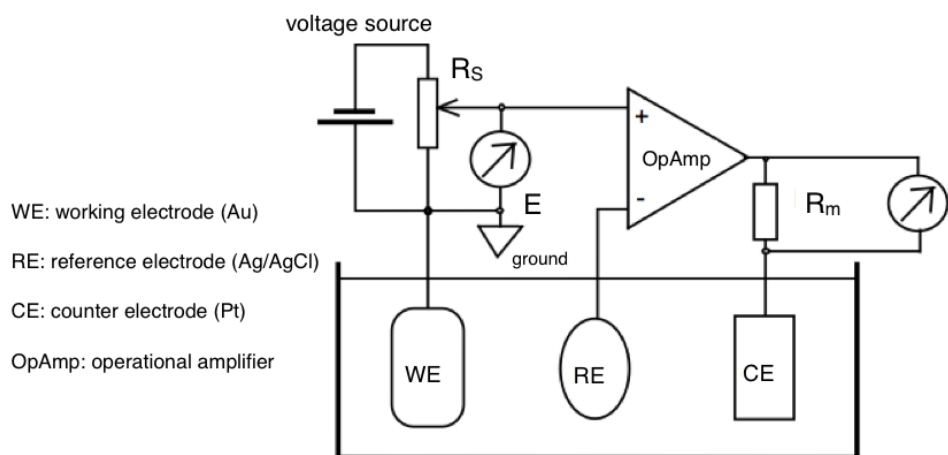


**Figure B.2** Schematics with the most important building blocks of a potentiostat. See text for details.

<sup>1</sup>It has to be noted that the potentiostat input of the reference electrode has a high ohmic resistance ( $M\Omega$  -  $T\Omega$ ), thus electric or ionic currents are not able to polarize the reference electrode. Consequently, the calibrated potential of the reference electrode maintains always the same with respect to the standardized  $H_2$ -electrode and a stable potential measurement is possible.



the working and reference electrode. The potential of the counter electrode with respect to the reference electrode is not considered. The counter electrode is typically an inert metal like platinum to avoid additional oxidation/reduction reactions.

These are only the elementary building blocks and processes of a potentiostat as developed by Wenking in the 1950s. Modern potentiostats include further complex circuitry to avoid electric noise or to provide phase shift corrections etc.

In the experiments presented in chapter 5, a polycrystalline gold microelectrode with a surface of  $1 \text{ mm}^2$  was used as a working electrode. In chapter 4, a self-assembled monolayer (SAM) covered this gold electrode. An Ag/AgCl reference electrode and platinum counter electrode were used in all experiments. For technical details please refer to the corresponding manuscripts.

### **Electrical contact between gold electrode and gold-coated AFM tip**

The electrical contact between AFM tip and electrode, which is essential for the DNA-gold bonding in chapter 5, is explained in detail: For dsDNA functionalization, the AFM tip was gold-coated to enable the covalent attachment of the SAM molecules. However, a degradation of the insulating SAM molecules in the contact area of the AFM tip (the tip radius is ca. 30 nm, which equals an area of  $2800 \text{ nm}^2$ ) was assumed, as an indentation force in the range of 500 pN was applied for a dwell-time of 0.5 s on the tip contact area for each force extension curve.

In order to prove the electrical contact between the AFM tip and the gold electrode, the resistance between these two elements was measured, whereby the tip was electrically contacted and connected to the electrode. A resistance of up to 19 M $\Omega$  was detected, when the AFM tip was not in contact with the electrode, which equaled the resistance of the low concentrated MgCl<sub>2</sub> solution. The resistance measurement with a fresh functionalized AFM tip revealed the same resistance, when the AFM tip was impressed on the electrode. However, after approximately 50 force extension curves, the insulation got lost and a resistance of  $R = 40 \pm 20 \text{ }\Omega$  was measured during indentation. Thus, an electrical contact between the AFM tip and the gold electrode was established as soon as the tip impressed on the electrode. This resistance is in good agreement with an approximate estimation:  $R = \rho \cdot l/A = 30 \text{ }\Omega$ , with  $\rho = 2.44 \cdot 10^{-8} \text{ }\Omega\text{m}$  for gold. Here, the pyramidal tip is considered as a bar shape gold wire with  $l = 3 \text{ }\mu\text{m}$  for the tip height and  $A = 2800 \text{ nm}^2$  as cross section area.

Thus, this electrical contact between AFM tip and electrode short circuited the electric field in the contact zone, and the positive charge of the Mg<sup>2+</sup> ions attracted the negatively charged DNA to the gold electrode.

## B.3 Polymers: CMA, PAAm and DNA

In the following section, the characteristics of the used polymers are presented and discussed:

### Carboxymethylamylose

The polysaccharid carboxymethylamylose (CMA) is made of pyranose rings, which are connected via an  $\alpha$ -D-(1 $\rightarrow$ 4) glycosidic linkage. In nature, the related amylose and amylopectin form starch, e.g. in potatoes or corn. In industry, CMA is used as emulsifier in detergents or in groceries. As explained in chapter 2, an applied force around 275 pN induces the lengthening of the pyranos rings from their ground state chair conformation to the boat conformation [27]. Moreover, the free carboxy-groups allow a covalent attachment to the amino-surface as described in the corresponding publication.

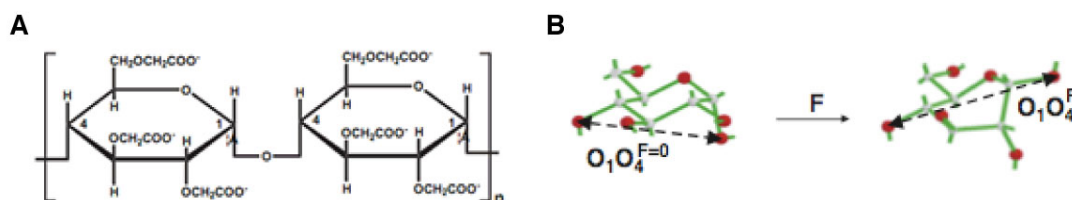


**Figure B.3** (A) Chemical structure of CMA: two pyranose rings are connected by  $\alpha$ -D-(1 $\rightarrow$ 4) glycosidic linkage. (B) Applying approximately 275 pN deforms the chair conformation ( $O_1O_4^{F=0} = 0.4533$  nm) to the boat conformation ( $O_1O_4^F = 0.5408$  nm).

### Polyallylamine

The synthetic cationic polymer polyallylamine exhibits a carbon atom backbone, with attached amino groups at every second carbon atom. It is used as industrial surface coating or in the field of *polyelectrolyte multilayer capsules (PMC)*. Here, cationic polymers create colloidal structures with defined permeability [75, 76].

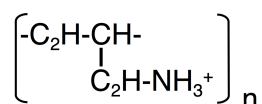


**Figure B.4** Chemical structure of polyallylamine. Amino groups are attached at every second carbon atom of the backbone. The polymer is cationic, as it may be positively charged due to the pH-value.

## DNA

Deoxyribonucleic acid (DNA) is the carrier of genetic information in all living organism and a few viruses. Moreover, numerous biotechnological applications are based on DNA. Thus, DNA is one of the most important and best characterized polymers [5, 59, 77, 78]. Here, only the basic structural information is presented, further details can be found in standard textbooks [48, 79]. Its structure was first described by Watson and Crick [80]: double stranded DNA (dsDNA) is made of two single DNA strands (single stranded DNA, ssDNA), which form a double helix by hybridization (Figure B.5 B).

The genetic information is coded with only four bases: adenine (A), thymine (T), guanine (G) and cytosine (C), whereby the complementary bases A and T or C and G form stable hydrogen bonds. Hydrogen bonds and stacking of the bases provide then a stable double helix structure, which is also called B-DNA. Each base is attached to a sugar ring (2-deoxyribose), whereby the sugar rings are connected by phosphodiester bonds to form a single DNA strand. The combination of single base, sugar and phosphate group is called nucleotide.

Due to their asymmetric phosphodiester linkage, two hybridized DNA strands run in opposite directions to each other (antiparallel). Thus, the 5'-end of a dsDNA molecule provides a single phosphate group, which can be double negatively charged depending on the pH-value. This effect is explained in chapter 4. In Figure B.5 A, the chemical

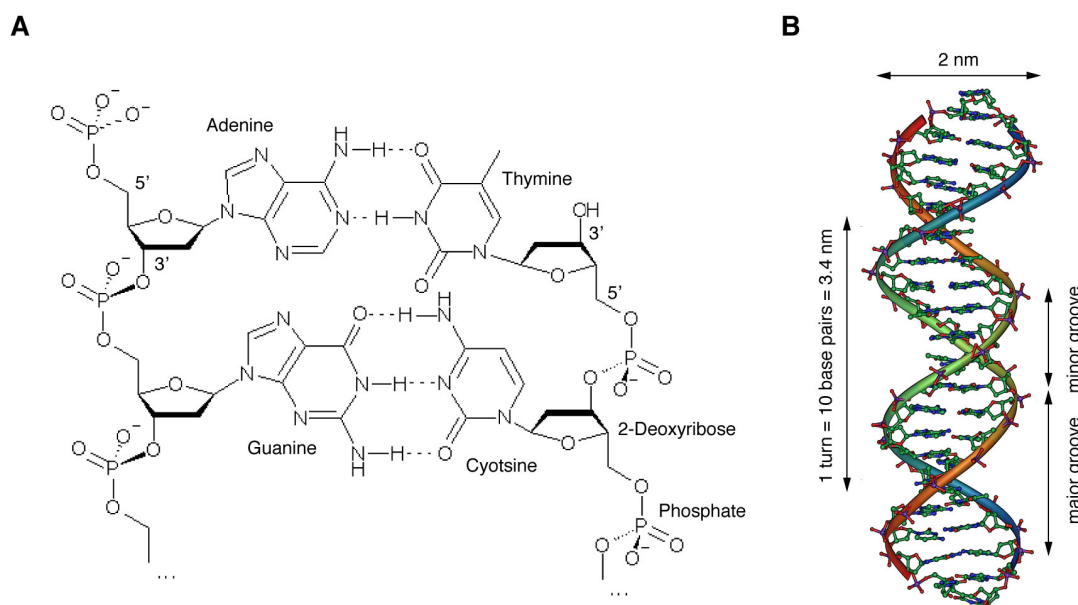


**Figure B.5** (A) Structure of dsDNA: the four bases adenine, thymine, guanine and cytosine are attached to sugar rings (2-deoxyribose), which are linked by phosphodiester bonds (ssDNA). Two complementary ssDNA molecules hybridize and form dsDNA. Important for the presented studies are the double charged 5'-end and the missing primary amino group for thymine. (B) Double helix form of B-DNA with characteristic values. Despite a width of 2 nm, the length of a DNA molecule may be several microns in organisms, which indicates the high mechanical stability of DNA (pictures are adapted from Wikipedia).

structures of the four bases are depicted as well: thymine is the only base, which exhibits no primary amino group and is therefore not able to form coordinative bonds with gold atoms. This effect is discussed in chapter 5.

## C Publications in preparation

Two manuscripts are in preparation, which are based on the DNA-gold bonding study presented in chapter 5:

- *A.R. Fornof, M. Erdmann, R. David and H.E. Gaub* describe the influence of the polymer backbone charge on the electrical controlled N-Au bonding. Three polymers with differently charged backbones and primary amine endgroups were utilized to control adhesion based on the electric potential of the surface as well as probe the influence of backbone charge on this process. The neutral polymer chosen was poly(ethylene glycol) (PEG-NH<sub>2</sub>), a commercially available polymer; a 2,2-ionene, which was synthesized in-house, with a primary amine endgroup was selected for the positively charged backbone and finally double-stranded DNA, where three of the four bases contain primary amines, was used as the negatively charged polymer. Consequently, the adhesion could be tuned by the backbone charge of the polymer: if the polymer amino endgroup reacted with the gold surface or not depended on the direction of applied potential.
- *R. David, M. Erdmann, A.R. Fornof and H.E. Gaub* introduce a new method to functionalize AFM tips with a poly(ethylene glycol) spacer (PEG) and single nucleotides via the phosphoamidite method. First, the silicon oxide AFM tip is functionalized with an epoxysilane. The epoxy function reacts in a second step the amino group of NH<sub>2</sub>-PEG-OH. The reaction of the OH-function with a phosphoamidite-nucleotide leads to a PEG-phosphite triester, which is then oxidized to PEG-phosphate triester. Removal of protecting groups leads to a nucleotide functionalized tip. The binding force of 170 pN for a single N-Au bond based on the interaction between the primary amino group of adenine and the gold surface could be determined with these functionalized AFM tips.

# Acknowledgment

This thesis is not only based on experiments and time in the lab - most important are all the persons and friends behind it, who supported me during these three years, gave me advice or accompanied me. I want to thank all of them and in particular:

- *Prof. Hermann E. Gaub* for the fascinating projects and ideas, the excellent infrastructure and instructive discussions. Thank you for the possibility to work at this chair ... and of course for the exquisite art of cooking!
- *Dr. Ralf David* for the essential contributions in terms of biochemistry and the discussions on the DNA projects - especially at regular lunch & espresso meetings. Thank you for the interesting and cordial conversations!
- *Dr. Ann Fornof* for the contributions on the N-Au bonding experiments and for the continuation of this project.
- *Dr. Ferdinand Kühner* for his technical instructions and advice during my diploma thesis, which constituted the basis of my further work.
- *Dominik Ho* for discussions and having a great time in the lab, in the fitness club and our leisure time.
- *Jan Vogelsang* for discussions in or out of the lab and proof reading of this thesis.
- *Dr. Elias Puchner, Dr. Thorben Cordes, Philip Severin, Katja Falter, Uta Steinbach and the whole Gambicrew* for the fantastic and inspiring working environment.
- *the responsible persons behind SFB 486, NIM, CeNS and the LMU*, who provide a top-notch scientific infrastructure in Munich.
- my former fellow student *Marcus Schaffry*, who is now in Oxford, for the great times at mutual visits.

Finally, I would like to thank especially my parents *Ulrike* and *Dr. Juergen Erdmann*. Their support and motivation were crucial to the success of this thesis. Thank you so much!